

Impact of Antenna and Propagation on Wireless Communication Technology: Terminal, Base Station, and Channel Modeling

Guest Editors: Guangyi Liu, Cheng-Xiang Wang, Min Zhang,
James Warden, and Huanhuan Gu





Impact of Antenna and Propagation on Wireless Communication Technology: Terminal, Base Station, and Channel Modeling

International Journal of Antennas and Propagation

Impact of Antenna and Propagation on Wireless Communication Technology: Terminal, Base Station, and Channel Modeling

Guest Editors: Guangyi Liu, Cheng-Xiang Wang, Min Zhang,
James Warden, and Huanhuan Gu



Copyright © 2013 Hindawi Publishing Corporation. All rights reserved.

This is a special issue published in "International Journal of Antennas and Propagation." All articles are open access articles distributed under the Creative Commons Attribution License, which permits unrestricted use, distribution, and reproduction in any medium, provided the original work is properly cited.

Editorial Board

M. Ali, USA
Charles Bunting, USA
Felipe Ctedra, Spain
Dau-Chyrh Chang, Taiwan
Deb Chatterjee, USA
Z. N. Chen, Singapore
M. Y. Wah Chia, Singapore
Christos Christodoulou, USA
Shyh-Jong Chung, Taiwan
Lorenzo Crocco, Italy
Tayeb A. Denidni, Canada
Antonije R. Djordjevic, Serbia
Karu P. Esselle, Australia
Francisco Falcone, Spain
Miguel Ferrando, Spain
Vincenzo Galdi, Italy
Wei Hong, China
Hon Tat Hui, Singapore
Tamer S. Ibrahim, USA
Nemai Karmakar, Australia

Se-Yun Kim, Republic of Korea
Ahmed A. Kishk, Canada
Tribikram Kundu, USA
Byungje Lee, Republic of Korea
Ju-Hong Lee, Taiwan
L. Li, Singapore
Yilong Lu, Singapore
Atsushi Mase, Japan
Andrea Massa, Italy
Giuseppe Mazzarella, Italy
Derek McNamara, Canada
C. F. Mecklenbruker, Austria
Michele Midrio, Italy
Mark Mirotznik, USA
A. S. Mohan, Australia
P. Mohanan, India
Pavel Nikitin, USA
A. D. Panagopoulos, Greece
Matteo Pastorino, Italy
Massimiliano Pieraccini, Italy

Sadasiva M. Rao, USA
Sembiam R. Rengarajan, USA
Ahmad Safaai-Jazi, USA
S. Safavi-Naeini, Canada
M. Salazar-Palma, Spain
Stefano Selleri, Italy
Krishnasamy T. Selvan, India
Zhongxiang Q. Shen, Singapore
John J. Shynk, USA
M. Singh Jit Singh, Malaysia
Seong-Youp Suh, USA
Parveen Wahid, USA
Yuanxun Ethan Wang, USA
Daniel S. Weile, USA
Tat Soon Yeo, Singapore
Young Joong Yoon, Korea
Jong-Won Yu, Republic of Korea
Wenhua Yu, USA
Anping Zhao, China

Contents

Impact of Antenna and Propagation on Wireless Communication Technology: Terminal, Base Station, and Channel Modeling, Guangyi Liu, Cheng-Xiang Wang, Min Zhang, James Warden, and Huanhuan Gu
Volume 2013, Article ID 368457, 2 pages

Fading Characteristics of Wireless Channel on High-Speed Railway in Hilly Terrain Scenario, Fengyu Luan, Yan Zhang, Limin Xiao, Chunhui Zhou, and Shidong Zhou
Volume 2013, Article ID 378407, 9 pages

Positive Effect of Severe Nakagami- m Fading on the Performance of Multiuser TAS/MRC Systems with High Selection Gain, Chia-Chun Hung, Ching-Tai Chiang, Rong-Ching Wu, and C. Lee
Volume 2012, Article ID 987631, 7 pages

Investigation of the Effect of Noise Correlations on Diversity Gains and Capacities of Multiport Antennas Using Reverberation Chamber, Xiaoming Chen and Jian Yang
Volume 2012, Article ID 486730, 9 pages

High Gain Array of Monopoles-Coupled Antennas for Wireless Applications, Ahmad El Sayed Ahmad, Marc Thevenot, Jean-Marie Floc'h, and Mohamad Mantash
Volume 2012, Article ID 725745, 8 pages

Validation of Antenna Modeling Methodology in IMT-Advanced Channel Model, Jianhua Zhang and Chun Pan
Volume 2012, Article ID 282797, 9 pages

Statistical Modeling of Antenna: Urban Equipment Interactions for LTE Access Points, Xin Zeng and Alain Sibille
Volume 2012, Article ID 292018, 14 pages

Differences in User Influence on MIMO Handset Antenna Performance in Reverberation Chamber, Juan D. Sánchez-Heredia, Paul Hallbjörner, Juan F. Valenzuela-Valdés, Thomas Bolin, and Antonio M. Martínez-González
Volume 2012, Article ID 826425, 5 pages

Impact of Antenna Placement on Frequency Domain Adaptive Antenna Array in Hybrid FRF Cellular System, Sri Maldia Hari Asti, Wei Peng, and Fumiyuki Adachi
Volume 2012, Article ID 538161, 9 pages

Editorial

Impact of Antenna and Propagation on Wireless Communication Technology: Terminal, Base Station, and Channel Modeling

Guangyi Liu,¹ Cheng-Xiang Wang,² Min Zhang,³ James Warden,⁴ and Huanhuan Gu⁵

¹ Wireless Department of China Mobile Research Institute, Beijing, China

² Joint Research Institute for Signal and Image Processing, School of Engineering & Physical Sciences, Heriot-Watt University, Edinburgh, UK

³ Alcatel-Lucent Telecom Ltd., The Quadrant Stonehill Green, Westlea, UK

⁴ Research In Motion Ltd., USA

⁵ Research In Motion Ltd., Canada

Correspondence should be addressed to Guangyi Liu; liuguangyi@chinamobile.com

Received 14 March 2013; Accepted 14 March 2013

Copyright © 2013 Guangyi Liu et al. This is an open access article distributed under the Creative Commons Attribution License, which permits unrestricted use, distribution, and reproduction in any medium, provided the original work is properly cited.

For wireless communication, the antennas at both sides of the wireless chain and the corresponding propagation characteristics play an important role in the system design and optimization. In past standardization activities, for example, in 3GPP LTE/LTE-Advanced and IEEE 802.16m, only some simplified antenna patterns are assumed during the standardization, which may influence the system parameter optimization and system performance for practical deployment. For example, only omnidirectional antenna pattern is assumed at the terminal, and perfect sectoring antenna pattern is assumed at the base station, while the impact of practical antenna pattern, coupling among the antennas, and human body on the channel characteristics have been ignored. It is therefore valuable to evaluate how these nonideal issues on the antennas will influence the propagation characteristics and thus the system design. This special issue has accepted 8 papers as below.

The first paper investigates the positive effect of severe Nakagami- m fading on the performance of multiuser Transmit Antenna Selection/Maximal-Ratio Combining (TAS/MRC) systems with high selection gain. Both amount of fading (AF) and symbol error rate (SER) of M-QAM are derived as closed-form expressions for integer m . For arbitrary m , the AF and the SER are expressible as a single infinite series of Gamma function and Gauss hypergeometric function,

respectively. The analytical results lead to the following observations. First, the SER performance can demonstrate the positive effect of severe Nakagami- m fading on multiuser TAS/MRC systems with high selection gain. Second, the AF performance only exhibits the negative impact of severe fading regardless of high selection gain. Last, the benefit of severe fading to the system performance diminishes at high signal-to-noise ratio (SNR).

In the second paper, an array of monopoles antenna over a ground plane that radiates a directive lobe in the end-fire direction is described. The design uses the rigorous method described in order to synthesis the radiation though the strong cumulative coupling between the monopoles. A gain higher than 20 dB was achieved in the end-fire direction over a 4.5% bandwidth. However, the antenna has been tilted in order to compensate the beam deviation caused by the edge diffraction. A prototype with 12 elements has been manufactured in order to validate the antenna principle and the whole antenna is successfully measured.

In the third paper, user influence on multiple-input multiple-output (MIMO) performance is studied for different dual antenna handsets specially designed to have good and bad MIMO performance. The study reveals that user influence can cause either improvement or degradation for different test objects, including a spread effect over the parameters.

Differences in performance between good and bad handsets can be clear when they are measured without user influence, but become small under real person influence. This result illustrates the particular importance of user influence to characterize MIMO handsets.

The fourth paper focuses on the fading characteristics of wireless channel on high-speed railway (HSR) in hilly terrain scenario. From the measurement conducted on the Guangzhou-Shenzhen passenger dedicated line in China with the speed of 295 km/h at 2.4 GHz, the fading parameters, including path loss, shadow fading, and K -factor, are analyzed. Compared with the free space path loss model, the measured path loss value in hilly terrain scenario suffers greater decay and shows the property of having a breakpoint distance as the WINNER HSR model shows. The shadow fading is lognormal fitting and changed with two turning points. the mean value of decorrelation distance is around 14 m. But the value will rise up when getting near to the huge reflectors. The K -factor as a fast fading parameter is also influenced by the breakpoint distance. Within the breakpoint distance, K -factor decreases as the T-R distance increases. Beyond the break point distance, the value of K -factor fluctuates dramatically.

In the fifth paper, to evaluate the sector antenna performance degradation, three performance indicators are defined as the normalized "In Sector Power Gain" (ISPG), the normalized "In Sector Mean Power Gain" (ISMPG), and the "In Sector Standard Deviation of the Power Gain" (ISSDPG). Then the antenna performance degradation in three conventional wireless access point scenarios of small cell (antenna wall, antenna shelter, and antenna-lamp post) is investigated for directional or omnidirectional antennas. The results indicate that the lognormal distribution (Gaussian in dB) is often approximately obeyed, as regards the power gains in the considered sector. This is true for the antenna-wall scenario, while in the antenna-shelter and antenna-lamp post scenarios, the ISPG appears to follow the generalized Gaussian distribution. The ISSDPG follows well a lognormal distribution in the antenna-wall scenarios, within the frequency band from 1.7 GHz to 2.0 GHz for both directional and nondirectional antennas.

In the sixth paper, the impact of antenna separation and angle-of-arrival (AOA) spread on frequency domain adaptive antenna array (FDAAA) receiver and hybrid frequency reuse factor are analyzed. Large AOA spread can increase the cellular capacity, and increasing the antenna separation to above 5λ can greatly increase the cellular capacity. The optimal frequency reuse factor (FRF) depends on the channel propagation and transceiver scheme as well. Hybrid FRF algorithm can effectively improve the cellular outage capacity and therefore hybrid FRF together with FDAAA receiver is a good solution for uplink transmission in cellular system.

In the seventh paper, the modeling methodology that the antenna pattern and antenna constellation could be incorporated into propagation channel model independently by receiver antenna and transmitter antenna is validated by the field channel measurement in indoor scenarios at 2.35 GHz. First, the 2×2 MIMO channel impulse responses (CIRs) is recorded with practical dipole

antenna (DPA) and real terminal antenna as the reference. Second, the CIRs are reconstructed from the available International Mobile Telecommunications-Advanced (IMT-Advanced) channel model with the field patterns of test antennas and updated spatial parameters extracted from the similar measurement, in which the omnidirectional antenna array (ODA) is used at both sides of the transmission link to capture the omnidirectional spatial information. The comparisons between field data and reconstructed data are made from coherent bandwidth, eigenvalue dispersion, outage capacity, and ergodic channel capacity. It is found that the reconstructed data closely approximates real data in coherent bandwidth and correctly describe the statistical characteristics in frequency domain. But difference is found in the spatial correlation, which causes the underestimation of the 5% channel outage capacity. So the modeling method which ignores the nonideal issues on the antennas will have impact on the characteristics of MIMO channel, especially on the spatial characteristics.

In the eighth paper, the influence of correlated noises on the Maximal-Ratio Combining (MRC) diversity gain and multiple-input multiple-output (MIMO) capacity is investigated. The noise correlation effects on diversity gains and capacities are formulated using the noise prewhitening concept, and the computational robustness of the derived MRC CDF was proved rigorously. The effects of correlated noises on MRC diversity gains and MIMO ergodic capacities were studied via reverberation chamber measurements. It was shown that, only for multiport antennas with very small correlations, the noise correlation effects on diversity gains (capacities) can be neglected. Otherwise, it should be taken into account for accurate diversity (capacity) measurements.

Guangyi Liu
Cheng-Xiang Wang
Min Zhang
James Warden
Huanhuan Gu

Research Article

Fading Characteristics of Wireless Channel on High-Speed Railway in Hilly Terrain Scenario

Fengyu Luan, Yan Zhang, Limin Xiao, Chunhui Zhou, and Shidong Zhou

State Key Laboratory on Microwave and Digital Communications, Tsinghua National Laboratory for Information Science and Technology, Department of Electronic Engineering, Tsinghua University, Beijing 100084, China

Correspondence should be addressed to Yan Zhang; yanz@tsinghua.edu.cn

Received 13 July 2012; Revised 26 January 2013; Accepted 28 January 2013

Academic Editor: Cheng-Xiang Wang

Copyright © 2013 Fengyu Luan et al. This is an open access article distributed under the Creative Commons Attribution License, which permits unrestricted use, distribution, and reproduction in any medium, provided the original work is properly cited.

This paper focuses on the fading characteristics of wireless channel on High-Speed Railway (HSR) in hilly terrain scenario. Due to the rapid speed, the fading characteristics of HSR channel are highly correlated with time or Transmit-Receive distance and have their own special property. To investigate the fading characteristics, the measurement is conducted on the Guangzhou-Shenzhen passenger-dedicated line in China with the speed of 295 km/h in the data-collection area at 2.4 GHz. From the measured data, the amplitude of each path is estimated by using the Subspace-Alternating Generalized Expectation-Maximization (SAGE) algorithm along with other parameters of channel impulse responses. Then the fading parameters, including path loss, shadow fading, and K -factor, are analysed. With the numerical results in the measurement and analysis, the fading characteristics have been revealed and modelled. It is supposed that this work has a promotion for HSR communication system design and improvement.

1. Introduction

High-Speed Railway (HSR) has the properties of large conveying capacity, good security, low-energy consumption, and vast economic benefits [1, 2]. With rail speed designed to travel at no less than 200 km/h [1], HSRs are widely deployed around the world. For example, the Japanese Shinkansen started in the year of 1963, at a maximum speed of 320 km/h, while the Eurostar is running across the European continent with the speed reaching 300 km/h. In recent years, China has paid more attention to the HSR and has made great progress. Upon the end of year 2011, the operating mileages surpassed 1300 kilometers, making HSR an increasingly important form of transportation.

However, there is a great difference for wireless channel between the HSR scenario and the typical scenario, especially in fading characteristics. In general, communication systems are very sensitive to the fading of the wireless channel, which causes intercarrier interfaces and degrades system performance [3]. The HSR scenario has the special property of high velocity and rapidly changing environment. So the channel exhibits great position-based fading characteristics,

which introduces problems to increase the wireless communication capacity and improve the wireless communication quality. On the other hand, the fading characteristics play an important role in system simulation. Only the influence of fast small-scale fading is considered in most communication simulation methods. But in HSR scenario, path loss and shadow fading are also changed in a continuous simulation process with a long distance caused by high moving speed. For these reasons, having a good knowledge of the HSR wireless channel fading characteristics will help to give a reference for the HSR communication system simulation.

It is significant to get reliable and realistic fading characteristics of the HSR wireless channel through the wideband channel measurements. The HSR scenarios can be divided into different types, including hilly terrain, viaduct, tunnel, cutting, and station. Several HSR channel measurements have been performed by researchers worldwide. The viaduct, tunnel, cutting, and hilly terrain scenarios are measured and modeled, respectively. Liu et al. give the position-based measurement result of HSR channel fading parameters at 2.35 GHz in viaduct scenario [4]. The measurements of path loss and delay spread in tunnels of different sizes at 2.154 GHz

are performed by Helsinki University of Technology [5]. Cichon et al. also build up a ray-optical propagation model for tunnel channel [6]. The Rice K -factor in cutting scenario is presented in [7] with the measurement frequency of 930.2 MHz. Some channel parameters including delay spread and K -factor in different scenarios and different railways are compared [8]. The nonstationary MIMO channel model based on the space-time-frequency correlation function for HSR communication system is proposed for modeling the time-variant property of different taps [9].

To the best of our knowledge, existing researches seldom pay attention to the position-based property of the hilly terrain HSR channel. The hilly terrain occupies 69.1% of the area in China. And the newly built lines of China, such as the Chengdu-Guiyang passenger-dedicated line and Guangzhou-Shenzhen passenger-dedicated line, run through vast area of hilly terrain. The HSR hilly terrain channel measurement and modeling are of great significance. Compared with other scenarios, the scattering and position-based property of the multipath propagation is more complicated and more obvious in hilly terrain. Both large-scale fading and small-scale fading are changed with the train fast moving. In this paper, the fading characteristics of the wireless channel in hilly terrain scenarios are analyzed from the actual channel measurement data. We also attempt to give out the models which describe the position-based statistic property of different channel parameters which reveal the characteristics, such as path loss, shadow fading, and K -factor. The reliable and realistic model serves as the foundation for designing and improving the HSR communication systems.

The main contributions of our works consist of the measurement newly conducted in the HSR hilly terrain scenario, the proposition of the position-based models of different channel parameters, and the application of the Subspace-Alternating Generalized Expectation-Maximization (SAGE) algorithm. SAGE algorithm is regarded as a high-resolution channel parameter estimation method and fits for dealing with the several position-based channel parameters by jointing the time and frequency domains. The properties of path loss, the lognormal shadowing, and K -factor are concluded in this paper. These properties are compared with the current models and explained in detail by investigating the Transmit-Receive (T-R) distance and actual measurement scenario.

The remainder of the paper is organized as follows. In Section 2, the description of hilly terrain scenario and the arrangement of the measurement are outlined. And in Section 3, the details of the SAGE algorithm application are laid out. In Section 4, statistic results of position-based channel parameters which are used for building the channel fading models are discussed and analyzed. The paper is concluded in Section 5.

2. Measurement Setup

The measurement in this paper is taken on the Guangzhou-Shenzhen passenger-dedicated line. The main terrains along the railway are hilly terrain and plain with viaducts. These two types of scenarios are almost distributed alternatively.

Here the paper focuses on the hilly terrain scenario. Figure 1 shows satellite map of our measured hilly terrain scenario. It is generated using the Google Maps tool [10]. The white line is referred to as the railway from West to East. And the base station is located at the position which is 63 km from Guangzhou and 41 km from Shenzhen as the green arrow shows along the railway with the GPS coordinates of 22.830558 N, 113.860235 E. In the data-collection area, many kinds of scattering objects are observed around the railway at the foot of hills. Besides hills, there is a big pond near the railway in the distance of about 600 m from the base station. The areas with an abundance of buildings, factories, and warehouses appear in the distance of about 800 m and 2200 m, respectively. It can be seen that an expressway intersects with the railway from far to near. In this scenario, the relative altitudes of these main scattering objects are mostly below 200 m. In summary, there are several significant properties which have huge effect on the channel fading characteristics in the HSR hilly terrain scenario during the signal transmission.

- (1) With the high-altitude transmit antenna and low-altitude obstacles, the Line of Sight (LOS) is observable and can be detected along the entire railway.
- (2) In hilly terrain, the propagation environment is high density scattered, and scattering objects are distributed irregularly and nonuniformly. The constructive and destructive interference among different multipath components (MPCs) with similar delay is serious. This phenomenon has influence on the channel fading characteristics.
- (3) The high speed will not only cause the large Doppler frequency shift, but also bring the rapid change to the channel parameters. When the train moves quickly, both the propagation environment and the angles of incidence vary quickly. The signal will go through different propagation paths. At the same time, the channel parameters are changed.

Our measurement is conducted by using the THU channel sounder. The parameters of the measurement setup are listed in Table 1. The center frequency is 2.4 GHz, and the bandwidth is 40 MHz. The transmit antenna is mounted on the base station tower (Figure 2(a)). It is a directional antenna pointing at the direction of train travelling with the gain of 17 dBi. The receive antenna is fixed on the window of the high-speed moving train carriage (Figure 2(b)). It is vertically polarized and omnidirectional with the gain of 7 dBi. The transmitter and the receiver are both locked to GPS-derived 10 MHz references, thereby eliminating frequency offsets between the two time bases. In the transmitter, the test signal is fed through the power amplifier to the transmit antenna with the total power of 20 dBm. After receiving the test signal, the receiver does the low-noise amplification and down conversation. Then the signal is sampled with the sample rate of 100 MHz and stored to the disk array of a server for offline analysis [11].

The test signal is regarded as a linear frequency modulated (LFM) sequence. Its length is $12.8 \mu\text{s}$. Due to the good



FIGURE 1: Satellite map of measured hilly terrain area.



FIGURE 2: (a), (b) are photos of the propagation environments at the transmit side and receive side, respectively.

TABLE 1: Parameters of the measurement setup.

Parameter	Value
Central frequency	2.4 GHz
Bandwidth	40 MHz,
Transmitter power	20 dBm
	1 Tx and 1 Rx
Antenna pattern and gain	Tx: directional antenna with 17 dBi Rx: Omnidirectional antenna with 7 dBi
Tx height	30 m
Rx height	1.2 m
Test signal length	12.8 μ s
The minimum distance between Tx and railway	10 m
The penetration loss of the window	12.4 dB
The speed of HSR train	295 km/h

autocorrelation property of the LFM sequences, the measurement principle of LFM signal is that the received sequence is correlated with the local copy of the sequence at the

receiver to produce the measured channel impulse response. Then the offline and broadband features simplify the system operation. After the measurement data is stored in the server, the channel parameter estimation method such as SAGE algorithm is utilized to search and separate the different multipath components, according to the different delay and Doppler frequency of each component. Furthermore, the calibrations of the response of radio frequency (RF) at both Tx side and Rx side and the measurement of the penetration loss of the carriage window are also conducted in each measurement.

In the measured hilly terrain, the height of transmit antenna h_b is 30 m, and the height of receive antenna h_m is 1.2 m. The minimum distance between transmit antenna and the railway is 10 m. The GPS system of the train shows the speed of the train in the data-collection area remains 295 km/h. The total length of the measured route is 2600 m from the base station. Beyond this distance, the train will rush into a tunnel. The main reflections of the electromagnetic wave come from ground, hill, buildings, ponds, and plantings as mentioned above.

Providing the wireless signal coverage for HSR is a very important and tremendous task, which is related to both the

channel fading characteristics and coverage scheme. There are two schemes for HSR wireless signal coverage. One scheme is using a moving relay station mounted on the roof of the carriage. The mobile terminals are linked to base station via the relay station indirectly. This scheme has been detailed in [4, 12]. The other scheme of realizing HSR communication is that the mobile terminals in the carriage are linked directly to the base stations on the ground. In this scheme, the electromagnetic waves suffer a penetration loss from the carriage windows [9]. The second scheme is adopted in this measurement.

3. Analysis Method

SAGE algorithm is proposed as a low-complexity approximation of the Maximum Likelihood (ML) estimation and successfully applied in different application purposes [13]. With this algorithm, accurate estimations of channel parameters from the measured data can be obtained. In the SAGE algorithm, the received and transmitted signals can be described as a finite number of plane waves [14]:

$$r(t) = \sum_{l=1}^L \alpha_l e^{-j2\pi\nu_l t} s(t - \tau_l), \quad (1)$$

where L is the total number of extracted MPCs and α_l , τ_l , and ν_l are, respectively, the complex amplitude, delay, and Doppler frequency of the l th MPC. The advantage of SAGE algorithm is that it can achieve the joint estimation of the complex amplification, delay, and Doppler frequency of the MPCs through iteration process. Based on the estimated value of delay and Doppler frequency, the LOS component is separated from the Non-Line of Sight (NLOS) components. At the second step with the achieved complex amplitude of each MPC, the path loss, shadow fading, and K -factor are calculated according to the definitions to give a description of the position-based fading characteristics of the HSR channel.

During the data analysis, the starting point of distance and time is chosen as the point of HSR train just passing by the base station with the 0 Doppler frequency shift. The T-R distance is proportional to time in the measurement.

4. Measurement Results

4.1. Path Loss. Path loss as a large-scale fading parameter is analyzed to help make a link budget for system design and base station site selection. To obtain the path loss, the traditional method usually averages snapshots corresponding to 5~40 wavelengths for removing the effects of small-scale fading. The SAGE algorithm has the ability to separate each MPC according to different delays, Doppler shifts, and amplitudes. With the method of just summing up the power of each MPC, the path loss can be calculated after removing the gain of antennas (Tx 17 dBi, Rx 7 dBi), penetration loss of carriage window (12.4 dB) and other influencing factors.

The statistical model is often expressed by

$$PL(\text{dB}) = 10 \cdot n \cdot \log 10(d) + PL_0 + X_\sigma(d), \quad (2)$$

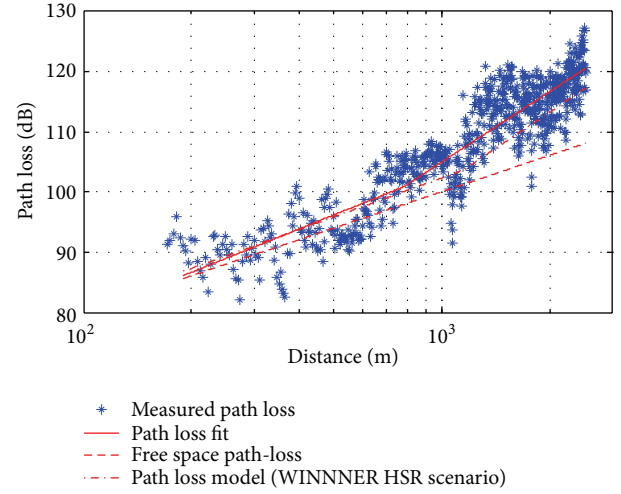


FIGURE 3: Path loss in hilly terrain.

where n is the path loss exponent, d is the distance between the transmitter and receiver, PL_0 is the intercept, and $X_\sigma(d)$ denotes the shadow fading with the standard deviation. Path loss depends on the distance between transmitter and receiver. Figure 3 shows the measured path loss and the fitting curve. It is noticed that there is a breakpoint within position-based measurement data. So the fitting broken curve is obtained by using the linear least square method in near and far regions relative to the base station, respectively. The breakpoint of the fitting curve is 788.6 m of T-R distance. At 788.6 m, the value of path loss is 100.9 dB. The equation of the path loss model with standard deviation σ for this scenario is modeled by

$$PL(\text{dB})$$

$$= \begin{cases} 31.31 + 24.0 \log_{10}(d), & \sigma = 3.3 \text{ dB}, d < 788.6 \text{ m}, \\ -11.6 + 38.8 \log_{10}(d), & \sigma = 4.2 \text{ dB}, d \geq 788.6 \text{ m}. \end{cases} \quad (3)$$

The fitting curve can be regarded as a two-slope model. For this model, the LOS path between transmitter and receiver is strong, and the contributions from all the scatters are small in a short distance. However, beyond the breakpoint distance, the scatters start to play an important role. In the two-slope model, the breakpoint distance [15] depending on the clearance of the first Fresnel zone is defined as

$$r_b = 4 \frac{h_b h_m}{\lambda}, \quad (4)$$

where h_b and h_m are the heights of the transmit antenna and receive antenna, respectively, and λ is the wavelength. The r_b is calculated as 1152 m. This distance is assumed that there are no high obstacles around the propagation route. The measured distance 788.6 m is smaller than r_b . Our result is due to two fitting lines' intersection. This situation is attributed to certain scattering objects. The hills and huge buildings with similar height of the transmit antenna at the distance of 800 m–1000 m are all responsible for this

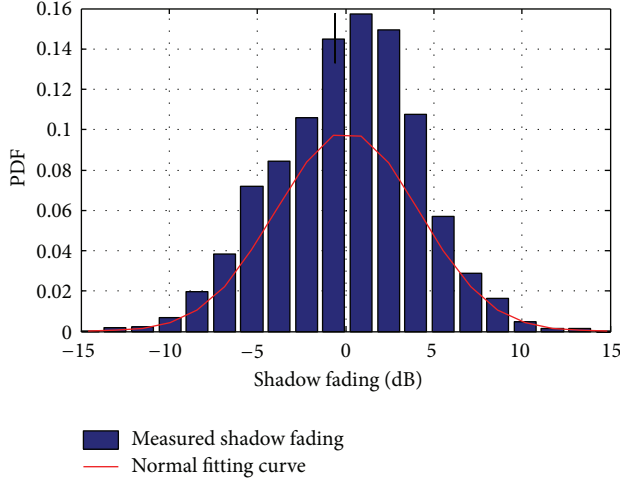


FIGURE 4: PDF of shadow fading in hilly terrain.

phenomenon, where MPCs suffer complex constructive and destructive interference due to diffractions.

The free space path loss and the path loss model in the WINNER II HSR scenario [15] are also showed for comparison. The measured path loss suffers greater loss than the value in free space fading. The WINNER II path loss model is also described by the two-slope model with a breakpoint distance. From Figure 3, the fitting curve is very close to the WINNER II path loss model. The main differences exist not only in the aspect of breakpoint distance, but also in the aspect of slopes of the two segments. The slopes of the two segments of WINNER II path loss model are 21.5 and 40, respectively. There is a visible gap between the slopes of WINNER II path loss model and the measured path loss in HSR hilly terrain scenario. The reason leading to the difference is that the scatters in hilly terrain scenario are richer than those in WINNER II HSR scenario. In short T-R distance, these scattering waves have cancellation impact on the received signal energy. For long T-R distance, there is more scattered energy in this scenario than that in WINNER II HSR scenario.

4.2. Shadow Fading. Shadow fading is the variation of the path loss. After the path loss is obtained, shadow fading can be extracted from the calculated path loss after removing the distance-dependency fitting curve. This channel fading parameter is a variable caused by obstruction. It arises as slow fading, when the coherence time is large relative to the delay constraint of the channel. In most literatures, such as [15–17], the value of shadow fading is often regarded as a random variable conforming to the lognormal distribution. This is certified over a large number of measurement positions along the railway by Table 2.

The comparison results of different distribution fitting methods are presented in Table 2. The Gamma distribution and the Nakagami- m distribution are also used to model the shadow fading [16]. Compared with the other two distributions, the lognormal distribution fitting shows the

TABLE 2: Log likelihood value of different distribution fitting methods.

	Lognormal	Gamma	Nakagami- m
Log likelihood	-4343.36	-4480.30	-4919.28

TABLE 3: Decorrelation distance statistic in hilly terrain.

Decorrelation distance (m)		
Percentile	10%	6.61
	50%	10.28
	90%	32.31
	Mean	14.81

TABLE 4: K-factor statistic in hilly terrain.

K-factor (dB)		
Percentile	10%	-9.05
	50%	-1.42
	90%	4.51
	mean	-1.85

TABLE 5: The comparison of fading parameters in different scenarios.

Scenarios	Viaduct [4]	Hilly terrain
Frequency [GHz]	2.35	2.4
PL component	3.03	2.40/3.88
PL intercept [dB]	12.4	31.31/-11.6
SF STD [dB]	2.0	3.3/4.2
<i>K</i> -factor [dB]	Region 1: 23.05 – 0.0337d	Region 1: 5.10 – 0.0102d
	Region 2: $N(8.25, 1.05)$	Region 2: $N(-1.85, 5.05)$

maximum log likelihood value. It is indicated that lognormal distribution fits the measured shadow fading well.

Figure 4 gives out the statistical characteristics of shadow fading in magnitude of dB. In this figure, the blue bars are the probability distribution function, and the red curve is the normal fitting curve. The standard deviation of the fitting normal distribution is 3.99 dB. Most values in this scenario range from -10 dB to 10 dB. The shadow fading in this scenario is mainly caused by the strong signal reflection from ground, hills, ponds, and buildings.

Shadow fading is often considered roughly constant over the symbol period. But in the HSR scenario, the rapid speed leads to the high Doppler frequency shift and small coherence time, which will influence the design of symbol period. Besides, the long T-R distance caused by rapid speed has a relationship with the change of shadow fading.

Figure 5 shows the relationship between the standard deviation of shadow fading in hilly terrain and the T-R distance. There are two turning points in the blue curve. One is around the position with the T-R distance of 650 m. This position is between the water pond and the measured breakpoint with the distance of 788.6 m. The distance of water pond from the base station is approximately 600 m.

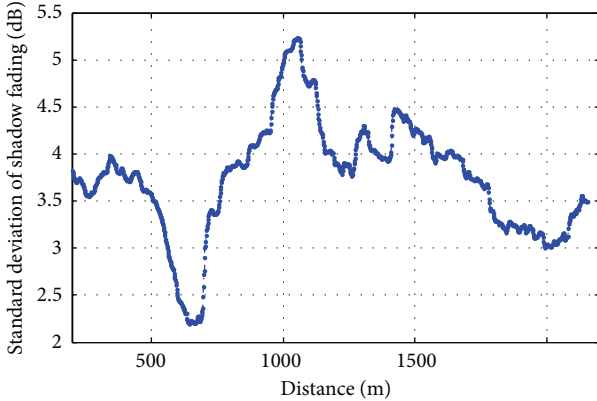


FIGURE 5: Standard deviation of shadow fading in hilly terrain.

The mirror reflection from the water pond is highly powered, which makes the received energy in this region concentrated. So this leads to a deep drop in the curve with the position of 650 m. But with the increasing distance, the opportunity for collecting the different scattering energy also increases. Consequently, the standard deviation of shadow fading is getting larger after this turning point. Another turning point is around the 1050 m similar to the calculated the breakpoint distance in a two-slope model. Beyond the last turning point, the energy of many MPCs is under the noise floor which is discarded in the data process. Then the standard deviation of shadow fading decreases with the increasing distance.

The autocorrelation of shadow fading is often investigated for power control and base station location designing. It is defined as the correlation of shadow fading in different positions under the same base station. The Spatial Channel Model (SCM) [18], 802.16J [19], and M.2135 [20] also give out the reference value and distance-dependent model of autocorrelation of shadow fading. The autocorrelation is described by the correlation coefficient in these documents. The definition is as follows:

$$\rho_{1,2} = \frac{E\{\mathbf{S}(d_1)\mathbf{S}(d_2)\}}{\sigma(d_1)\sigma(d_2)}, \quad (5)$$

where $\mathbf{S}(d_1)$ and $\mathbf{S}(d_2)$ are the values of shadow fading in the position with distance d_1 and d_2 and $\sigma(d_1)$ and $\sigma(d_2)$ are the standard deviations of shadow fading $\mathbf{S}(d_1)$ and $\mathbf{S}(d_2)$, respectively.

Figure 6 shows the autocorrelation coefficient of the shadow fading between the position with T-R distance of 200 m and the positions behind. When the autocorrelation coefficient is less than 0.5, the decorrelation distance d_{cor} is determined. In Figure 6, the decorrelation distance is 10.28 m. This value is smaller than the value of 20 m suggested in 802.16J for vehicular test environment and is also smaller than the value of about 40 m for LOS scenario of RMa in M. 2135. The red dotted line is on the basis of 802.16J model with

$$\rho(\Delta d) = e^{-(|\Delta d|/d_{cor}) \ln 2}, \quad (6)$$

where Δd is the distance between the two observed positions. It seems that there is a little difference between the measured

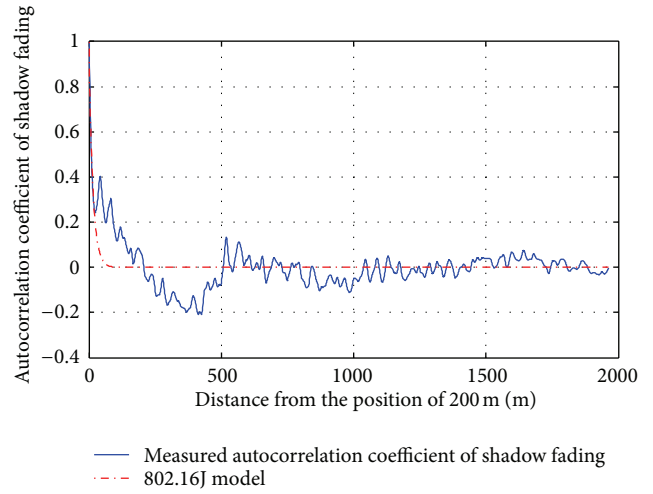


FIGURE 6: Autocorrelation coefficient of shadow fading in hilly terrain.

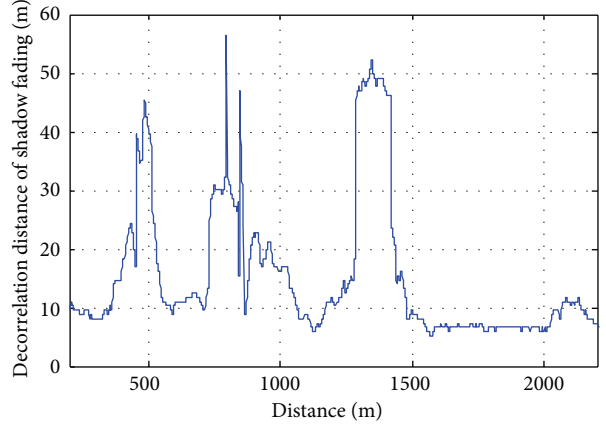


FIGURE 7: Decorrelation distance of shadow fading in hilly terrain.

autocorrelation coefficient and the published model, due to large fluctuations with Δd which is from 100 m to 400 m. These fluctuations are caused by the wave reflection from ground and other scattering objects.

Figure 7 depicts the decorrelation distance of all the positions in the whole route. Each value of decorrelation distance is calculated between the certain position and other positions with the range of 200 m behind. In most cases, the value of decorrelation distance is around 10 m. Due to the observable LOS, the effects of scatters in these locations are small. There are also many positions with decorrelation distance of more than 30 m which is similar to the correlation distance for LOS scenario of RMa in M. 2135. The phenomenon reflects the nonstationary characteristics of large-scale fading parameters. This is the difference between the HSR hilly terrain scenario and custom outdoor scenarios. These positions with larger decorrelation distance often appear before, around, or behind the positions of huge scattering objects, such as the water pond with the distance of 600 m and the huge building with the distance of 1400 m. It is verified that the

reflected waves received by different positions from the same scattering object experience the similar fading, when these receiving positions are at the same direction relative to the same scattering object.

Table 3 shows the statistical results of decorrelation distance. The mean value of decorrelation distance is 14.81 m. In the measured route, 90% of all locations exhibit decorrelation distance less than 32.31 m, and 50% of all positions exhibit decorrelation distance less than 10.28 m. But there are also an amount of positions with a larger decorrelation distance of more than 30 m which exceeds 10%. Therefore, most of the decorrelation distance values are around 10.28 m, but the phenomenon that there is a great difference of the decorrelation distance in different positions is not ignored. The propagation environment with large scattering objects needs special attention for communication system design.

4.3. K-Factor. Fast fading represents a rapid amplitude variation of received signal for movements in the order of a wavelength [21]. For LOS scenario, K-factor is an important parameter for describing the fast fading characteristic of the channel. It is used for describing the ratio of the power of dominant LOS component to the power of Rayleigh NLOS components. The traditional definition is as follows:

$$K \text{ (dB)} = 10 \log_{10} \frac{\rho^2}{\sigma^2}, \quad (7)$$

where ρ^2 is the power of LOS component and σ^2 is the total power of NLOS components [22]. It is assumed that the LOS component is the first arrival of MPCs with the smallest delay. Therefore, these two parameters ρ^2 and σ^2 can be easily calculated with the amplitudes of extracted MPCs in SAGE algorithm. According to the definition, the broadband K-factor is achieved.

Since K-factor is related to the probability of a fade of certain depth, it is critical for improving the communication quality. In traditional view, the high-speed problem can be solved in some degree either through increasing the SNR by 2 dB or through increasing the K-factor by 6 dB [23]. For HSR scenario, the relationship between the K-factor and the T-R distance is worth investigating for system designing.

The relationship between the K-factor and the T-R distance is shown in Figure 8. It is obvious that there are also 2 segments of measured K-factor. The fitting curve is obtained by using the linear least square method in near and far regions. In this figure, the breakpoint of fitting curve might be set as the calculated breakpoint with the T-R distance of 1152 m which is mentioned in the two-slope model of Section 4.1 as well. The expression of the red fitting curve is as follows:

$$K \text{ (dB)} = \begin{cases} 5.10 - 0.0102d, & d < 1152 \text{ m}, \\ -1.19 - 0.0004d, & d \geq 1152 \text{ m}. \end{cases} \quad (8)$$

In the near region, the phenomenon that median of K-factor decreases linearly with increasing T-R distance is verified as depicted in [21]. The traditional explanation is that the signal power decay is logarithmic with distance, and the

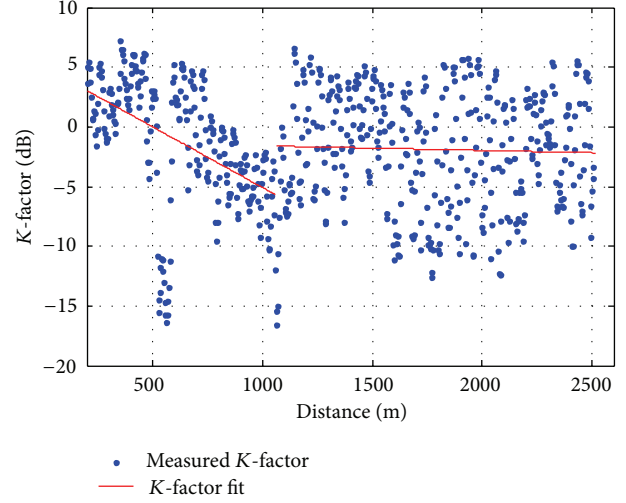


FIGURE 8: K-factor in hilly terrain.

decreasing power of multipath components is much smaller than the decreasing power of LOS one when the distance increases. The standard deviation between the measured K-factor and fitting curve is approximately limited to 3 dB. In the far region, the values of the red fitting curve lie between -1.5 and -2.5 dB. It is indicated that K-factor suffers fluctuation which is often estimated as a Gaussian variable [23] with the mean value of -1.85 dB and the standard deviation of 5.05 dB. The K-factor value for 10%, 50%, and 90% points of the cumulative distribution function (CDF) of the Ricean K-factor in far region can be found in Table 4. From Table 4, the K-factor values of 50% and 90% positions are lower than -1.42 dB and 4.51 dB, respectively. The mean K-factor value of all positions is -1.85 dB. Most of K-factor values are near 0 dB. There are also 10% of positions in far region with a K-factor less than -9 dB. This means that the power of LOS path remains at a low level in the measured route. Actually in some cases, the LOS signal is not the strongest signal. These cases include the impact of the main scattering objects and the long distance transmission. The results are statistically significant.

This result of K-factor is different from the WINNER II HSR result of measured K-factor. In WINNER II HSR result, the K-factor is constant over the measured distance. As Figure 8 indicates, the K-factor has its own special characteristic in different positions of the hilly terrain scenario. For example, the water pond which caused the strong specular reflection in the T-R distance of about 600 m is mentioned once again. The K-factor has an extreme low value.

4.4. Comparison with Viaduct Scenario. Viaduct is another typical scenario in HSR scenarios. Table 5 compares the results of the channel fading parameters in viaduct scenario and the results in hilly terrain scenario. The viaduct measurement is conducted in the Beijing-Tianjin HSR by the Beijing Jiaotong University with an EB CS radio channel sounder Propsound at a frequency of 2.35 GHz with 10 MHz band

width [4]. The second is the measured hilly terrain scenario in this paper.

Although differences exist in measurement frequency and other aspects, the comparison between two measurements is still meaningful. In Table 5, the distinction of channel parameters between two scenarios is obvious. Compared with the viaduct scenario, the measured path loss in hilly terrain is divided into two parts with a breakpoint. The path loss component of the first region in hilly terrain is smaller than the value in viaduct, but the value of second region in hilly terrain is larger than that in viaduct. Due to the rapidly changing propagation environment along the measured route, the standard deviation of shadow fading in hilly terrain is larger than that in viaduct. The rich scattering environment of hilly terrain also leads to smaller K -factor, compared with viaduct. The difference of fading characteristics between viaduct and hilly terrain indicates that the work on HSR hilly terrain measurement and modeling is necessary for general applicability of HSR.

5. Conclusions

Through the use of the high-resolution SAGE algorithm in HSR hilly terrain scenario, the statistical fading characteristic of wireless channel parameters has been analyzed in this paper. The HSR hilly terrain scenario is characterized by an obvious LOS component, complex scattering propagation environment, and rapid change of propagation condition due to high speed. On the whole, our measurement results are supported by the fact that the values of fading parameters are changing with time or T-R distance.

In the analysis, the path loss, shadow fading, and K -factor are investigated. Compared with the free space path loss model, the measured path loss value in hilly terrain scenario suffers greater decay and shows the property of having a breakpoint distance as the WINNER HSR model shows. The shadow fading is a parameter for describing the slow fading characteristic. It is lognormal fitting and changed with two turning points. As an important point of interest, the autocorrelation of shadow fading is investigated. It is exhibited that the mean value of decorrelation distance is around 14 m. But the value will rise up when the train gets near to the huge reflectors. The K -factor as a fast fading parameter is also influenced by the breakpoint distance. Within the breakpoint distance, K -factor decreases as the T-R distance increases. Beyond the break point distance, the value of K -factor fluctuates dramatically. These results are compared with the published results in viaduct scenario, and the difference between viaduct and hilly terrain is summarized. The results of this paper can be utilized to build a position-based channel fading model and amend the existing channel models for HSR hilly terrain scenario. And this is also hoped to serve as a reference for future HSR communication system design, evaluation, and improvement.

Acknowledgments

This work has been partially supported by the National Basic Research Program of China (2012CB316002), National

Natural Science Foundation of China (61201192), Tsinghua University Initiative Scientific Research Program (2011-081025), National S&T Major Project (2013ZX03001024), International S&T Cooperation Program (2012DFG12010), Tsinghua-Qualcomm Joint Research Program, China Postdoctoral Science Foundation, and Open Research Fund of National Mobile Communication Research Laboratory, Southeast University. The authors also would like to thank Mr. Zhenghui Li, Wenzhen Pang, and Yuejian Zhou for their help in the basic work of channel measurement.

References

- [1] http://en.wikipedia.org/wiki/High-speed_rail.
- [2] P. Lukasazewics and E. Anderson, "Green train energy consumption, estimation on high-speed rail operation," Tech. Rep. 978-91-7415-257-9, KTH Railway Group, Stockholm, Sweden, 2009.
- [3] J. Li and M. Kavehrad, "Effects of time selective multipath fading on OFDM systems for broadband mobile applications," *IEEE Communications Letters*, vol. 3, no. 12, pp. 332–334, 1999.
- [4] L. Liu, C. Tao, J. Qiu et al., "Position-based modeling for wireless channel on high-speed railway under a viaduct at 2.35 GHz," *IEEE Journal on Selected Areas in Communications*, vol. 30, pp. 834–845, 2012.
- [5] P. Aikio, R. Gruber, and P. Vainikainen, "Wideband radio channel measurements for train tunnels," in *Proceedings of the 48th IEEE Vehicular Technology Conference (VTC '98)*, pp. 460–464, Ottawa, Ontario, Canada, May 1998.
- [6] D. J. Cichon, T. Zwick, and W. Wiesbeck, "Ray optical modeling of wireless communications in high-speed railway tunnels," in *Proceedings of the IEEE 46th Vehicular Technology Conference (VTC '96)*, pp. 546–550, Atlanta, Ga, USA, May 1996.
- [7] L. Gao, Z. Zhong, B. Ai, and L. Xiong, "Estimation of the Ricean K factor in the high speed railway scenarios," in *Proceedings of the 5th International ICST Conference on Communications and Networking in China (ChinaCom '10)*, Beijing, China, August 2010.
- [8] J. Qiu, C. Tao, L. Liu, and Z. Tan, "Broadband channel measurement for the high-speed railway based on WCDMA," in *Proceedings of the IEEE 75th Vehicular Technology Conference (VTC '12-Spring)*, pp. 1–5, Yokohama, Japan, May 2012.
- [9] A. Ghazal, C. X. Wang, H. Haas, M. A. Beach, X. Lu, and D. Yuan, "A non-stationary MIMO channel model for high speed train communication systems," in *Proceedings of the IEEE 75th Vehicular Technology Conference (VTC '12-Spring)*, pp. 347–351, Yokohma, Japan, May 2012.
- [10] Google Maps, <http://maps.google.com.hk/>.
- [11] Y. Rui, Y. Zhang, S. Liu, and S. Zhou, "3.52 GHz MIMO radio channel sounder," in *Proceedings of the International Conference on Communications, Circuits and Systems (ICCCAS '08)*, pp. 79–83, May 2008.
- [12] WINNER2 WPI, "Measurement results and analysis items," Internal Report IR1.1.230.9.2006, 2006.
- [13] B. H. Fleury, M. Tschudin, R. Heddergott, D. Dahlhaus, and K. I. Pedersen, "Channel parameter estimation in mobile radio environments using the SAGE algorithm," *IEEE Journal on Selected Areas in Communications*, vol. 17, no. 3, pp. 434–450, 1999.
- [14] S. Wyne, A. F. Molisch, P. Almers, G. Eriksson, J. Karedal, and F. Tufvesson, "Outdoor-to-indoor office MIMO measurements

- and analysis at 5.2 GHz,” *IEEE Transactions on Vehicular Technology*, vol. 57, no. 3, pp. 1374–1386, 2008.
- [15] WINNER2 WP1, “Radio channel measurement and analysis results,” Deliverable D 1.1.2, ver 1.0. 30.9.2007, 2007.
 - [16] J. Salo, L. Vuokko, and P. Vainikainen, “Why is shadow fading lognormal?” in *Proceedings of the International Symposium on Wireless Personal Multimedia Communications*, pp. 522–526, Aalborg, Denmark, September 2005.
 - [17] I. Forkel, M. Schinzenburg, and M. Ang, “Generation of two-dimensional correlated shadowing for mobile radio network simulation,” in *Proceedings of the Wireless Personal Multimedia Communications (WPMC '04)*, pp. 314–319, Abano Terme, Italy, September 2004.
 - [18] 3GPP TR 25.996, “3rd Generation Partnership Project; technical specification group radio access networks; spatial channel model for MIMO simulations (release 6),” V6.1.0.
 - [19] “Multi-hop relay system evaluation methodology (Channel model and performance metrics),” IEEE802.16j-06/013r3, 2007.
 - [20] ITU-R, “Guidelines for evaluation of radio interface technologies for IMT-Advanced,” Tech. Rep. ITU-R M.2135, 2008.
 - [21] Z. Wang, E. K. Tameh, and A. R. Nix, “Statistical peer-to-peer channel models for outdoor urban environments at 2 GHz and 5 GHz,” in *Proceedings of the IEEE 60th Vehicular Technology Conference (VTC '04-Fall)*, pp. 5101–5105, September 2004.
 - [22] W. H. Jeong, J. S. Kim, M. Jung, and K. Kim, “MIMO channel measurement and analysis for 4G mobile communication,” *Computer Science*, vol. 7425, pp. 678–682, 2012.
 - [23] M. Goller, “Application of GSM in high speed trains: measurement and simulations,” *IEEE Colloquium on Radio communications in Transportation*, pp. 5/1–5/7, 1995.

Research Article

Positive Effect of Severe Nakagami- m Fading on the Performance of Multiuser TAS/MRC Systems with High Selection Gain

Chia-Chun Hung,¹ Ching-Tai Chiang,² Rong-Ching Wu,³ and C. Lee⁴

¹Instrument Technology Research Center, National Applied Research Laboratories, 20 R&D VI Road, Hsinchu Science-Based Industrial Park, Hsinchu 300, Taiwan

²Department of Computer and Communication, National Pingtung Institute of Commerce, 51 Min Sheng E. Road, Pingtung 900, Taiwan

³Department of Electrical Engineering, I-Shou University, No.1, Section 1, Syuecheng Road, Dashu District, Kaohsiung 84001, Taiwan

⁴Department of Mechanical and Automation Engineering, I-Shou University, No.1, Section 1, Syuecheng Road, Dashu District, Kaohsiung 84001, Taiwan

Correspondence should be addressed to Ching-Tai Chiang, cctai@npic.edu.tw

Received 24 June 2012; Revised 8 November 2012; Accepted 9 November 2012

Academic Editor: Min Zhang

Copyright © 2012 Chia-Chun Hung et al. This is an open access article distributed under the Creative Commons Attribution License, which permits unrestricted use, distribution, and reproduction in any medium, provided the original work is properly cited.

This paper investigates the positive effect of severe Nakagami- m fading on the performance of multiuser transmit antenna selection/maximal-ratio combining (TAS/MRC) systems with high selection gain. Both amount of fading (AF) and symbol error rate (SER) of M -QAM are derived as closed-form expressions for integer m . For arbitrary m , the AF and the SER are expressible as a single infinite series of Gamma function and Gauss hypergeometric function, respectively. The analytical results lead to the following observations. First, the SER performance can demonstrate the positive effect of severe Nakagami- m fading on multiuser TAS/MRC systems with high selection gain. Second, the AF performance only exhibits the negative impact of severe fading regardless of high selection gain. Last, the benefit of severe fading to the system performance diminishes at high signal-to-noise ratio (SNR).

1. Introduction

Multiple-input multiple-output (MIMO) communications have been considered as suitable ways to improve the performance of wireless communications. Various MIMO transmission schemes have been developed to obtain a high reliability through promised diversity gain and/or high rate transmission via spatial multiplexing (SM) [1–6]. Rectangular quadrature amplitude modulation (QAM) is a general modulation technique which includes important modulation schemes as particular cases, such as binary phase-shift keying (BPSK), pulse amplitude modulation (PAM), or square QAM. Although MIMO maximum-ratio combining (MRC) systems under different conditions have been investigated in the last few years, no results seem to be available for the average symbol error rate (SER) of

rectangular QAM in noise-limited environments. In [7], an expression for the bit error rate (BER) of rectangular QAM is derived, yet the result is only valid for Gray code mapping, and no expression for the average SER is provided.

More specifically, the diverse techniques of coherent signal combining were developed depending on the specific treatment of the combined signals' phase and amplitude, which are selection combining (SC), threshold combining, equal-gain combining (EGC) and MRC, as summarized in [8, 9]. Choosing a single transmit antenna, the one that maximizes the total received signal power at the receiver, can substantially reduce the transmitter's hardware and software complexity. Thus, the transmit antenna selection (TAS) has occupied a considerable part of today's communication researches [10]. On the other hand, MRC is an optimal diversity technique with a maximum SNR

criterion. To retain the advantages of both TAS and MRC, an integrated TAS scheme with MRC at the receiver, labeled TAS/MRC, was proposed [11]. Besides the antenna diversity, multiuser diversity (MUD) is also utilized to improve performance in point-to-multipoint communication [12]. A proper scheduling algorithm is the key to gain the MUD in the multiuser systems [12]. Moreover, multiuser MIMO systems have recently attracted much attention as the technology enhances the total system capacity by generating a virtual large MIMO channel between a base station and multiple terminal stations [13]. In [14], tight closed-form expressions of outage performance were derived for the multiuser MIMO systems in Rayleigh fading channels. The analytical results demonstrate that users can be viewed as equivalent “virtual” transmit antennas [15]. The published papers are mainly focused on flat Rayleigh channels [11, 14, 15]. The closed-form expressions for the average symbol error rate of general rectangular QAM in MIMO MRC systems over Rayleigh fading channels are derived [16].

Via the m parameter, Nakagami model is able to cover both severe and weak fadings, which includes the Rayleigh fading ($m = 1$) as a special case. The Nakagami- m distribution also can closely approximate the Hoyt distribution and the Rice distribution [17]. Therefore, the Nakagami- m channels are usually used to model land-mobile, indoor mobile multipath propagation, as well as scintillating ionospheric radio links [17]. The severity of fading can be quantified by the amount of fading (AF) [17]. In [18], a closed-form expression for the AF was derived in a MIMO diversity system with space-time block coding (STBC) in Nakagami- m fading channels. In this paper, we derive the AF of multiuser TAS/MRC systems as a closed-form expression in independent and identically distributed (i.i.d.) Nakagami- m channels with a positive integer m . For arbitrary m , the AF is expressible as a single infinite series of Gamma function. The analytical results show that the AF of multiuser TAS/MRC systems decreases as m increases as expected. The positive effect of severe fading, however, cannot be observed from the standpoint of AF.

Performance analyses, including outage probability, capacity, and symbol error rate (SER), were investigated for the TAS/MRC systems in Nakagami- m fading channels in [19–21]. The performance is improved with the increase of m , that is, in weak fading channels [19–21]. However, the tendency becomes totally different because the paper [22] presented that the higher m causes a negative impact on the capacity of multiuser MIMO systems. In this paper, the performance of TAS/MRC system with MUD in Nakagami- m fading channels is analyzed. We derive a simple closed-form expression for the outage probability of multiuser TAS/MRC systems. Moreover, a closed-form SER of M -ary quadrature amplitude modulation (M -QAM) is also derived when m is an integer. For arbitrary m , the SER of M -QAM is expressible as a single infinite series of a Gauss hypergeometric function. The analytical results suggest that the effect of severe fading on the performance becomes beneficial at high

selection gain, since a more scattering fading environment enables the selection scheduler to arrange transmissions at higher peaks of channel fading. Thus, the systems with high selection gain perform better in severe fading than in weak fading. However, the high signal-to-noise ratio (SNR) may dilute the function of selection scheduler in transmitters. All the derived expressions are verified by Monte Carlo simulations.

2. Amount of Fading for Nakagami- m Models

We consider a TAS/MRC system with a base station serving K users in the downlink. The best transmit antenna out of all L_T transmit candidates, which maximizes the postprocessing SNR at the MRC output of L_R received antennas, is selected to transmit data for the corresponding user. The channels between the transmit antennas and the users experience fading paths which are modeled as i.i.d. Nakagami- m fading channels. The probability density function (PDF) of the instantaneous postprocessing SNR of MRC combiner output for the k th user with respect to the i th transmit antenna is given by

$$f(\gamma_{i,k}) = \left(\frac{m}{\bar{\gamma}} \right)^{mL_R} \frac{\gamma_{i,k}^{mL_R-1}}{\Gamma(mL_R)} \exp\left(-\frac{m\gamma_{i,k}}{\bar{\gamma}}\right), \quad (1)$$

where $\Gamma(\cdot)$ denotes the Gamma function and $\bar{\gamma}$ is the average SNR per symbol per branch. Then, the corresponding cumulative distribution function (CDF) denoted by $F(\gamma_{i,k})$ leads to

$$F(\gamma_{i,k}) = \int_0^{\gamma_{i,k}} f(x)dx = \frac{\gamma(mL_R, (m\gamma_{i,k}/\bar{\gamma}))}{\Gamma(mL_R)}, \quad (2)$$

where $\gamma(y, z)$ is the incomplete Gamma function [23, equation (8.350.1)]. For MUD in the TAS/MRC scheme, which is denoted as a (L_T, L_R, K) multiuser TAS/MRC system, the scheduler at BS collects the MRC output SNR of all users and selects the target user according to the criterion

$$\gamma = \max_{\substack{i=1,2,\dots,L_T \\ k=1,2,\dots,K}} \gamma_{i,k}. \quad (3)$$

Then, the selected PDF of effective postprocessing SNR in (3) can be expressed as [19, equation (4)]

$$\begin{aligned} f_I(\gamma) &= KL_T [F(\gamma)]^{KL_T-1} f(\gamma) \\ &= \frac{KL_T}{[\Gamma(mL_R)]^{KL_T}} \left(\frac{m}{\bar{\gamma}} \right)^{mL_R} \gamma^{mL_R-1} \\ &\quad \times \exp\left(-\frac{m\gamma}{\bar{\gamma}}\right) \left[\gamma \left(mL_R, \frac{m\gamma}{\bar{\gamma}} \right) \right]^{KL_T-1}. \end{aligned} \quad (4)$$

Integrating (4), we can obtain the CDF as

$$F_I(\gamma) = [F(\gamma)]^{KL_T} = \left[\frac{\gamma(mL_R, (m\gamma/\bar{\gamma}))}{\Gamma(mL_R)} \right]^{KL_T}. \quad (5)$$

From (3)–(5), one can see that the effective antenna selection gain is KL_T , since the users can be viewed as equivalent virtual transmit antennas [15]. We propose an expansion of the incomplete Gamma function in (4) by a series development for $\gamma(mL_R, my/\bar{y})$, namely:

$$\begin{aligned} & \gamma\left(mL_R, \frac{my}{\bar{y}}\right) \\ = & \begin{cases} \exp\left(-\frac{my}{\bar{y}}\right) \sum_{n=0}^{\infty} \frac{\Gamma(mL_R)(my/\bar{y})^{n+mL_R}}{\Gamma(mL_R + n + 1)}, \\ \quad \text{real } m \geq \frac{1}{2}, \\ \Gamma(mL_R) \left[1 - \exp\left(-\frac{my}{\bar{y}}\right) \sum_{n=0}^{mL_R-1} \frac{(my/\bar{y})^n}{n!} \right], \\ \quad \text{positive integer } m. \end{cases} \end{aligned} \quad (6)$$

Next, using (6), we may infer the expansion of $[\gamma(mL_R, my/\bar{y})]^{KL_T-1}$ by the power series raised to powers [23, equation (0.314)] as follows:

$$\begin{aligned} & \left[\gamma\left(mL_R, \frac{my}{\bar{y}}\right) \right]^{KL_T-1} \\ = & \begin{cases} \sum_{n=0}^{\infty} \alpha_n \left(\frac{my}{\bar{y}}\right)^{mL_R(KL_T-1)+n} \\ \times \exp\left(-\frac{my(KL_T-1)}{\bar{y}}\right), \\ \quad \text{real } m \geq \frac{1}{2}, \\ [\Gamma(mL_R)]^{KL_T-1} \sum_{j=0}^{KL_T-1} \binom{KL_T-1}{j} (-1)^j \\ \times \exp\left(-j\frac{my}{\bar{y}}\right) \sum_{n=0}^{j(mL_R-1)} \beta_n \left(\frac{my}{\bar{y}}\right)^n, \\ \quad \text{positive integer } m, \end{cases} \end{aligned} \quad (7)$$

where α_n is the coefficient of $(my/\bar{y})^{mL_R(KL_T-1)+n}$ in the expansion of

$$\left\{ \sum_{n=0}^{\infty} \frac{\Gamma(mL_R)(my/\bar{y})^{mL_R+n}}{\Gamma(mL_R + 1 + n)} \right\}^{KL_T-1}, \quad (8)$$

and [19, equation (6)]

$$\begin{aligned} \alpha_0 &= \left(\frac{1}{mL_R}\right)^{KL_T-1}, \\ \alpha_n &= \frac{\Gamma(mL_R + 1)}{n} \sum_{z=1}^n \frac{zKL_T - n}{\Gamma(mL_R + 1 + z)} \alpha_{n-z}, \quad \text{for } n \geq 1. \end{aligned} \quad (9)$$

β_n in (7) is the coefficient of $(my/\bar{y})^n$ in the expansion of $\{\sum_{n=0}^{mL_R-1} 1/n!(my/\bar{y})^n\}^j$, and [19, equation (9)]

$$\beta_0 = 1, \quad \beta_n = \frac{1}{n} \sum_{k=1}^{\min(n, mL_R-1)} \frac{k(j+1) - n}{k!} \beta_{n-k}, \quad \text{for } n \geq 1. \quad (10)$$

Thus, substituting (7) into (4), we can rewrite the PDF of the multiuser TAS/MRC systems as

$$f_I(y) = \begin{cases} \frac{KL_T}{[\Gamma(mL_R)]^{KL_T}} \sum_{n=0}^{\infty} \alpha_n \left(\frac{m}{\bar{y}}\right)^{mKL_TL_R+n} \\ \times \gamma^{mKL_TL_R+n-1} \exp\left(-KL_T \frac{my}{\bar{y}}\right), \\ \quad \text{real } m \geq \frac{1}{2}, \\ \frac{KL_T}{\Gamma(mL_R)} \sum_{j=0}^{KL_T-1} \binom{KL_T-1}{j} (-1)^j \\ \times \sum_{n=0}^{j(mL_R-1)} \beta_n \left(\frac{m}{\bar{y}}\right)^{mL_R+n} \\ \times \gamma^{mL_R+n-1} \exp\left(-[j+1] \frac{my}{\bar{y}}\right), \\ \quad \text{positive integer } m. \end{cases} \quad (11)$$

Similar to (11), the CDF of (5) can be expanded as

$$F_I(y) = \begin{cases} \sum_{n=0}^{\infty} \eta_n \left(\frac{my}{\bar{y}}\right)^{mKL_TL_R+n} \exp\left(-KL_T \frac{my}{\bar{y}}\right), \\ \quad \text{real } m \geq \frac{1}{2} \\ \sum_{j=0}^{KL_T} \binom{KL_T}{j} (-1)^j \\ \times \sum_{n=0}^{j(mL_R-1)} \beta_n \left(\frac{my}{\bar{y}}\right)^n \exp\left(-j \frac{my}{\bar{y}}\right), \\ \quad \text{positive integer } m, \end{cases} \quad (12)$$

where

$$\eta_0 = \left(\frac{1}{\Gamma(mL_R + 1)}\right)^{KL_T},$$

$$\eta_n = \frac{\Gamma(mL_R + 1)}{n} \sum_{z=1}^n \frac{z(KL_T + 1) - n}{\Gamma(mL_R + 1 + z)} \eta_{n-z}, \quad \text{for } n \geq 1. \quad (13)$$

From (11), we can obtain the expectation and the second moment of effective SNR γ by the following expressions [20, equations (7), (8)]:

$$\begin{aligned} \mu_{\gamma} &= \frac{(\bar{y}/m)}{[\Gamma(mL_R)]^{KL_T}} \\ &\times \sum_{n=0}^{\infty} \alpha_n \frac{\Gamma(mKL_TL_R + n + 1)}{L_T^{mKL_TL_R+n}}, \quad \text{real } m \geq \frac{1}{2}, \end{aligned} \quad (14a)$$

$$\begin{aligned} \mu_{\gamma} &= \frac{KL_T(\bar{y}/m)}{\Gamma(mL_R)} \sum_{j=0}^{KL_T-1} \binom{KL_T-1}{j} (-1)^j \\ &\times \sum_{n=0}^{j(mL_R-1)} \beta_n \frac{\Gamma(mL_R + n + 1)}{(j+1)^{mL_R+n+1}}, \quad \text{positive integer } m, \end{aligned} \quad (14b)$$

$$\begin{aligned} E[\gamma^2] &= \frac{(\bar{\gamma}/m)^2}{[\Gamma(mL_R)]^{KL_T}} \\ &\times \sum_{n=0}^{\infty} \alpha_n \frac{\Gamma(mKL_T L_R + n + 2)}{L_T^{mKL_T L_R + n + 1}}, \quad \text{real } m \geq \frac{1}{2}, \end{aligned} \quad (15a)$$

$$\begin{aligned} E[\gamma^2] &= \frac{KL_T (\bar{\gamma}/m)^2}{\Gamma(mL_R)} \sum_{j=0}^{KL_T-1} \binom{KL_T - 1}{j} (-1)^j \\ &\times \sum_{n=0}^{j(mL_R-1)} \beta_n \frac{\Gamma(mL_R + n + 2)}{(j+1)^{mL_R+n+2}}, \quad \text{positive integer } m. \end{aligned} \quad (15b)$$

Using (14a), (14b), (15a), and (15b) yields the variance of the effective system SNR:

$$\sigma_\gamma^2 = E[\gamma^2] - \mu_\gamma^2. \quad (16)$$

Accordingly, from (14a)–(16), the quantity of AF for the multiuser TAS/MRC systems can be computed by

$$AF = \frac{\sigma_\gamma^2}{\mu_\gamma^2}. \quad (17)$$

3. Performance Analysis: Outage Probability and SER

The outage probability is defined as the probability that the instantaneous capacity is less than a given capacity C [19], that is:

$$\begin{aligned} P_{\text{out}}(C, \text{SNR}) &= \Pr\{\log_2[1 + \text{SNR}(\gamma)] < C\} \\ &= \Pr\{\text{SNR} < (2^C - 1)\}. \end{aligned} \quad (18)$$

Then, in light of the CDF in (5), we can express the outage probability for the multiuser TAS/MRC systems as

$$\begin{aligned} P_{\text{out}}(C, \text{SNR}) &= F_I(2^C - 1) \\ &= \left[\frac{\gamma(mL_R, ((2^C - 1)m)/\bar{\gamma})}{\Gamma(mL_R)} \right]^{KL_T}. \end{aligned} \quad (19)$$

On the other hand, the SER for M -QAM is given by [24, equation (31)]

$$P_{\text{QAM}}(\gamma) = aQ(\sqrt{b\gamma}) - cQ^2(\sqrt{b\gamma}), \quad (20)$$

where $Q(x) = (\sqrt{2\pi})^{-1} \int_x^\infty \exp(-z^2/2) dz$ is the Gaussian Q-function, $(a, b, c) = (4(\sqrt{M} - 1)/\sqrt{M}, 3/(M - 1), 4(\sqrt{M} - 1)^2/M)$. Then, the derivative of (20) is [24, equation (32)]

$$\begin{aligned} P'_{\text{QAM}}(\gamma) &= (c - a) \sqrt{\frac{b}{8\pi\gamma}} e^{-b\gamma/2} \\ &- \frac{cb}{2\pi} e^{-b\gamma} {}_1F_1\left(1; \frac{3}{2}; \frac{b\gamma}{2}\right), \end{aligned} \quad (21)$$

where ${}_1F_1(\cdot; \cdot; \cdot)$ is the confluent hypergeometric function [23, equation (9.210.2)].

Using the integral-by-parts method, the average SER in fading channels is given by

$$P_{\text{SER}} = \int_0^\infty f_I(\gamma) P_{\text{QAM}}(\gamma) d\gamma = - \int_0^\infty F_I(\gamma) P'_{\text{QAM}}(\gamma) d\gamma. \quad (22)$$

Substituting (12) and (21) into (22), we obtain the SER for M -QAM for real $m \geq 1/2$ as

$$\begin{aligned} P_{\text{SER}} &= \frac{1}{2} \sum_{n=0}^{\infty} \eta_n \cdot \left(\frac{m}{\bar{\gamma}}\right)^{mKL_T L_R + n} \\ &\times \left\{ \sqrt{\frac{b}{2\pi}} \frac{(a - c)\Gamma(mKL_T L_R + n + 0.5)}{(mKL_T/\bar{\gamma} + b/2)^{mKL_T L_R + n + 0.5}} \right. \\ &+ \frac{bc}{\pi} \frac{\Gamma(mKL_T L_R + n + 1)}{(mKL_T/\bar{\gamma} + b)^{mKL_T L_R + n + 1}} \\ &\times {}_2F_1\left(mKL_T L_R + n + 1, 1; \frac{3}{2}; \frac{b}{2(mKL_T/\bar{\gamma} + b)}\right) \Big\}, \\ &\text{real } m \geq \frac{1}{2}, \end{aligned} \quad (23)$$

where we have used the relation [23, equation (7.621.4)]

$$\begin{aligned} &\int_0^\infty \exp(-st) t^{d-1} {}_1F_1(f; g; kt) dt \\ &= \frac{\Gamma(d)}{s^d} {}_2F_1\left(f, d; g; \frac{k}{s}\right) \end{aligned} \quad (24)$$

and ${}_2F_1(\cdot, \cdot; \cdot; \cdot)$ is the Gauss hypergeometric function [23, equation (9.14.1)]. Similarly, while the fading parameter m is a positive integer, we obtain a closed form as

$$\begin{aligned} P_{\text{SER}} &= \frac{1}{2} \sum_{j=0}^{KL_T} \binom{KL_T}{j} (-1)^j \sum_{n=0}^{j(mL_R-1)} \beta_n \cdot \left(\frac{m}{\bar{\gamma}}\right)^n \\ &\times \left\{ \sqrt{\frac{b}{2\pi}} \frac{(a - c)\Gamma(n + 0.5)}{(mj/\bar{\gamma} + b/2)^{n+0.5}} + \frac{bc}{\pi} \frac{\Gamma(n + 1)}{(mj/\bar{\gamma} + b)^{n+1}} \right. \\ &\times {}_2F_1\left(1, n + 1; \frac{3}{2}; \frac{b}{2(mj/\bar{\gamma} + b)}\right) \Big\}, \\ &\text{positive integer } m. \end{aligned} \quad (25)$$

4. Numerical and Simulation Results

In this section, we use the MATLAB software to present the numerical and simulation results of performance. The Nakagami- m samples are generated by the square root of

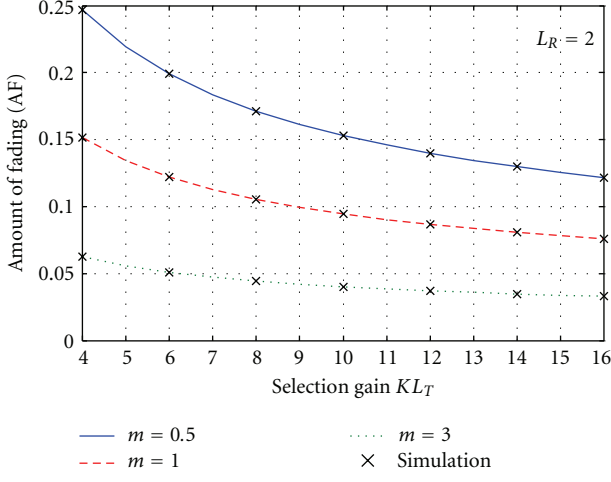


FIGURE 1: The amount of fading (AF) of multiuser TAS/MRC systems against the selection gain KL_T in various Nakagami- m fading channels when $L_R = 2$ and $\bar{\gamma} = 0$ dB.

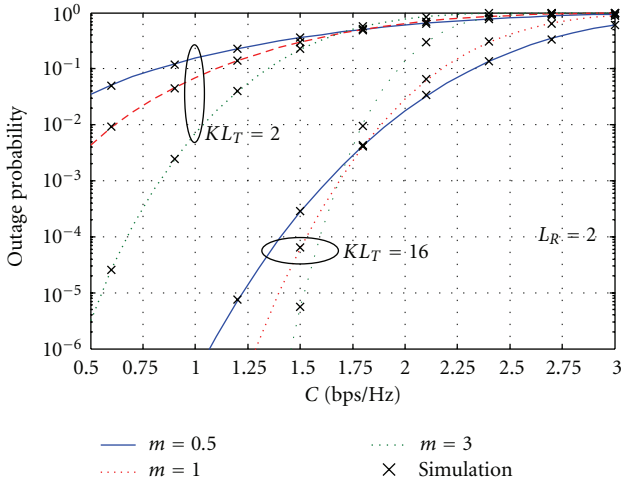


FIGURE 2: Outage probability against the capacity for both low and high selection gains when $L_R = 2$ and $\bar{\gamma} = 0$ dB.

Gamma distributed samples (i.e., the $\text{gmrnd}(\cdot)$ MATLAB function) [25]. The outage probability and the SER were simulated by the ratios when 10^4 outages and 10^4 symbol errors occurred, respectively. All the simulations, marked by the “ \times ” symbols, agree closely with the analytic curves, validating the theoretical derivation. The number of received antenna L_R is chosen as 2 in all scenarios.

Figure 1 depicts the AF of the multiuser TAS/MRC systems against the selection gain KL_T in various Nakagami- m fading channels. The curves with $\bar{\gamma} = 0$ dB are plotted, using (14a) and (15a) for $m = 0.5$ by truncating the infinite series to 50 terms. It can be seen that the AF decreases as m increases; even the selection gain increases from 4 to 16. In other words, the fading index AF can quantify the severity of channel fading. For the high selection gain, however, the benefit of severe fading cannot be exhibited from

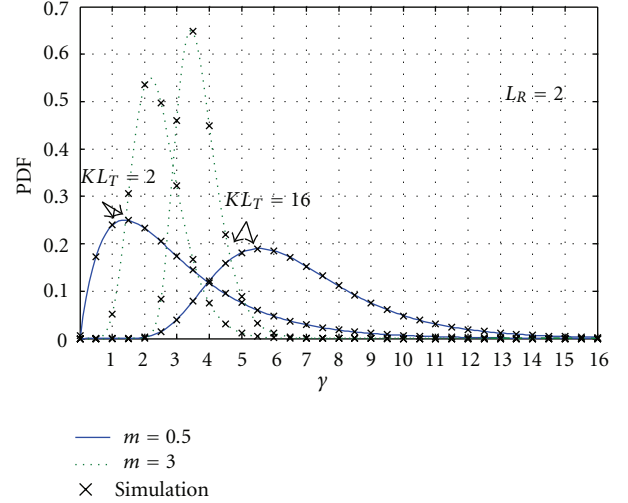


FIGURE 3: PDF of multiuser TAS/MRC systems with both low and high selection gains when $L_R = 2$ and $\bar{\gamma} = 0$ dB.

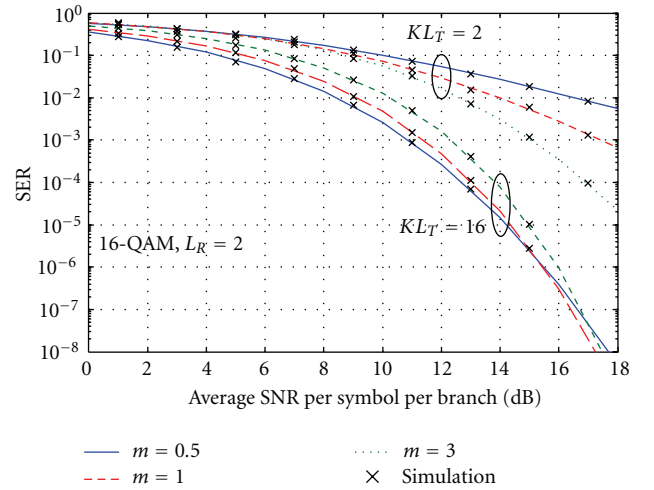


FIGURE 4: SER of 16-QAM against average SNR per symbol per branch when $L_R = 2$.

the tendency of AF. Figure 2 shows the outage probability with $\bar{\gamma} = 0$ dB against the capacity for both low and high selection gains. The outage probability with the low selection gain ($KL_T = 2$) mostly performs better for the higher values of m , except that the outage probability already exceeds about 50%. On the other hand, the positive effect of severe fading on the performance is clearly demonstrated at the high selection gain ($KL_T = 16$). It is worth noting that the advantage of severe fading occurs in the outage range of practical interest. For example, the outage probability exceeds about 3×10^{-3} when the capacity is required larger than about 1.7 bps/Hz. The positive effect is further illustrated by the PDF values using (11) when $\bar{\gamma} = 0$ dB in Figure 3. As the selection gain increases from 2 to 16, the PDF values for $m = 0.5$ shift to right much more than those for $m = 3$. In the severe fading channel, indeed, the selection

gain boosts the probability to distribute the PDF values over a higher instantaneous SNR region and hence demonstrates the positive effect.

In Figure 4, the SERs are plotted for the considered systems with 16-QAM in various fading channels. The SER for $m = 0.5$ is evaluated by (23) with truncation (50 terms) for the infinite series. As expected, the SER performs better in the weak fading channels at low selection gain. However, the tendency becomes contrary for the SERs at high selection gain. It can be seen that the SER for $m = 0.5$ performs best until \bar{y} is higher than about 15 dB, and the SER is smaller than the order of 10^{-5} . Obviously, the signal with high SNR will dilute the character of severe fading even at high selection gain.

5. Conclusions

In general, system performance behaves better in weak fading channels than in severe fading channels. This paper presents a positive impact of severe Nakagami- m fading on the performance of multiuser TAS/MRC systems with high selection gain. The scheduler with high selection gain is the key to arrange the transmission at higher peaks in a more scattering fading channel. Two performance indexes, AF and SER of M -QAM, are derived as closed-form expressions for integer m . For arbitrary m , the AF and the SER are expressible as a single infinite series of Gamma function and Gauss hypergeometric function, respectively. Although the AF is unable to illustrate the benefit of severe fading, from the analytical and numerical results, we validate the favorable effect from the results of PDF, outage probability and SER, occurring in the range of practical interest.

Acknowledgment

The authors thank the anonymous referees for helpful comments. This research was supported by the Instrument Technology Research Center, National Applied Research Laboratories, and NSC 100-2221-E-251-004.

References

- [1] V. Tarokh, H. Jafarkhani, and A. R. Calderbank, "Space-time block codes from orthogonal designs," *IEEE Transactions on Information Theory*, vol. 45, no. 5, pp. 1456–1467, 1999.
- [2] G. D. Golden, C. J. Foschini, R. A. Valenzuela, and P. W. Wolniansky, "Detection algorithm and initial laboratory results using V-BLAST space-time communication architecture," *Electronics Letters*, vol. 35, no. 1, pp. 14–16, 1999.
- [3] S. Sandhu and A. Paulraj, "Space-time block codes: a capacity perspective," *IEEE Communications Letters*, vol. 4, no. 12, pp. 384–386, 2000.
- [4] B. Hassibi and B. M. Hochwald, "High-rate codes that are linear in space and time," *IEEE Transactions on Information Theory*, vol. 48, no. 7, pp. 1804–1824, 2002.
- [5] X. Ma and G. B. Giannakis, "Full-diversity full-rate complex-field space-time coding," *IEEE Transactions on Signal Processing*, vol. 51, no. 11, pp. 2917–2930, 2003.
- [6] B. Song, N. Kim, and H. Park, "A binary space-time code for MIMO systems," *IEEE Transactions on Wireless Communications*, vol. 11, no. 4, pp. 1350–1357, 2012.
- [7] M. Li, M. Lin, Z. Q. Gong et al., "Performance analysis of MIMO MRC system," *Electronics Letters*, vol. 43, no. 23, pp. 1297–1298, 2007.
- [8] D. G. Brennan, "Linear diversity combining techniques," *Proceedings of the IRE*, vol. 47, no. 6, pp. 1075–1102, 1959.
- [9] S. Sugiura, S. Chen, and L. Hanzo, "A universal space-time architecture for multiple-antenna aided systems," *IEEE Communications Surveys and Tutorials*, vol. 14, no. 2, pp. 401–420, 2012.
- [10] F. Molish and M. Z. Win, "MIMO systems with antenna selection," *IEEE Microwave Magazine*, vol. 5, no. 1, pp. 46–56, 2004.
- [11] S. Thoen, L. van der Perre, B. Gyselinckx, and M. Engels, "Performance analysis of combined transmit-SC/receive-MRC," *IEEE Transactions on Communications*, vol. 49, no. 1, pp. 5–8, 2001.
- [12] W. Ajib and D. Haccoun, "An overview of scheduling algorithms in MIMO-based fourth-generation wireless systems," *IEEE Network*, vol. 19, no. 5, pp. 43–48, 2005.
- [13] Q. H. Spencer, C. B. Peel, A. L. Swindlehurst, and M. Haardt, "An introduction to the multi-user MIMO downlink," *IEEE Communications Magazine*, vol. 42, no. 10, pp. 60–67, 2004.
- [14] X. Zhang, F. Chen, and W. Wang, "Outage probability study of multiuser diversity in MIMO transmit antenna selection systems," *IEEE Signal Processing Letters*, vol. 14, no. 3, pp. 161–164, 2007.
- [15] X. Zhang, Z. Lv, and W. Wang, "Performance analysis of multiuser diversity in MIMO systems with antenna selection," *IEEE Transactions on Wireless Communications*, vol. 7, no. 1, pp. 15–21, 2008.
- [16] J. M. Romero-Jerez and J. P. Pena-Martin, "ASER of rectangular MQAM in noise-limited and interference-limited MIMO MRC systems," *IEEE Wireless Communications Letters*, vol. 1, no. 1, pp. 1–5, 2012.
- [17] M. K. Simon and M. S. Alouini, *Digital Communication in Fading Channels*, John Wiley & Sons, New York, NY, USA, 2nd edition, 2005.
- [18] B. Holter and G. E. Øien, "On the amount of fading in MIMO diversity systems," *IEEE Transactions on Wireless Communications*, vol. 4, no. 5, pp. 2498–2507, 2005.
- [19] C. C. Hung, C. T. Chiang, N. Y. Yen, and R. C. Wu, "Outage probability of multiuser transmit antenna selection/maximal-ratio combining systems over arbitrary Nakagami- m fading channels," *IET Communications*, vol. 4, no. 1, pp. 63–68, 2010.
- [20] C. C. Hung, C. T. Chiang, S. N. Lin, and R. C. Wu, "Outage capacity analysis of TAS/MRC systems over arbitrary Nakagami- m fading channels," *IEICE Transactions on Communications*, vol. 93, no. 1, pp. 215–218, 2010.
- [21] Z. Chen, Z. Chi, Y. Li, and B. Vucetic, "Error performance of maximal-ratio combining with transmit antenna selection in flat Nakagami- m fading channels," *IEEE Transactions on Wireless Communications*, vol. 8, no. 1, pp. 424–431, 2009.
- [22] C. J. Chen and L. C. Wang, "A unified capacity analysis for wireless systems with joint multiuser scheduling and antenna diversity in Nakagami fading channels," *IEEE Transactions on Communications*, vol. 54, no. 3, pp. 469–478, 2006.
- [23] S. Gradshteyn and I. M. Ryzhik, *Table of Integrals, Series, and Products*, Academic Press, New York, NY, USA, 1995.
- [24] J. M. Romero-Jerez and A. J. Goldsmith, "Performance of multichannel reception with transmit antenna selection in arbitrarily distributed Nakagami fading channels," *IEEE*

Transactions on Wireless Communications, vol. 8, no. 4, pp. 2006–2013, 2009.

- [25] J. C. S. S. Filho, M. D. Yacoub, and G. A. Fraidenraich, “A simple accurate method for generating autocorrelated Nakagami- m envelope sequences,” *IEEE Communications Letters*, vol. 11, no. 3, pp. 231–233, 2007.

Research Article

Investigation of the Effect of Noise Correlations on Diversity Gains and Capacities of Multiport Antennas Using Reverberation Chamber

Xiaoming Chen and Jian Yang

Department of Signals and Systems, Chalmers University of Technology, 41296 Gothenburg, Sweden

Correspondence should be addressed to Xiaoming Chen, xiaoming.chen@chalmers.se

Received 4 July 2012; Revised 27 October 2012; Accepted 5 November 2012

Academic Editor: Min Zhang

Copyright © 2012 X. Chen and J. Yang. This is an open access article distributed under the Creative Commons Attribution License, which permits unrestricted use, distribution, and reproduction in any medium, provided the original work is properly cited.

Most of previous studies on diversity gains and capacities of multiantenna systems assumed independent and identically distributed (i.i.d.) Gaussian noises. There are a few studies about the noise correlation effects on diversity gains or MIMO capacities, however, by simulations only. In this paper, the maximum ratio combining (MRC) diversity gain and multiple-input multiple-output (MIMO) capacity including correlated noises are presented. Based on the derived formulas, measurements in a reverberation chamber are performed for the first time to observe the effect of noise correlations on diversity gains and MIMO capacities.

1. Introduction

Diversity techniques are used to mitigate fading effects in wireless multipath environments to offer better communication reliability; the multiple-input multiple-output (MIMO) multiplexing, on the other hand, makes use of the scattering property to provide higher communication data rates. Since both the (spatial) diversity and multiplexing in mobile communications involve multiport antennas, the diversity gain and ergodic MIMO capacity become two common parameters for characterization of multiport antennas. This paper focuses on the maximum ratio combining (MRC) diversity gain and the ergodic MIMO capacity. We assume perfect channel state information (CSI) at receive side but no CSI at transmit side throughout this paper.

MRC diversity gains and MIMO capacities of multiport antennas have been measured in real-life (outdoor and indoor) multipath environments [1–4]. These studies provide valuable empirical results for various representative environments. However, real-life measurements are usually time-consuming and costly. The diversity gain of a multiport antenna can also be evaluated based on anechoic chamber measurements [5]. However, the full radiation pattern measurement is also time-consuming. As an alternative, the

reverberation chamber is getting more and more popularity for MIMO terminal characterization (and even system tests) due to its fast and repeatable measurements [6–14]. A reverberation chamber is basically a large metal cavity with mode-stirrers inside to create a Rayleigh-fading environment [15].

While most of the previous works assumed independent, identically distributed (i.i.d.) noises, it was pointed out in [16, 17] that the antenna mutual coupling, apart from affecting spatial correlations of received signals, causes noise correlations which, in turn, affect diversity gains and MIMO capacities. However, these studies were carried out by simulations only, and there is so far no measurement for noise correlation effects on either diversity gains or MIMO capacities.

The main purpose of this paper is to study and observe the effects of correlated noises on diversity gains and MIMO capacities by measurements in a reverberation chamber. Formulations of the diversity gain and MIMO capacity including noise correlations (using the noise prewhitening concept) are given in Section 2. The measurements and results are discussed in Section 3, where great care is exerted in choosing appropriate frequency step and frequency stirring bandwidth in order to have accurate measurement results. This paper

is particularly useful for over-the-air (OTA) measurements using reverberation chambers.

2. Theory

Unlike that in [16] where an open-circuit channel concept was used, in the paper, we deal with composite channels including overall antenna effects (i.e., spatial correlation, mutual coupling, and antenna efficiencies) directly, which are more convenient for measured channels [1–14]. Provided that mutual coupling effects can be included correctly using antenna impedance matrices and with the right channel normalization, the open-circuit channel approach gives the same result as the composite channel (including overall antenna effect) approach [4]. In the paper, the MRC diversity gain is presented using the noise prewhitening concept based on [18]. A similar approach is used in the presentation of the MIMO capacity, yet the formulation is rather simple thanks to the well-known MIMO capacity work [19].

2.1. MRC Diversity Gain. Considering a narrowband N -port diversity antenna in a Rayleigh-fading environment, the input-output relation is

$$\mathbf{y} = \mathbf{h}\mathbf{x} + \mathbf{n}, \quad (1)$$

where \mathbf{h} is the composite fading channel vector including overall antenna effect, \mathbf{x} is the complex baseband scalar input signal, \mathbf{y} is the complex baseband output signal, and \mathbf{n} is the noise vector. Without specifications, vectors in this paper (e.g., \mathbf{h} , \mathbf{y} , \mathbf{n}) are column vectors. Note that this composite channel model is almost the same as the open-circuit one except that signals are measured with the antenna ports terminated with matched loads instead of open-circuited. In this exhibition, the mutual coupling effect is implicitly included via the composite channel \mathbf{h} . To illustrate the equivalence of the open-circuit and composite channel model, we resort to numerical simulations using both models (see Appendix A).

The covariance matrix of the diversity antenna is

$$\mathbf{R} = E[\mathbf{h}\mathbf{h}^H], \quad (2)$$

where the superscript H is the Hermitian operator, and E is the expectation operator that is usually approximated by sample mean of channel realizations. Note that in a Rayleigh-fading channel, correlation and covariance are used interchangeably, and that in rich scattering environments \mathbf{R} is nonsingular. The instantaneous MRC output power is

$$P_{\text{MRC}} = \mathbf{h}^H \mathbf{h}. \quad (3)$$

Previous literature assumed i.i.d. Gaussian noises with unity variance, that is, $\mathbf{n} \sim \mathcal{CN}(\mathbf{0}, \mathbf{I})$ where \mathbf{I} denotes identity matrix, so that P_{MRC} was equal (in value) to the instantaneous signal-to-noise ratio (SNR), denoted as γ [18]. However, for compact multiport antennas, the antenna mutual coupling colors the noises in different antenna

branches, so that $\mathbf{n} \sim \mathcal{CN}(\mathbf{0}, \mathbf{R}_n)$. Therefore, \mathbf{y} needs noise prewhitening prior to further signal processing [20]:

$$\mathbf{y}' = \mathbf{R}_n^{-1/2} \mathbf{y} = \mathbf{R}_n^{-1/2} \mathbf{h} \mathbf{x} + \mathbf{R}_n^{-1/2} \mathbf{n}, \quad (4)$$

where \mathbf{y}' is the prewhitened output signals together with spatially white (unity variance) noises to be combined by MRC. Therefore, the instantaneous SNR is

$$\gamma = (\mathbf{R}_n^{-1/2} \mathbf{h})^H (\mathbf{R}_n^{-1/2} \mathbf{h}) = \mathbf{h}^H \mathbf{R}_n^{-1} \mathbf{h} \quad (5)$$

and the covariance matrix of the prewhitened signals is

$$\mathbf{R}' = E[(\mathbf{R}_n^{-1/2} \mathbf{h})(\mathbf{R}_n^{-1/2} \mathbf{h})^H] = \mathbf{R}_n^{-1/2} \mathbf{R} (\mathbf{R}_n^{-1/2})^H. \quad (6)$$

The characteristic function of the MRC output is [21]

$$\begin{aligned} \phi(z) &= E[\exp(jz\gamma)] = \frac{1}{\det(\mathbf{I} + z\mathbf{R}')}, \\ &= \frac{1}{\det(\mathbf{I} + z\mathbf{R}_n^{-1} \mathbf{R})}. \end{aligned} \quad (7)$$

Denote λ_i ($i = 1, \dots, N$) as the i th eigenvalue of \mathbf{R}' (or equivalently $\mathbf{R}_n^{-1} \mathbf{R}$). The probability density function (PDF) of γ is inverse Fourier transform of $\phi(z)$,

$$p(\gamma) = \frac{1}{\prod_i \lambda_i} \sum_i \frac{\exp(-\gamma/\lambda_i)}{\prod_{k \neq i} ((1/\lambda_k) - (1/\lambda_i))}. \quad (8)$$

The cumulative distribution function (CDF) of γ is,

$$F(\gamma) = 1 - \sum_{i=1}^N \frac{\lambda_i^{N-1} \exp(-\gamma/\lambda_i)}{\prod_{k \neq i}^N (\lambda_i - \lambda_k)}. \quad (9)$$

For a theoretically ideal case (where a multiport antenna is power-balanced and has zero correlations and no mutual coupling among all branches), all eigenvalues are equal to each other, neither (8) nor (9) is valid anymore due to singularity. For such cases (8) and (9) must be replaced by (10) and (11), respectively [22]

$$p(\gamma) = \frac{1}{(N-1)!} \frac{\gamma^{N-1}}{\lambda} \exp\left(-\frac{\gamma}{\lambda}\right), \quad (10)$$

$$F(\gamma) = 1 - \exp\left(-\frac{\gamma}{\lambda}\right) \sum_{i=1}^N \frac{(\gamma/\lambda)^{i-1}}{(i-1)!}. \quad (11)$$

Note that the CDF formula (9) is almost identical to the one given in [18] except that λ_i are eigenvalues of $\mathbf{R}_n^{-1} \mathbf{R}$ instead of \mathbf{R} . This CDF formula is also only valid for multiport antennas with distinct eigenvalues because of its singularity (when any two eigenvalues are equal). Thus one tends to believe that (9) will result in large numerical error when two eigenvalues are close to each other. However, it has been shown in [7] that (9) does not have large numerical error when the estimated eigenvalues from measurements are close to each other, and therefore holds for practical measurements. Equation (9) will be used in this paper hereafter.

The effective diversity gain is defined as the output SNR improvement of a diversity antenna compared with that of an ideal single antenna at 1% outage probability level [22],

$$G_{\text{eff}} = \frac{F^{-1}(\gamma)}{F_{\text{ref}}^{-1}(\gamma)} \Big|_{1\%}, \quad (12)$$

where $(\cdot)^{-1}$ denotes functional inversion, F_{ref} is the CDF of a single ideal antenna,

$$F_{\text{ref}}(\gamma) = 1 - \exp(-\gamma). \quad (13)$$

2.2. MIMO Capacity. Considering a narrowband MIMO system with N_t transmit antennas and N_r receive antennas in a flat Rayleigh-fading environment, the input-output relation can be modeled as

$$\mathbf{y} = \mathbf{Hx} + \mathbf{n}, \quad (14)$$

where \mathbf{H} is complex fading channel matrix including overall antenna effects, and \mathbf{x} is complex baseband transmit signal vector. Similarly, due to mutually coupled noise, the noise prewhitening needs to be performed to \mathbf{y} ,

$$\mathbf{y}' = \mathbf{R}_n^{-1/2} \mathbf{y} = \mathbf{R}_n^{-1/2} \mathbf{Hx} + \mathbf{R}_n^{-1/2} \mathbf{n}, \quad (15)$$

so that the classical MIMO capacity formula given by [19] holds.

Since there is no CSI at transmit side, the transmit power is assumed to be equally allocated to the N_t transmit antennas, the ergodic capacity in this case is [19]

$$\begin{aligned} C &= E \left\{ \log_2 \left[\det \left(\mathbf{I} + \frac{\gamma}{N_t} (\mathbf{R}_n^{-1/2} \mathbf{H}) (\mathbf{R}_n^{-1/2} \mathbf{H})^H \right) \right] \right\} \\ &= E \left\{ \log_2 \left[\det \left(\mathbf{I} + \frac{\gamma}{N_t} \mathbf{R}_n^{-1} \mathbf{H} \mathbf{H}^H \right) \right] \right\}. \end{aligned} \quad (16)$$

2.3. Mutual Coupling on Noises. The mutual coupling effect on noises was studied in [16] for a MIMO system, which is also applicable for diversity antennas. For the sake of completeness, we briefly include the derivation here. Assuming that each antenna port is terminated separately, the spectral density of total thermal noise matrix is

$$\mathbf{P}_n(f) = \frac{1}{2} (\mathbf{Y}_L + \mathbf{Y}_L^*) \mathbf{v}_n \mathbf{v}_n^H, \quad (17)$$

where \mathbf{Y}_L is the diagonal admittance matrix of the loads and \mathbf{v}_n is thermal noise voltage. Based on simple circuit theory, we have

$$\begin{aligned} \mathbf{v}_n \mathbf{v}_n^H &= 2kT \mathbf{Y}_A^{-1} (\mathbf{Y}_A + \mathbf{Y}_A^*) (\mathbf{Y}_A^{-1})^H, \\ \mathbf{Y}_A &= \mathbf{Y}_R + \mathbf{Y}_L, \end{aligned} \quad (18)$$

where k is Boltzmann's constant, T is the absolute temperature, and \mathbf{Y}_R is the admittance matrix of the receive antennas. For a narrowband system, the normalized noise covariance matrix is

$$\mathbf{R}_n = \frac{\mathbf{P}_n(f)}{P_n(f)}, \quad (19)$$

where $P_n(f)$ is the noise spectral density of an isolated antenna. Note that the exact values of k , T and actual system bandwidth do not matter for \mathbf{R}_n since they are all cancelled out by the normalization (19). In order to illustrate the mutual coupling effect on noise correlation, we resort to numerical simulations presented in Appendix B, where it is shown that the mutual coupling effect on noise correlation is more profound with small antenna separation.

3. Measurements and Results

To study noise coupling effects on diversity gains and MIMO capacities, we performed measurements of the so-called Eleven antenna (a wideband log-periodic array working from 2 to 13 GHz as shown in Figure 1) [23], in a reverberation chamber. In this case, the wideband array has to be regarded as many narrowband antennas working at different frequencies. Therefore, the wideband measurement is regarded as many separate narrowband measurements for many virtual narrowband antennas operating at different frequencies.

3.1. Measurement of Channel Samples. The chamber used in this work is the Bluetest HP reverberation chamber with a size of $1.75 \times 1.25 \times 1.8 \text{ m}^3$. It has two plate stirrers, a turn-table platform, and three wall antennas (antennas mounted on three orthogonal walls inside the chamber) (see Figure 2). In the measurements, the platform moved step-wisely to 20 positions (equally spaced over one complete platform rotation) and for each platform position the two plates moved step-wisely and simultaneously to 10 positions (equally spaced over the total distances that they could travel). At each stirrer position and for each of the three wall antennas, the vector network analyzer (VNA) performed a frequency sweeping to sample the channel transfer functions over frequency. The VNA used in this work is Agilent E5071C ENA series network analyzer working from 100 kHz to 8.5 GHz. We therefore chose a measuring frequency range of 2–8 GHz. The frequency step was set to 1 MHz (for a reason that will become clear later). Since the maximum sweep point of this VNA is 1601, we have to divide the whole frequency band into four subbands, that is, 2–3.5 GHz, 3.5–5 GHz, 5–6.5 GHz, and 6.5–8 GHz.

For diversity measurements, the Eleven antenna is regarded as the diversity antenna under test, and channels corresponding to the three wall antennas are considered as the same random process. Therefore, there are 600 channel samples per frequency point for the diversity evaluation. For capacity measurements, the Eleven antenna is regarded as receive MIMO antenna under test, and the three wall antennas are regarded as three transmit antennas. Therefore, there are 200 MIMO channel samples per frequency point for the capacity evaluation. In both cases, the measured channel samples may not be sufficient to support accurate estimations. A simple way to increase channel samples is to treat channel samples at different frequencies as different channel realizations. This methodology has been used in [2] for real-life multipath measurements. In a reverberation chamber, it is usually referred to as the frequency

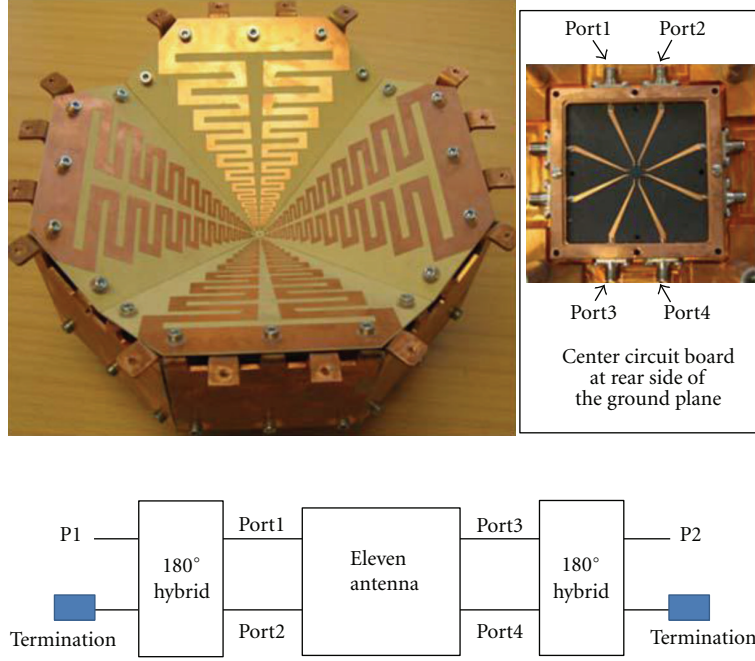


FIGURE 1: Photos of front and back sides of Eleven antenna (upper) and diagram of Eleven antenna with the four ports of one polarization combined to two ports that as used as measurement ports in this paper (lower).

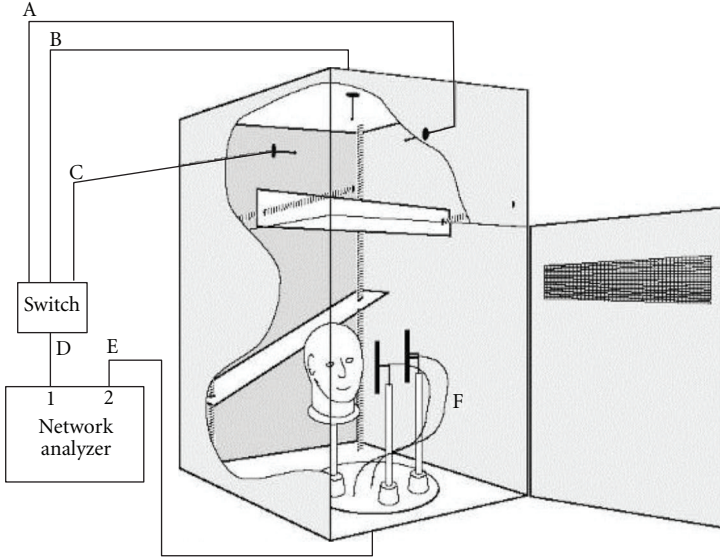


FIGURE 2: Drawing of Bluetest reverberation chamber measuring a two-port antenna.

stirring or electronic stirring [24]. However, the frequency stirring bandwidth has to be carefully chosen so that more equivalently independent samples can be included without changing the channel statistics. The coherence bandwidth of the channel is around 1-2 MHz [25], while the stationarity bandwidth is larger than 20 MHz (see [8] and the references therein). In practice, the antenna bandwidth also affects the channel characteristics, since the composite channel includes the antennas. Hence, the frequency stirring bandwidth should be larger than coherence bandwidth but smaller

than stationarity bandwidth and antenna bandwidth. The Eleven antenna has reflection coefficients below -10 dB over its working frequency range [23]. As a result, an empirical frequency stirring bandwidth of 20 MHz is chosen. At this point, the choice of 1-MHz frequency step starts to make sense in that a larger frequency step will degrade the frequency resolution and a smaller one will result in spectrally correlated channel samples (which in turn makes the frequency stirring less effective). As a result, there are 12000 channel samples per frequency for diversity

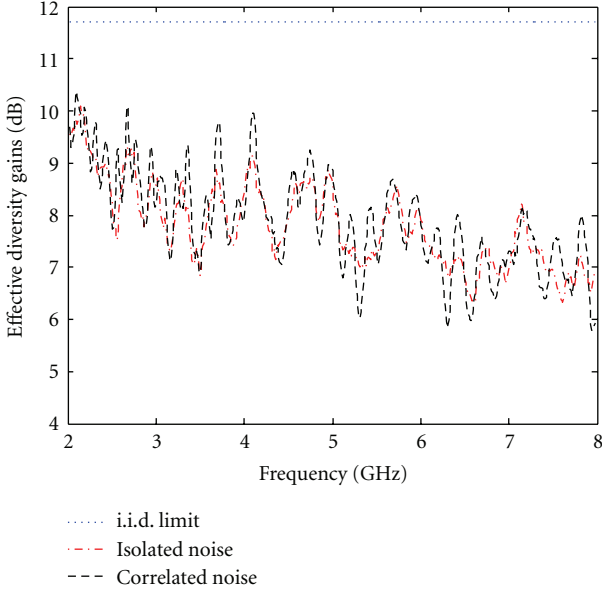


FIGURE 3: Measured effective diversity gains of the two-port Eleven antenna with/without coupled noise.

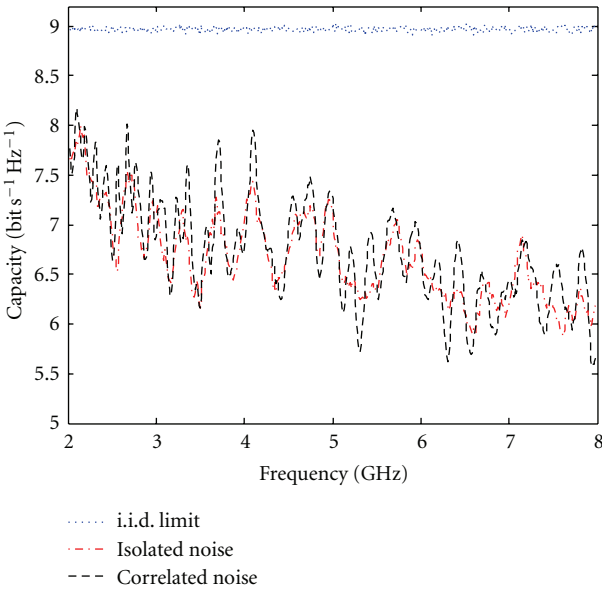


FIGURE 4: Measured ergodic capacities of the two-port Eleven antenna at 15 dB SNR with/without coupled noise.

evaluations and 4000 channel samples per frequency for capacity evaluations.

In order to calibrate out the long-term fading (or attenuation) in the chamber (so that only short-term fading comes into play), a reference measurement is needed, where the average power transfer function is measured using a reference antenna with known total radiation efficiency. The reference power level, P_{ref} , is obtained by dividing the average power function by the total radiation efficiency of the reference antenna. The measured channel vector \mathbf{h}_{meas} (for diversity evaluations) and channel matrix \mathbf{H}_{meas} (for

capacity evaluations) are functions of frequency (or virtual narrowband antenna) and stirrer position. For convenience, the normalized measured channel vector and matrix are denoted, respectively, as

$$\mathbf{h} = \frac{\mathbf{h}_{\text{meas}}}{\sqrt{P_{\text{ref}}}}, \quad \mathbf{H} = \frac{\mathbf{H}_{\text{meas}}}{\sqrt{P_{\text{ref}}}}. \quad (20)$$

Due to the strong scattering inside the chamber, line-of-sight (LOS) components usually have much smaller power level as scattered components. Therefore, \mathbf{h} and \mathbf{H} in (20) can be considered as zero mean vector and matrix, respectively. Note that the total radiation efficiencies of the wall antennas are also calibrated out by (20). Since the wall antennas are separated sufficiently far from each other (at least 7~8 wavelength spacing at the lowest frequency) and orthogonally polarized, their correlations are negligible [26]. Therefore, the Eleven antenna's effects on diversity gains and MIMO capacities without the effects of the transmit antennas can be examined by the measurement setup and normalization (20) (cf. semicorrelation configurations in [27]).

3.2. Measurement of Correlated Noises. In order to calculate the correlated noises, we have to know the admittance (or impedance) matrix of the Eleven antenna. Note that the derivation in Section 2.3 holds for lossless multiport antennas only. Fortunately, the Eleven antenna itself has a negligible ohmic loss (below 0.3 dB over the working frequency range) [23]. The 180° hybrids (see Figure 1), however, have insertion losses between 1.4 dB at 2 GHz and 3 dB at 8 GHz. In order to calibrate the hybrid losses, we measured S-parameters of the Eleven antenna at the four ports, port1–port4 (see Figure 1) (without the 180° hybrids) in an anechoic chamber. These measured S-parameters were combined using two ideal lossless 180° hybrids to obtain S-parameters at “lossless” ports P1' and P2'. These “lossless” S-parameters are converted to Y-parameters by

$$\mathbf{Z}_R = Z_0(\mathbf{I} + \mathbf{S}_R)(\mathbf{I} - \mathbf{S}_R)^{-1}, \quad \mathbf{Y}_R = \mathbf{Z}_R^{-1}, \quad (21)$$

where \mathbf{S}_R is S-parameter matrix, \mathbf{Z}_R (\mathbf{Y}_R) is the impedance (admittance) matrix of the Eleven antenna, and $Z_0 = 50 \text{ ohm}$. Assuming 50-ohm impedance termination at antenna ports, $\mathbf{Y}_L = \mathbf{I}/Z_0$. Substitute these into (17)–(19), the noise covariance matrix \mathbf{R}_n can be calculated.

3.3. Measurement Results. With known \mathbf{R}_n and measured channel samples, MRC diversity gains and MIMO ergodic capacities can be readily calculated using the formulas derived in Section 2. Figure 3 shows the measured effective diversity gains with/without noise coupling (i.e., isolated/correlated noise). It is seen that the correlated noises alter the effective diversity gains at some frequencies (corresponding to some virtual narrowband antennas) compared with that of the isolated noise case. Figure 4 shows the measured ergodic capacity with/without noise coupling (i.e., isolated/correlated noise). Similarly, it is found that the correlated noises affect ergodic capacities for some virtual

narrowband antennas at different frequencies. The ideal diversity gains and ergodic capacities with i.i.d. channel are also plotted, respectively, in Figures 3 and 4 (marked as i.i.d. limits) for comparisons. Note that the i.i.d. limit for ergodic capacities were estimated by the sample mean of mutual information realizations corresponding to 4000 numerically generated i.i.d. Rayleigh-fading channel realizations, while the exact i.i.d. limit for effective diversity gains was calculated analytically using (11)–(13).

There are many factors affecting diversity gain and capacity; however, the “isolated noise” curves in Figures 3 and 4 represent, respectively, the diversity gain and capacity taking into account all the factors except the noise correlation, while the corresponding “correlated noise” curves represent the diversity gain or capacity with all factors including the noise correlation. Therefore, the difference between these two curves is only due to the effect of noise correlation. To clearly illustrate the noise correlation effect on either diversity gain or capacity, we plot the diversity gain and capacity differences (or errors) between “correlated noise” and “isolated noise” cases (in percentage by dividing the differences with the corresponding “correlated noise” value) in Figure 5.

The correlation magnitudes, ρ , of the two-port Eleven antenna can be estimated by

$$\hat{\rho} = \left| \left[\hat{\mathbf{R}} \right]_{12} \right|, \quad \hat{\mathbf{R}} = \frac{1}{MN_t} \sum_{m=1}^M \mathbf{H}_m \mathbf{H}_m^H, \quad (22)$$

where \mathbf{H}_m denotes the m th sample of normalized channel \mathbf{H} , $M = 4000$ is the number of samples, and $N_t = 3$ is the number of wall antennas. Figure 6 shows the correlation magnitudes of the virtual narrowband antennas working at different frequencies. Comparing Figure 5 with Figure 6, it is found that diversity gains (and ergodic capacities) with isolated noises are very close to those with correlated noises at frequencies where correlation magnitudes are smaller than 0.2; otherwise, there are noticeable deviations between them and these deviations tend to increase with increasing correlations. In other words, for virtual narrowband multiport antennas with small correlations, it is a good approximation by assuming i.i.d. Gaussian noise, otherwise noise correlations need to be considered in order to get accurate diversity gains and/or ergodic capacities. This observation agrees with the noise power simulation in Appendix B, where it is shown that noise correlation can be neglected when the mutual coupling (or correlation) between the antenna ports is negligible.

This finding verifies the simulation results in [16], where it was shown that the noise correlation has noticeable effect on capacity when parallel half-wavelength dipoles are closer than 0.3 wavelengths, while the parallel half-wavelength dipoles’ correlation magnitude is larger than 0.2 when dipole separation is smaller than 0.3 wavelengths in a three-dimensional isotropic-scattering environment [28], for example, a reverberation chamber [29].

4. Conclusion

Most of previous diversity and MIMO studies assumed i.i.d. noises in antenna branches. There are only a few works studying the effects of noise correlations on diversity gains and MIMO capacity [16, 17], but these studies were carried out by simulations only. In this paper, the noise correlation effects on diversity gains and capacities are formulated using the noise prewhitening concept and the computational robustness of the derived MRC CDF was proved rigorously. The effects of correlated noises on MRC diversity gains and MIMO ergodic capacities were studied via reverberation chamber measurements, where a great care is exerted in choosing the measurement frequency step and frequency stirring bandwidth in order to have accurate measurement results. It was shown that, only for multiport antennas with very small correlations, the noise correlation effects on diversity gains (capacities) can be neglected. Otherwise, it should be taken into account for accurate diversity (capacity) measurements.

Appendices

A. Open-Circuit and Composite Channel Model

From the circuit theory, a MIMO system can be expressed using the open-circuit channel model as [17]

$$\begin{bmatrix} \mathbf{v}_T \\ \mathbf{v}_R \end{bmatrix} = \begin{bmatrix} \mathbf{Z}_T & \mathbf{0} \\ \mathbf{H}^{oc} & \mathbf{Z}_R \end{bmatrix} \begin{bmatrix} \mathbf{i}_T \\ \mathbf{i}_R \end{bmatrix}, \quad (A.1)$$

where \mathbf{Z}_T , \mathbf{i}_T , and \mathbf{v}_T are impedance matrix, current and voltage vectors at the transmitter, respectively; and \mathbf{Z}_R , \mathbf{i}_R , and \mathbf{v}_R are impedance matrix, current and voltage vectors at the receiver, respectively; $\mathbf{0}$ is zero matrix with proper dimensions, \mathbf{H}^{oc} is channel matrix corresponding to open-circuited antennas at both MIMO sides. Note that for notation simplicity and without loss of generality, the additive noises are omitted for the time being, while the noises can be easily included using similar SNR concept as the one used in Section 2.2.1. Based on simple circuit theory, the transmit and receive voltage vectors can be expressed, respectively, as

$$\mathbf{v}_T = \mathbf{Z}_T (\mathbf{Z}_T + \mathbf{Z}_s)^{-1} \mathbf{v}_s, \quad \mathbf{v}_R = -\mathbf{Z}_L \mathbf{i}_R, \quad (A.2)$$

where \mathbf{v}_s is source voltage vector, \mathbf{Z}_s and \mathbf{Z}_L are source and load impedance matrices, respectively. For coupled impedance matching, both \mathbf{Z}_s and \mathbf{Z}_L are full matrices, whereas for uncoupled impedance matching, \mathbf{Z}_s and \mathbf{Z}_L are diagonal matrices. \mathbf{v}_R is related to \mathbf{v}_T as

$$\mathbf{v}_R = \mathbf{Z}_L (\mathbf{Z}_L + \mathbf{Z}_R)^{-1} \mathbf{H}^{oc} (\mathbf{Z}_T + \mathbf{Z}_s)^{-1} \mathbf{v}_s. \quad (A.3)$$

The factor $\mathbf{Z}_L (\mathbf{Z}_L + \mathbf{Z}_R)^{-1} \mathbf{H}^{oc} (\mathbf{Z}_T + \mathbf{Z}_s)^{-1}$ is voltage transfer function. To relate the Z-parameter model (A.3) to the information-theoretic input-output relation, $\mathbf{y} = \mathbf{H}_{eff} \mathbf{x}$, the

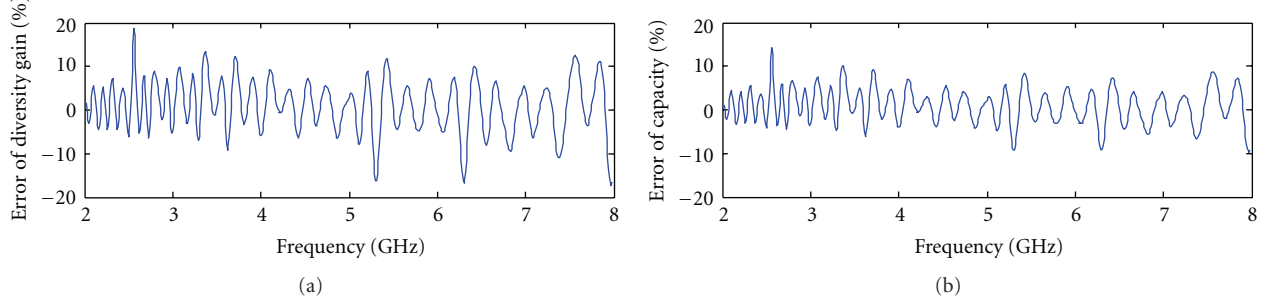


FIGURE 5: Errors of effective diversity gain and ergodic capacities (at 15-dB SNR) of the two-port Eleven antenna due to noise correlation.

voltage transfer function has to be properly normalized such that the received power satisfies

$$\begin{aligned} E\left\{\text{tr}\left[\text{Re}\left(\mathbf{Z}_L \mathbf{i}_R \mathbf{i}_R^H\right)\right]\right\} &= E\left[\text{tr}\left(\mathbf{y} \mathbf{y}^H\right)\right] \\ &= E\left[\text{tr}\left(\mathbf{H}_{\text{eff}} \mathbf{K}_x \mathbf{H}_{\text{eff}}^H\right)\right], \end{aligned} \quad (\text{A.4})$$

where $\mathbf{K}_x = \mathbf{I}_{N_t} P_T / N_t$ is covariance matrix of transmit signals. The total radiated power is $P_T = E\{\text{tr}[\text{Re}(\mathbf{Z}_T \mathbf{i}_T \mathbf{i}_T^H)]\}$. The effective channel can be written as

$$\mathbf{H}_{\text{eff}} = \sqrt{N_t} \text{Re}(\mathbf{Z})_L^{1/2} (\mathbf{Z}_L + \mathbf{Z}_R)^{-1} \mathbf{H}^{\text{oc}} \text{Re}(\mathbf{Z})_T^{-1/2}. \quad (\text{A.5})$$

Accordingly, the effective channel should be normalized to the average channel gain of a SISO system with antennas at both sides conjugate matched, that is, $z_L = z_R^*$ and $z_s = z_T^*$ where superscript * is conjugate operator, z_T and z_R are antenna transmit and receive impedance, respectively, and z_L and z_s are load and source impedances at transmit and

receive sides, respectively. It is easy to derive the effective SISO channel, that is, h_{eff} , as

$$h_{\text{eff}} = \sqrt{\frac{N_t}{r_R r_T}} \frac{h}{2}, \quad (\text{A.6})$$

where $r_T = \text{Re}\{z_T\}$, $r_R = \text{Re}\{z_R\}$, and $E[|h|^2] = 1$. Dividing \mathbf{H}_{eff} with $\sqrt{E[|h_{\text{eff}}|^2]}$, the normalized MIMO channel that includes overall antenna effect is

$$\mathbf{H} = 2\sqrt{r_R r_T} \text{real}(\mathbf{Z})_L^{1/2} (\mathbf{Z}_L + \mathbf{Z}_R)^{-1} \mathbf{H}^{\text{oc}} \text{real}(\mathbf{Z})_T^{-1/2}, \quad (\text{A.7})$$

where $\mathbf{H}^{\text{oc}} = \Phi_R^{\text{oc},1/2} \mathbf{H}_w \Phi_T^{\text{oc},1/2}$, with Φ_R^{oc} and Φ_T^{oc} denoting the open-circuit correlation matrix. In order to compare the open-circuit channel model (A.7) with composite channel model, we have to construct the correlation matrix of the signals at the loaded antenna ports (that takes the overall antenna effect, including mutual coupling, into account)

$$\begin{aligned} \mathbf{R} &= \mathbf{\Xi} \circ \mathbf{\Phi}, \quad \mathbf{\Xi} = \sqrt{\mathbf{e}} \sqrt{\mathbf{e}}^T, \\ [\Phi]_{mn} &= \frac{\iint_{4\pi} \mathbf{g}_m^H(\Omega) \mathbf{P}_{\text{inc}}(\Omega) \mathbf{g}_n(\Omega) d\Omega}{\sqrt{\iint_{4\pi} \mathbf{g}_m^H(\Omega) \mathbf{P}_{\text{inc}}(\Omega) \mathbf{g}_m(\Omega) d\Omega \cdot \iint_{4\pi} \mathbf{g}_n^H(\Omega) \mathbf{P}_{\text{inc}}(\Omega) \mathbf{g}_n(\Omega) d\Omega}}, \end{aligned} \quad (\text{A.8})$$

where \mathbf{g}_i ($i = 1, \dots, N$) is the embedded far-field function vector (with elements representing components for different polarizations) at the i th loaded antenna port, and \mathbf{P}_{inc} is dyadic power angular spectrum of the incident waves, $\mathbf{e} = [e_{\text{emb}1} \ e_{\text{emb}2} \ \dots \ e_{\text{emb}N}]^T$, \circ denotes entry-wise product, the superscript T denotes the transpose operator, and $\sqrt{\cdot}$ is entry-wise square root. Note that in a polarization-balanced isotropic reverberation chamber, $\mathbf{P}_{\text{inc}}(\Omega) = \mathbf{I}$. Also note that the transmitting or receiving dependence has been dropped in the expression for notional convenience. The composite channel (including the overall antenna effect) can be expressed as

$$\mathbf{H} = \mathbf{R}_R^{1/2} \mathbf{H}_w \mathbf{R}_T^{1/2}. \quad (\text{A.9})$$

For simplicity, we use two parallel half-wavelength dipoles as an example. The dipole antennas are used as receive

antennas, and two ideal antennas are used at the transmit side. The open-circuit and embedded radiation patterns can be expressed, respectively, as

$$\begin{aligned} \vec{G}_i(\theta, \phi) &= -\hat{\theta} \frac{2C_k \eta \cos(\pi/2 \cos \theta)}{k \sin \theta} \exp\left(jk \frac{d_i}{2} \sin \theta \sin \phi\right), \\ \vec{G}_{\text{emb},1}(\theta, \phi) &= \vec{G}_1(\theta, \phi) I_1 + \vec{G}_2(\theta, \phi) I_2, \\ \vec{G}_{\text{emb},2}(\theta, \phi) &= \vec{G}_1(\theta, \phi) I_2 + \vec{G}_2(\theta, \phi) I_1, \end{aligned} \quad (\text{A.10})$$

where $i = 1, 2$, $d_1 = -d$, $d_2 = d$, $C_k = -jk/4\pi$, and η is the free-space wave impedance. From simple circuit theory, when the excitation current at the port 1 is unity, that is, $I_1 = 1$,

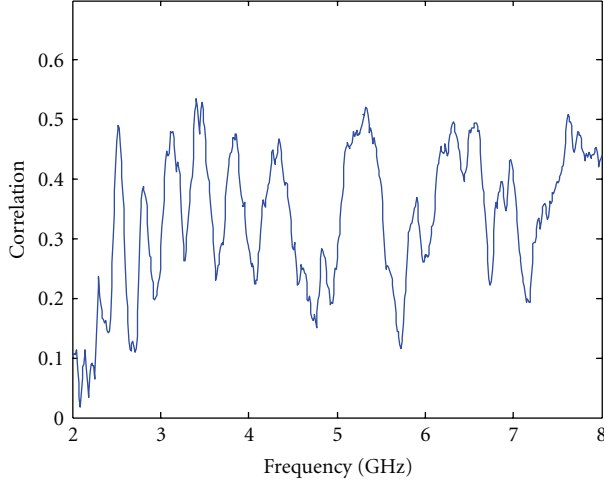


FIGURE 6: Measured magnitudes of complex correlations of the Eleven antenna.

$I_2 = -Z_{12}/(Z_{11} + Z_S)$. The embedded radiation efficiencies can therefore be calculated as

$$e_{\text{emb},j} = \left(1 - \left| \frac{z_{\text{in},j} - z_{L,jj}^*}{z_{\text{in},j} + z_{L,jj}} \right|^2\right) \left(1 - \frac{r_{L,jj} \sum_{i=1, i \neq j} |I_i|^2}{\text{Re}\{z_{\text{in},j}\} |I_j|^2}\right),$$

$$z_{\text{in},j} = z_j + \frac{1}{I_j} \sum_{i=1, i \neq j} z_{ji} I_i. \quad (\text{A.11})$$

The analytical expressions for the self- and mutual-impedances of the parallel dipoles can be found in [30]. Figure 7 shows the ergodic capacities (as functions of dipole separation) in an isotropic scattering environment at 13-dB SNR with 50-ohm loads using both open-circuit and composite channel model. As expected, both models result in the same capacity values.

B. Mutual Coupling Effect on Noise Correlation

In order to illustrate the mutual coupling effect on noise correlations, we resort to simulations again using the example of two parallel half-wavelength dipoles. As explained in Appendix A, the impedance matrix of the parallel dipoles is given in [30]. Substitute the impedance (or equivalently admittance) matrix into (17)–(19), the noise correlation matrix \mathbf{R}_n can be calculated. Since the two dipole antennas are identical, the noise power is simply $[\mathbf{R}_n]_{11}$. Figure 8 calculates the noise power as a function of dipole separation with/without the mutual coupling effect (i.e., correlated noise and isolated noise), where isolated noise is obtained simply by assuming a pair of uncoupled parallel dipoles (with a diagonal impedance matrix). It can be seen from Figure 8 that due to mutual coupling affect the noise power is not white anymore and that it approaches the white noise (i.i.d. noise) asymptotically as dipole separation increases (i.e., as the mutual coupling effect becomes negligible). This observation implies that the noises at different antenna

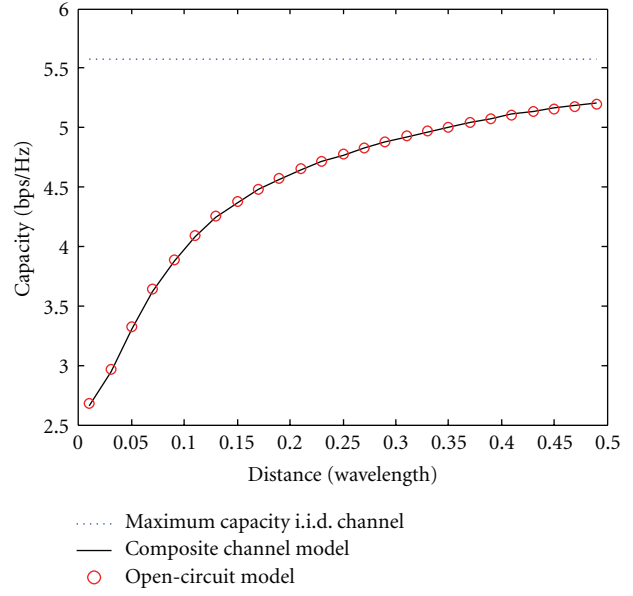


FIGURE 7: Ergodic capacities at 13-dB SNR in an isotropic scattering environment using open-circuit and composite channel models.

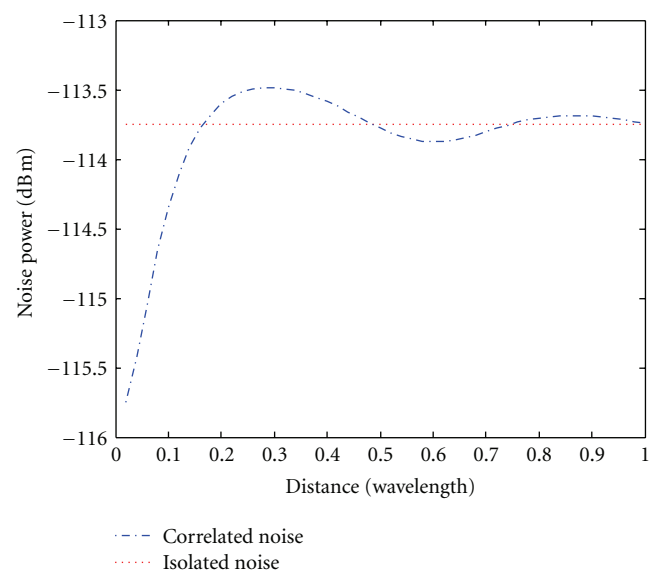


FIGURE 8: Comparison of noise powers of isolated noise and correlated noise.

ports can be approximately treated as uncorrelated when the separation is small.

References

- [1] O. Nørklit, P. D. Teal, and R. G. Vaughan, “Measurement and evaluation of multi-antenna handsets in indoor mobile communication,” *IEEE Transactions on Antennas and Propagation*, vol. 49, no. 3, pp. 429–437, 2001.
- [2] K. Yu, M. Bengtsson, B. Ottersten, D. McNamara, P. Karlsson, and M. Beach, “Modeling of wide-band MIMO radio channels

- based on NLoS indoor measurements," *IEEE Transactions on Vehicular Technology*, vol. 53, no. 3, pp. 655–665, 2004.
- [3] A. Diallo, C. Luxey, P. Le Thuc, R. Staraj, and G. Kossiavas, "Diversity performance of multiantenna systems for UMTS cellular phones in different propagation environments," *International Journal of Antennas and Propagation*, vol. 2008, Article ID 836050, 10 pages, 2008.
 - [4] Y. Fei, Y. Fan, B. K. Lau, and J. S. Thompson, "Optimal single-port matching impedance for capacity maximization in compact MIMO arrays," *IEEE Transactions on Antennas and Propagation*, vol. 56, no. 11, pp. 3566–3575, 2008.
 - [5] V. Plicanic, B. K. Lau, A. Derneryd, and Z. Ying, "Actual diversity performance of a multiband diversity antenna with hand and head effects," *IEEE Transactions on Antennas and Propagation*, vol. 57, no. 5, pp. 1547–1556, 2009.
 - [6] K. Rosengren and P.-S. Kildal, "Radiation efficiency, correlation, diversity gain and capacity of a six-monopole antenna array for a MIMO system: theory, simulation and measurement in reverberation chamber," *IEE Proceedings*, vol. 152, no. 1, pp. 7–16, 2005.
 - [7] X. Chen, P.-S. Kildal, J. Carlsson, and J. Yang, "MRC diversity and MIMO capacity evaluations of multi-port antennas using reverberation chamber and anechoic chamber," *IEEE Transactions on Antennas and Propagation*. In press.
 - [8] X. Chen, "Spatial correlation and ergodic capacity of MIMO channel in reverberation chamber," *International Journal of Antennas and Propagation*, vol. 2012, Article ID 939104, 7 pages, 2012.
 - [9] X. Chen, P.-S. Kildal, and J. Carlsson, "Fast converging measurement of MRC diversity gain in reverberation chamber using covariance-eigenvalue approach," *IEICE Transactions on Electronics*, vol. 94, no. 10, pp. 1657–1660, 2011.
 - [10] L. Garcia-Garcia, B. Lindmark, N. Jaldén, and C. Orlenius, "MIMO capacity of antenna arrays evaluated using radio channel measurements, reverberation chamber and radiation patterns," *IET Microwaves, Antennas and Propagation*, vol. 1, no. 6, pp. 1160–1169, 2007.
 - [11] J. F. Valenzuela-Valdés, M. A. Garcia-Fernandez, A. M. Martinez-Gonzalez, and D. A. Sanchez-Hernandez, "The influence of efficiency on receive diversity and MIMO capacity for Rayleigh-fading channels," *IEEE Transactions on Antennas and Propagation*, vol. 56, no. 5, pp. 1444–1450, 2008.
 - [12] K. A. Remley, H. Fielitz, C. L. Holloway, Q. Zhang, Q. Wu, and D. W. Matolak, "Simulation of a MIMO system in a reverberation chamber," in *Proceedings of the IEEE EMC Symposium*, August 2011.
 - [13] M. Lienard and P. Degauque, "Simulation of dual array multipath channels using mode-stirred reverberation chambers," *Electronics Letters*, vol. 40, no. 10, article 578, 2004.
 - [14] O. Delangre, P. De Doncker, M. Lienard, and P. Degauque, "Coupled reverberation chambers for emulating MIMO channels," *Comptes Rendus Physique*, vol. 11, no. 1, pp. 30–36, 2010.
 - [15] J. G. Kostas and B. Boverie, "Statistical model for a mode-stirred chamber," *IEEE Transactions on Electromagnetic Compatibility*, vol. 33, no. 4, pp. 366–370, 1991.
 - [16] S. M. Krusevac, R. A. Kennedy, and P. B. Rapajic, "Effect of signal and noise mutual coupling on MIMO channel capacity," *Wireless Personal Communications*, vol. 40, no. 3, pp. 317–328, 2007.
 - [17] M. T. Ivrlač and J. A. Nossek, "Physical modeling of communication systems in information theory," in *Proceedings of the IEEE International Symposium on Information Theory (ISIT '09)*, pp. 2179–2183, Seoul, Korea, 2009.
 - [18] W. C. Y. Lee, "Mutual coupling effect on maximum-ratio diversity combiners and application to mobile ratio," *IEEE Transactions on Communications*, vol. 18, no. 6, pp. 779–791, 1970.
 - [19] G. J. Foschini and M. J. Gans, "On limits of wireless communications in a fading environment when using multiple antennas," *Wireless Personal Communications*, vol. 6, no. 3, pp. 311–335, 1998.
 - [20] S. M. Kay, *Fundamentals of Statistical Signal Processing: Estimation Theory*, Prentice Hall, 1993.
 - [21] G. L. Turin, "The characteristics function of Hermitian quadratic forms in complex normal variables," *Biometrika*, vol. 47, pp. 199–201, 1960.
 - [22] M. Schwartz, W. R. Bennet, and S. Stein McGraw-Hill, *Communication Systems and Techniques*, 1966.
 - [23] J. Yang, M. Pantaleev, P. S. Kildal et al., "Cryogenic 213 GHz eleven feed for reflector antennas in future wideband radio telescopes," *IEEE Transactions on Antennas and Propagation*, vol. 59, no. 6, pp. 1918–1934, 2011.
 - [24] D. A. Hill, "Electronic mode stirring for reverberation chambers," *IEEE Transactions on Electromagnetic Compatibility*, vol. 36, no. 4, pp. 294–299, 1994.
 - [25] X. Chen, P. S. Kildal, C. Orlenius, and J. Carlsson, "Channel sounding of loaded reverberation chamber for over-the-air testing of wireless devices: coherence bandwidth versus average mode bandwidth and delay spread," *IEEE Antennas and Wireless Propagation Letters*, vol. 8, pp. 678–681, 2009.
 - [26] R. G. Vaughan and J. B. Andersen, "Fading correlations in wireless MIMO communication systems," *IEEE Transactions on Vehicular Technology*, vol. 36, no. 4, pp. 149–172, 1987.
 - [27] M. T. Ivrlač, W. Utschick, and J. A. Nossek, "Fading correlations in wireless MIMO communication systems," *IEEE Journal on Selected Areas in Communications*, vol. 21, no. 5, pp. 819–828, 2003.
 - [28] X. Chen, P. S. Kildal, and J. Carlsson, "Comparisons of different methods to determine correlation applied to multi-port UWB eleven antenna," in *Proceedings of the 5th European Conference on Antennas and Propagation (EUCAP '11)*, pp. 1776–1780, Rome, Italy, April 2011.
 - [29] D. A. Hill, "Plane wave integral representation for fields in reverberation chambers," *IEEE Transactions on Electromagnetic Compatibility*, vol. 40, no. 3, pp. 209–217, 1998.
 - [30] C. A. Balanis, *Antenna Theory: Analysis and Design*, John Wiley & Sons, 3rd edition, 2005.

Research Article

High Gain Array of Monopoles-Coupled Antennas for Wireless Applications

Ahmad El Sayed Ahmad,¹ Marc Thevenot,² Jean-Marie Floc'h,¹ and Mohamad Mantash¹

¹ IETR, CNRS, UMR 6164, 20 Avenue des Buttes de Coesmes, 35043 Rennes, France

² XLIM, CNRS, UMR 6172, 123 Avenue Albert Thomas, 87060 Limoges, France

Correspondence should be addressed to Ahmad El Sayed Ahmad, ahmad-khoder.el-sayed-ahmad@insa-rennes.fr

Received 7 June 2012; Revised 27 September 2012; Accepted 11 October 2012

Academic Editor: Huanhuan Gu

Copyright © 2012 Ahmad El Sayed Ahmad et al. This is an open access article distributed under the Creative Commons Attribution License, which permits unrestricted use, distribution, and reproduction in any medium, provided the original work is properly cited.

An array of monopole antennas over a ground plane that radiates a directive lobe in the end-fire direction are described in this paper. The design uses the rigorous method described by Drouet et al. 2008 in order to synthesize the radiation through the strong cumulative coupling between the monopoles. A gain higher than 20 dB was achieved in the end-fire direction over a 4.5% bandwidth. However, the antenna has been tilted in order to compensate the beam deviation caused by the edge diffraction. A prototype with 12 elements has been manufactured in order to validate the antenna principle and the whole antenna is successfully measured. The prototype was studied with the software CST-Microwave Studio and the feed network has been designed with Agilent ADS.

1. Introduction

This paper deals with the design of the vehicular antenna that must satisfy some particular requirements. Firstly, this antenna has to be integrated on the roof that induces a low-profile antenna working over a ground plane. Secondly, an end-fire antenna which radiates toward the horizon must be used to communicate with the base stations. Finally, the antenna gain must be high in order to reduce the number of base stations. The design of an antenna that satisfies all these specifications is very difficult to perform.

Linear monopole arrays are extensively used in many antenna systems due to their simplicity, low cost, polarization purity, reasonable bandwidth, and power-handling capability [1]. However, the strong mutual coupling between neighbored antenna elements also results in radiation patterns and matching degradations. The feed network can also be directly affected. It has been theoretically demonstrated that mutual coupling effects on radiation patterns can be reduced with appropriate loads [2–5].

The aim of this paper is to design a linear array of monopoles by managing the coupling. Moreover, the antenna design must be robust and easy to manufacture in

order to be integrated on a vehicle roof, and, thus, to undergo outdoor conditions such as rain and wind.

In the first part, the global design method will be briefly explained. Then, the principle, the design, and the performances of a linear array of 12 monopoles will be given. In the second part, an array of 4×12 monopoles fed by a feed network will be described. The last section discusses the design of 4×12 monopoles that would be compared to a Yagi antenna.

2. Basic Structure

2.1. Principle. The basic structure is composed of twelve monopoles and a feed network. The strong interactions between the monopoles need to design the feed network with a great accuracy in order to optimize the directivity.

The objective consists of the determination of the impedance matching and the incident power to reach both the objective radiation pattern and the best matching for the monopole array.

We employ the method described in [6] for the design of the array antenna with strong coupling: by using CST-Microwave studio we compute the [S] matrix and the 12

radiation patterns when the 12 monopoles are successively fed. These radiation patterns are ϕ_1 to ϕ_{12} (1). An objective radiation pattern ϕ_{obj} is proposed. This objective radiation pattern can be the linear combination of the radiation pattern of one monopole on its limited ground plane multiplied by an array factor (2). In this relation, d is the distance between each monopole and φ_i is the phase of the i th monopole.

Equation (1) provides the weights that must be applied to the monopoles' radiation pattern. Equation (3) leads to the antenna impedances to be considered as a reference (Z_{ref}) in order to reach the matching and (4) gives the input waves that the feed network must achieve:

$$[\phi_1 \phi_2 \cdots \phi_i] \begin{pmatrix} \beta_1 \\ \beta_2 \\ \vdots \\ \beta_i \end{pmatrix} \approx \phi_{\text{obj}} \quad \text{with } 1 \leq i \leq 12 \quad (1)$$

$$\phi_{\text{obj}} = \sum_{i=1}^{12} \exp[-(k_0 \cdot d \cdot \sin(\theta) + \varphi_i) \cdot i] \cdot \phi_{\text{monopole}} \quad (2)$$

$$Z_{\text{ref},i} = \left(\frac{50 \cdot [I + S](\beta)}{[I - S](\beta)} \right)^* \quad (3)$$

$$a_i = \sqrt{50} \cdot [I + S](\beta) \frac{\sqrt{\Re(Z_{\text{ref},i})}}{Z^*_{\text{ref},i}}, \quad (4)$$

where ϕ_i is the i th monopole radiation pattern, ϕ_{obj} is the objective radiation pattern, β_i is the weight that must be applied to the i th monopole radiation pattern, d is the distance between each monopole, $k_0 = 2\pi/\lambda_0$ (λ_0 free space wavelengths), φ_i is the phase shift at i th monopole, and $[S]$ is the coupling matrix.

2.2. Design and Performances of the Array of 12 Monopoles. As explained in Section 1, the application is a communication system that uses the WIMAX protocol between a vehicle and base stations. The objective is to establish a high-gain monopole array that radiates a directional beam in the azimuthal plane within the frequency band 5.47 GHz–5.725 GHz. In this section, we propose the complete design of the array of monopoles with its feed network. The optimization frequency is 5.6 GHz.

In order to achieve a radiation with a single lobe in the direction of the array alignment, the space between two nearby monopoles must stay lower than $0.5\lambda_0$: we have chosen $0.45\lambda_0$ (24.12 mm) for our design. Twelve monopoles are set on a ground plane whose dimensions are $L_x = 100$ mm and $L_y = 330$ mm (Figure 1). The monopole lengths are listed into Table 1 (length) and their diameter is 2.53 mm. The connections between the monopoles and the feed network's ports are achieved with 50Ω coaxial transitions which are drilled through the ground plane (Figure 2). The feed network is printed back to the antenna ground plane, onto a 0.508 mm thick Duroïd 6002 substrate ($\epsilon_r = 2.94$, $\tg\delta = 0.0012$).

The array of monopoles is positioned on a limited ground plane. In the limited ground plane size case, the



FIGURE 1: The array antenna is composed of 12 monopoles.

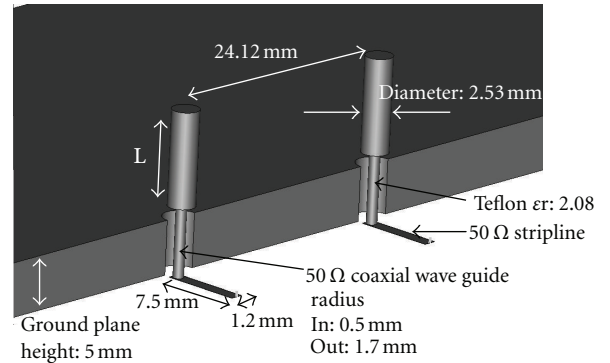


FIGURE 2: The monopoles are fed by a coaxial guide drilled through the ground.

well-known scattering effects on the ground plane edges alter the radiation pattern [7–9] (Figure 3). First of all, the interferences induce maxima and minima field on the radiation pattern. Their angular position is obviously related to the ground plane size. Then, we can observe the classic beam deviation in the elevation plane, which is caused by the scattering on the edges of the limited ground plane, since the main beam direction does not coincide with the horizon. To achieve the objective radiation pattern (we defined an angle $\theta = 75^\circ$), we apply the array factor (2) with

$$k_0 \cdot d \cdot \sin(\theta) + \varphi_i = m \cdot 2 \cdot \pi \Rightarrow \varphi_i = 203^\circ. \quad (5)$$

It should be stressed that these results are approximations since the analysis considers the monopoles do not interfere with each other. The radiation pattern illustrated in Figure 4 (monopole x -array factor) can be used as the objective radiation pattern ϕ_{obj} . In the next step, we have used CST Microwave studio to achieve the full-wave analysis of the whole antenna structure. As an example, only 3 monopole radiation patterns are plotted in Figure 3.

According to (1), the weights β are deduced and written in Table 1. Thus, Figure 4 points out the resemblance between the objective radiation pattern and the linear combination of the radiation patterns of monopoles weighted by the coefficients β .

Figures 5 and 6 show the scattering matrix of the monopole antenna. Regarding Figure 6, these interactions should not be omitted when connecting the array monopoles with the feed network. The coupling between nearby monopoles is greater than -13 dB.

The optimum weights (a_i) and the input impedances ($Z_{\text{ref},i}$) which simultaneously perform the objective radiation

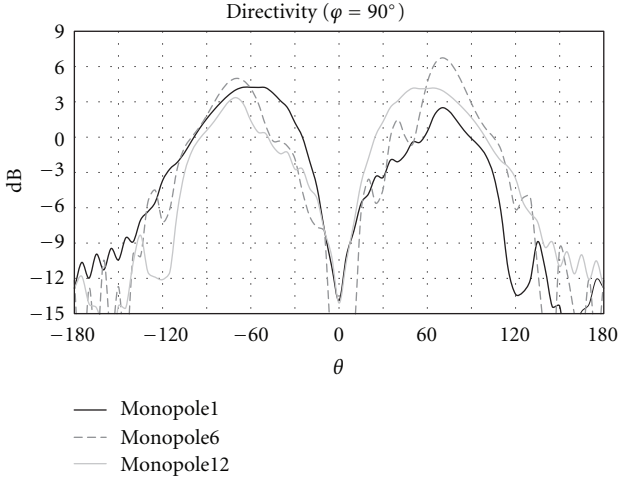


FIGURE 3: Radiation patterns of monopoles when the monopoles are successively fed.

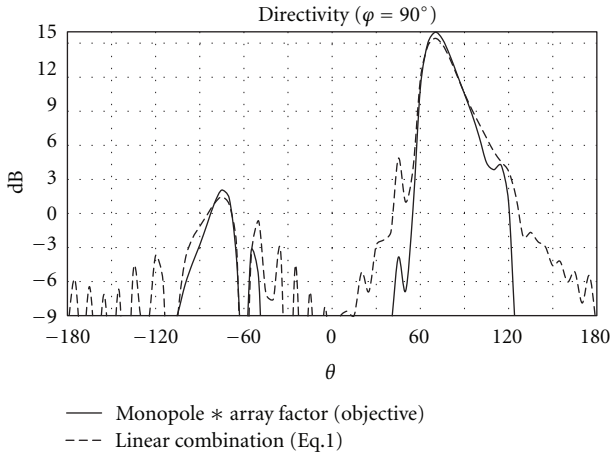


FIGURE 4: Comparison of the objective radiation pattern (radiation pattern of monopole x -array factor) with the linear combination of the radiation patterns of monopoles ($f = 5.6$ GHz).

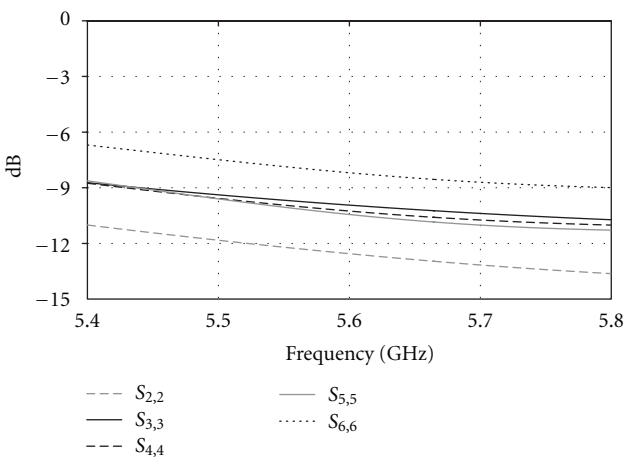


FIGURE 5: Some S_{ii} parameters of the array of monopoles.

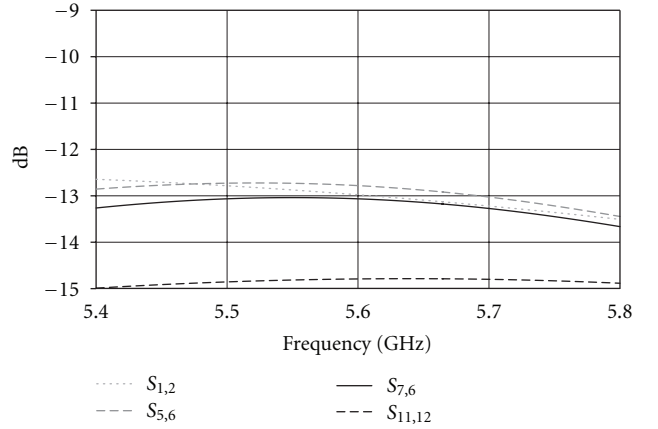


FIGURE 6: Some S_{ij} parameters of the array of monopoles.

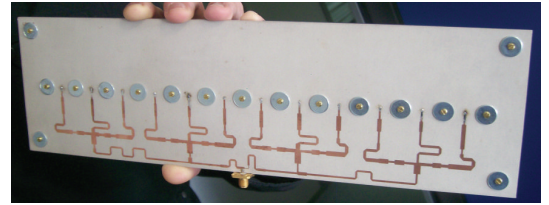


FIGURE 7: The feed network is designed to maximize the efficiency of the strongly coupled monopoles.

and the matching of all the feeding ports can be calculated using (3), (4), the scattering matrix [S], and the β vector. These values are given in Table 1 (columns 4 and 5) with the optimized monopole lengths. These have been set to comply with the different impedance values resulting from the synthesis procedure and to minimize the feed distribution network complexity.

The design of the microstrip feed network has been made with the Agilent ADS software in order to perform the weights and the impedance matching specified in Table 1. The realized feed network is shown in Figure 7.

In order to perform the numerical validation, the monopole simulation and the feed network design are numerically connected together. Using the CST software, this entire structure simulation provides the performances of the whole array antenna (the 12 monopoles and the feed network). The radiation pattern, the gain, and the return loss are computed. Figure 8 plots the radiation pattern in the plane $\phi = 90^\circ$. This is the plane which is parallel to the array alignment. We can observe that the entire structure simulation agrees very well with the objective radiation pattern (linear combination of the radiation patterns of the monopoles). So, the feed network operates properly through the couplings. Figure 9 presents the radiation pattern in 3D at 5.6 GHz; the maximum simulated directivity is 15.6 dB. The main beam direction does not coincide with the horizon ($\theta = 90^\circ$); it will be necessary to compensate this deviation by an inclination of the whole antenna. Indeed, it is essential for our application that the maximum gain is radiated in the base stations direction.

TABLE 1: Normalized incident waves and reference impedances which optimize the efficiency of the array antenna for a specified radiation pattern (5.6 GHz).

Monopoles	Length (mm)	β (= weights for the coupled radiation patterns)	Normalized incident waves (a_i) and antenna impedances ($Z_{\text{ref},i}$) that optimize the efficiency	
			a_i	$Z_{\text{ref},i}$
1	10.8	$0.286 \cdot \exp(-j^*48^\circ)$	$0.288 \cdot \exp(-j^*49^\circ)$	$29 + j^*13$
2	9.8	$0.293 \cdot \exp(j^*155^\circ)$	$0.30 \cdot \exp(j^*152^\circ)$	$32 + j^*10$
3	9.3	$0.279 \cdot \exp(-j^*3^\circ)$	$0.286 \cdot \exp(-j^*6^\circ)$	$31 + j^*9$
4	9.3	$0.284 \cdot \exp(-j^*155^\circ)$	$0.291 \cdot \exp(-j^*146^\circ)$	$30 + j^*1$
5	9.3	$0.284 \cdot \exp(j^*47^\circ)$	$0.287 \cdot \exp(j^*35^\circ)$	$27 - j^*2$
6	8.8	$0.280 \cdot \exp(-j^*120^\circ)$	$0.283 \cdot \exp(-j^*124^\circ)$	$29 + j^*7.5$
7	8.8	$0.266 \cdot \exp(j^*82^\circ)$	$0.262 \cdot \exp(j^*79^\circ)$	$24 + j^*8.5$
8	8.8	$0.264 \cdot \exp(-j^*74^\circ)$	$0.251 \cdot \exp(-j^*77^\circ)$	$20 + j^*8.5$
9	8.8	$0.254 \cdot \exp(j^*131^\circ)$	$0.227 \cdot \exp(j^*124^\circ)$	$15 + j^*3$
10	8.8	$0.275 \cdot \exp(-j^*24^\circ)$	$0.257 \cdot \exp(-j^*35^\circ)$	$18 - j^*1.5$
11	8.8	$0.319 \cdot \exp(j^*180^\circ)$	$0.323 \cdot \exp(j^*165^\circ)$	$28 - j^*7$
12	8.3	$0.361 \cdot \exp(j^*0^\circ)$	$0.377 \cdot \exp(j^*0^\circ)$	$48 + j^*17$

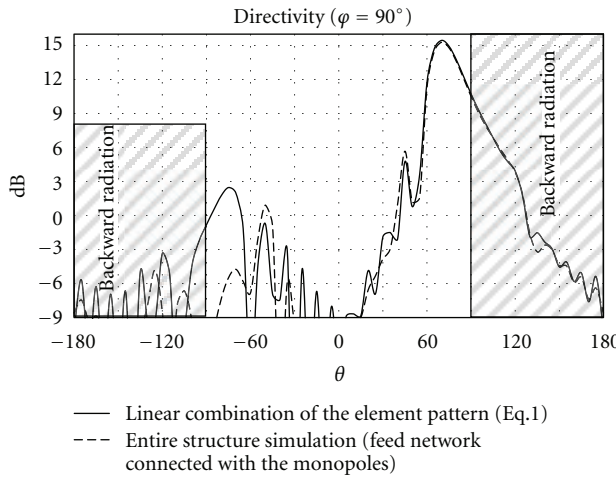


FIGURE 8: Simulated radiation pattern (directivity) comparison at $f = 5.6$ GHz.

The return loss at the input of the feed network is plotted in Figure 10 (simulation). The level is lower than -15 dB over the operating frequency bandwidth. This numerical validation shows that the radiation pattern is successfully synthesized as well as the impedance matching of every antenna port through the couplings. Although the feed network has been optimized to deal with the antenna couplings at 5.6 GHz, we have evaluated the performances of the entire structure (12 monopoles connected with the feed network) from 5.47 GHz to 5.725 GHz.

The antenna gain is 14.7 dB over the 5.47 GHz–5.725 GHz operating bandwidth (Figure 11). The directivity and the gain difference are mainly due to the dielectric losses in the strip line circuit.

2.3. Measurements. The array of monopoles and the feed network were manufactured (Figures 1 and 7). The feed

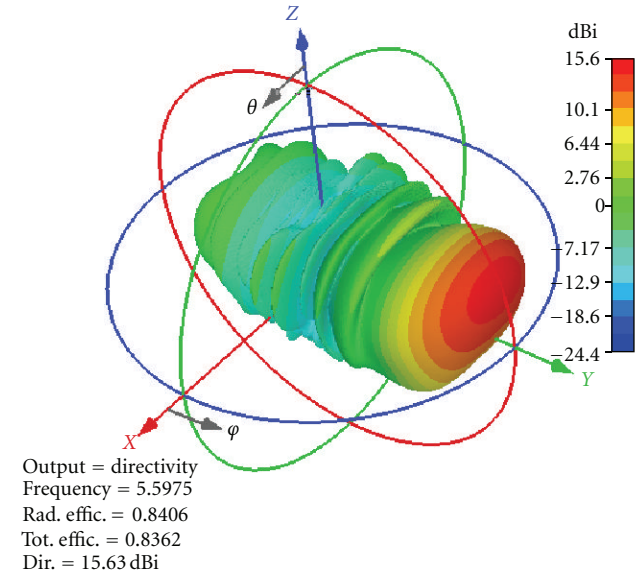


FIGURE 9: Simulated radiation pattern in 3D (directivity) at $f = 5.6$ GHz.

network is glued back to the ground plane and screws were added to secure the RF contacts. We have checked that interactions between the screws and the circuit are negligible. An SMA connector is at the input port.

Measurements were achieved in an anechoic chamber. The return loss of the tested antenna is in Figure 10 (measurement). This measurement is compared with the simulation: both S_{11} are close to -15 dB over the operating frequency bandwidth. A slight discrepancy of 50 MHz can be observed compared to the simulation, but it represents only 0.9% of the frequency shift that can be due to the mesh accuracy during simulation or manufacture tolerance. Figure 12 compares the measured radiation pattern with the

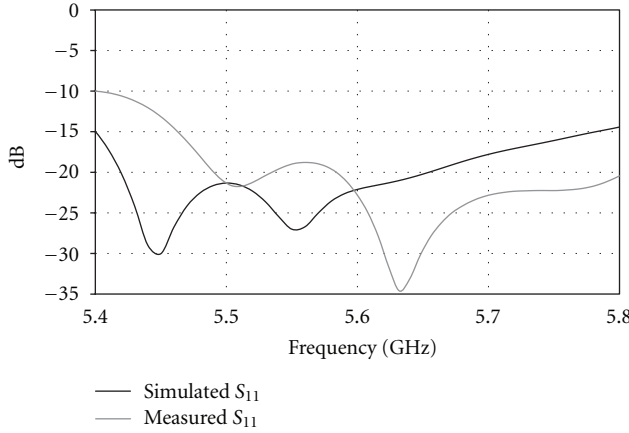


FIGURE 10: Comparison of the S_{11} of the entire structure simulation (12 monopoles connected with the feed network) with the realized structure.

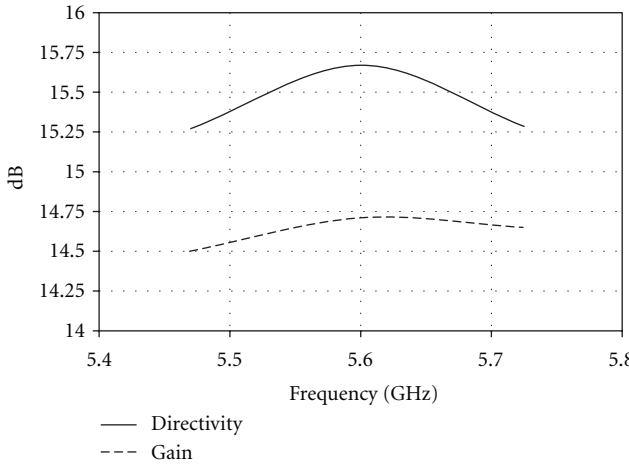


FIGURE 11: Directivity and gain versus the frequency ($\theta = 75^\circ$, $\varphi = 90^\circ$).

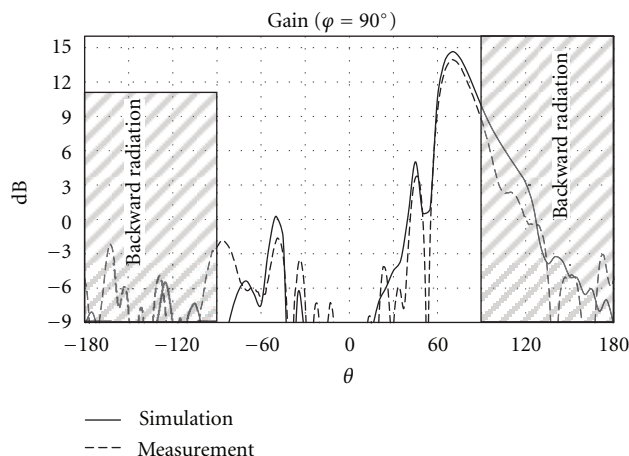


FIGURE 12: Comparison of the objective radiation pattern simulated with the radiation pattern measured at $f = 5.6$ GHz.

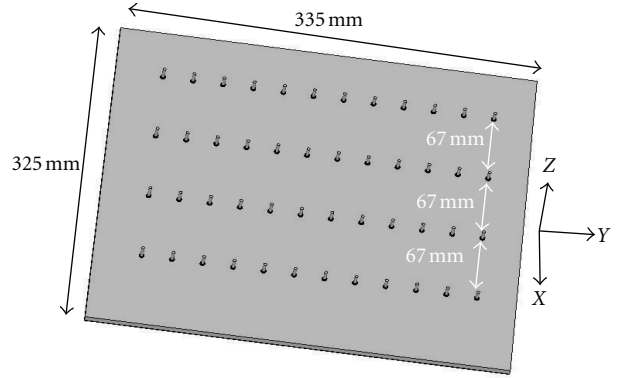
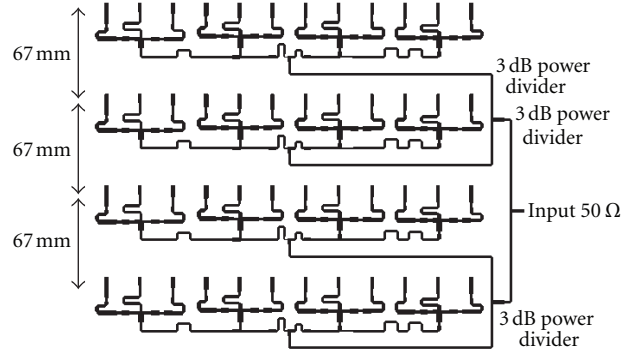


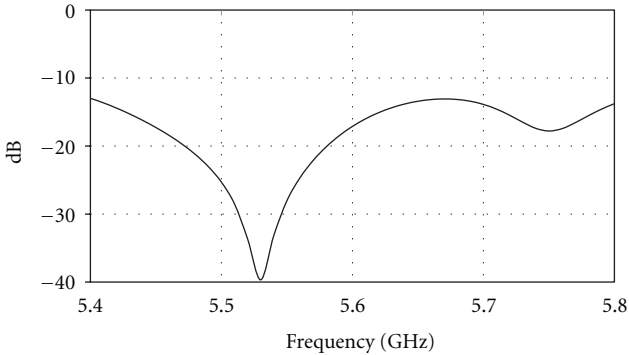
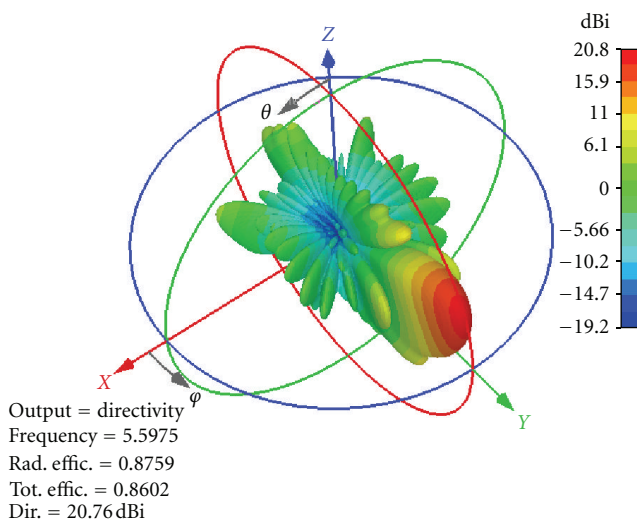
FIGURE 13: Array of 4×12 monopoles designed with CST Mws separated by $0.45 \lambda_0$ along [oy] and $1.25 \lambda_0$ along [ox].



theoretical one over 360° in the plane of the array alignment ($\varphi = 90^\circ$). The measured gain agrees very well with the prediction. We can conclude that the design is reliable. The feed network operates properly through the couplings. The differences between the simulated and the measured gains are lower than 0.5 dB. Metallic losses in the feed network and the uncertainty accuracy of our anechoic chamber can be responsible for this discard.

3. 2D Array of 4×12 Monopoles (4 Subarrays)

The well-behaved experimental results validate the principle of the 12-monopole linear array. The linear array of twelve monopoles (along [oy]) provided a gain of 14.7 dB at 5.6 GHz. Figure 9 shows that the radiation pattern contains low side lobes in the perpendicular plane [ox] to the array of monopole plane alignment [oy]. In order to increase the gain, a 2D array of 4×12 monopoles was designed (Figure 13). Four sub-arrays, where each of them is described in Section 2, have been used to make the 48-monopole array. Therefore, the 4 sub-arrays are $1.25 \lambda_0$ spaced out in order to avoid the interferences in these directions. Obviously, these sub-arrays alignment allow the constructive interference and so increase the gain in the end-fire direction.

FIGURE 15: Modulus of S_{11} .FIGURE 16: Simulated radiation pattern in 3D (directivity) of 4×12 monopoles at 5.6 GHz.

3 dB power dividers have been designed to connect the feed networks. $1.25\lambda_0$ (67 mm) is sufficient in order to avoid the interferences between the lines of the feed network. The corresponding layout of the feed network of 4×12 monopoles is shown in Figure 14. The return loss at the input of the feed network is plotted in Figure 15. The level is lower than -15 dB over the operating frequency bandwidth. The 3D (Figure 16) radiation pattern shows a very directive lobe. A 20.8 dB maximum directivity is obtained at the end-fire direction. An increase of 5.2 dB has been obtained compared to the case with a single subarray (12 monopoles) (Figure 9). The antenna gain is 20 dB over the 5.47 GHz–5.725 GHz operating bandwidth (Figure 17). The directivity and the gain difference are mainly due to the dielectric losses in the strip line circuit. Indeed, the insertion losses are very low because the antenna reflection coefficient is lower than -15 dB over the 5.47 GHz–5.725 GHz band (Figure 15).

The 4×12 monopoles are sufficient to have the gain required in the specifications. The antenna was 15° tilted to give back the main beam deviation caused by the scattering at the ground plane edges.

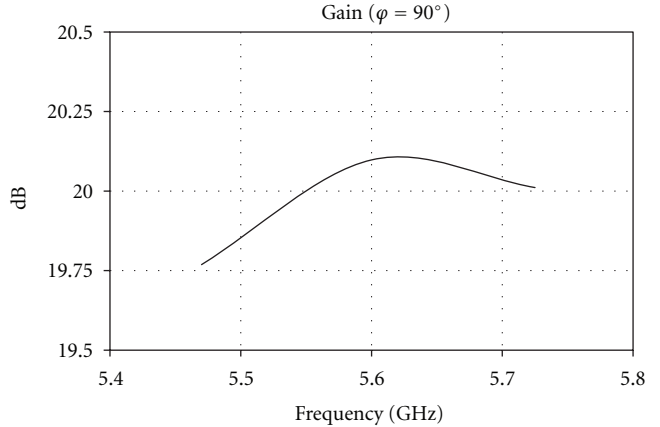
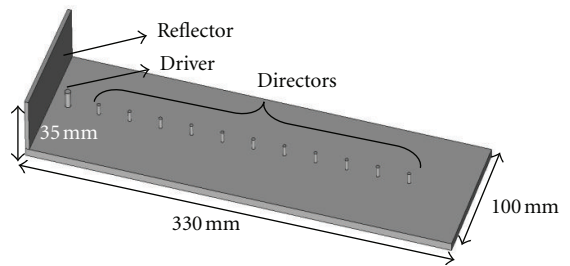
FIGURE 17: Gain versus the frequency ($\theta = 75^\circ, \varphi = 90^\circ$).

FIGURE 18: Proposed Yagi antenna.

4. Yagi Antenna

In order to check the interest to develop the complete method for the conception, we have made another antenna. The proposed antenna is a Yagi-Uda antenna.

Yagi antennas of three or more elements are widely used, although a thorough study is lacking today because of the many parameters, each element having three variables, length, spacing, and the diameter of conductor. Almost all multielement Yagis are invariably designed empirically. In [10], Yagi antenna of three elements was presented. It has been shown the gain over a half-wave dipole of a three element Yagi with various director lengths and spacing. This study shows that as the spacing between director and driver decreases, the optimum length of the director increases.

It has been documented in [11–13] that the dimension ratio of the reflector to the driven element can be somewhere between 1.1 and 1.3. The dimension ratio of the director to the driven element can be between 0.8 and 0.95. The distance between the centers of the reflector and the driven element should be about 0.25 free-space wavelengths, while the separation between the centers of the director and the driven element and the separation between the directors themselves should be between 0.3 and 0.4 free-space wavelengths.

The antenna characteristics such as gain, front-to-back ratio, beamwidth, and center frequency can be altered by changing the length of the driven element, the length of the parasitic elements, spacing between reflector and dipole, and spacing between director and dipole [14].

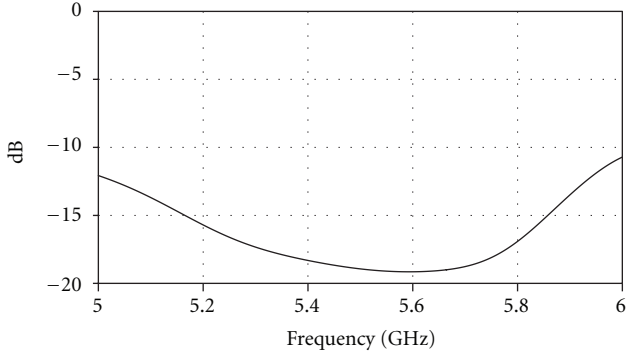
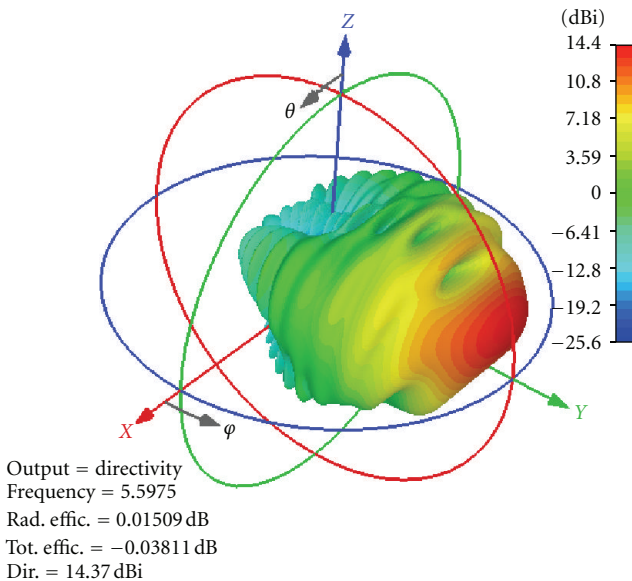
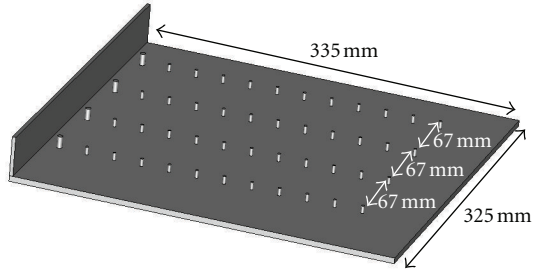
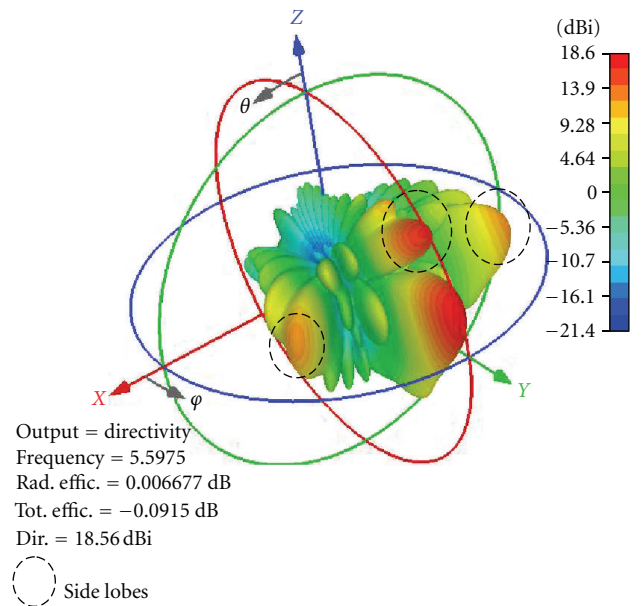
FIGURE 19: S_{11} of the Yagi antenna.

FIGURE 20: Simulated radiation pattern in 3D (directivity) of Yagi antenna at 5.6 GHz.

The proposed antenna consists of a monopole as a driven element, a reflector, and eleven directors as shown in Figure 18. To facilitate the design, this antenna is designed using the same size of the prototype described in Section 2. Since our application requires only one high-gain radiation direction, it is proceeded to prohibit the radiation in the half space behind the antenna. The backfire radiation can be avoided with some non excited elements named “reflectors” or with a vertical metallic plane. Intended for simplicity constraints, the second solution is selected. So, the driver monopole must be spaced out of a $\lambda_0/4$ (13.4 mm) distance from the reflector plane. This separation allows a constructive interference between the reflected fields and the direct waves. In this case and according to the images theory, the antenna gain should be 3 dB increased at the end-fire direction.

The separation between the centers of the director and the driven element and the separation between the directors themselves is 0.45 free-space wavelength (24.12 mm). The director lengths are 6.7 mm ($\lambda_0/8$) and their diameters are

FIGURE 21: Array of $4 \times$ Yagi antenna.FIGURE 22: Simulated radiation pattern in 3D (directivity) of $4 \times$ Yagi antenna at 5.6 GHz.

2.53 mm. These directors are shortcircuited with the ground plane. The length of the driver monopole is 10.32 mm; its diameter is 4.53 mm.

The yagi antenna is matched to -18 dB in simulation over a bandwidth 5.47 GHz–5.725 GHz (Figure 19). The simulated radiation pattern in 3D is presented in Figure 20; the maximum directivity is 14.3 dB at the end-fire direction.

In order to increase the directivity, a 2D array of $4 \times$ Yagi antenna was designed (Figure 21). The antenna was designed using the same size of the prototype described in Section 3 to make a true comparison between the array of monopole antenna and the Yagi antenna. Figure 22 presents the radiation pattern at 5.6 GHz. We obtain a maximum directivity of 18.5 dB. The comparison of radiation in the Cartesian plane between the array of monopoles and the yagi antenna is shown in Figure 23. The radiation pattern is compared versus φ at $\theta = 75^\circ$ (maximum radiation). We can observe the first side lobe level of yagi radiation pattern is around 12 dB; it is -6 dB below the main lobe which explains the maximum directivity of yagi antenna is 2.3 dB lower than the radiation of the monopole array.

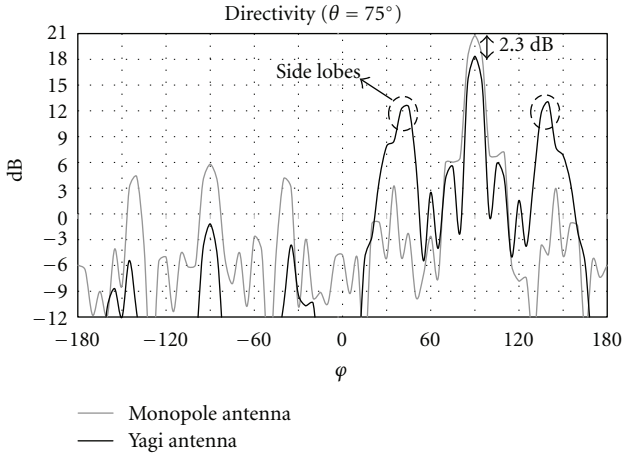


FIGURE 23: Comparison of the radiation pattern of 4×12 monopoles with the $4 \times$ Yagi array antenna.

The advantages of the monopole antenna compared to the Yagi antenna are

- (1) the array of monopole antenna designed in Section 3 does not need to a reflector plane to radiate on the end-fire direction,
- (2) the radiation pattern of monopole antenna does not contain significant side lobes levels,
- (3) the maximum level of radiation of the monopoles antenna is greater than the yagi,

The disadvantages of the monopole antenna compared to the Yagi antenna is the feed network.

5. Conclusion

In this paper, a low-profile antenna with a ground plane has been presented. The purpose was to design a high-gain antenna (single end-fire beam) which must be positioned on a vehicle roof in order to communicate with the far base stations. As a first step, an array of 12 monopoles was designed. In such a structure, the monopoles strongly interact with each other.

In our study, the feed network has been designed to deal with the couplings by considering as a reference the impedances and the input waves that optimize the efficiency of the antenna.

The feed network and the monopole array were manufactured. The whole antenna was successfully tested. The antenna was tilted to give back the main beam deviation caused by the scatterings on the ground plane edges.

As a second step, an array of 4×12 monopoles has been designed in order to increase the gain. A gain higher than 20 dB has been achieved over a 4.5% bandwidth.

Finally, in order to check the interest to develop the complete method for the conception, we have made another antenna. The proposed antenna is a Yagi-Uda antenna. The radiation of this antenna presents high side lobe levels. The maximum radiation on the end fire is lower than

the radiation of the monopole array. In conclusion, as the method takes into account couplings, a particular beam pointing with reduced or controlled side lobes can be achieved easily.

References

- [1] B. Tomasic and A. Hessel, "Linear array of coaxially fed monopole elements in a parallel plate waveguide-I: theory," *IEEE Transactions on Antennas and Propagation*, vol. 36, no. 4, pp. 449–462, 1988.
- [2] D. M. Pozar, "The active element pattern," *IEEE Transactions on Antennas and Propagation*, vol. 42, no. 8, pp. 1176–1178, 1994.
- [3] J. P. Daniel and C. Terret, "Mutual coupling between antennas optimization of transistor parameters in active antenna design," *IEEE Transactions on Antennas and Propagation*, vol. AP-23, no. 4, pp. 513–516, 1975.
- [4] A. K. Bhattacharyya, *Phased Array Antennas: Floquet Analysis, Synthesis, BFNs, and Active Array Systems*, John Wiley & Sons, Hoboken, NJ, USA, 2006.
- [5] R. J. Mailloux, *Electronically Scanned Array. Synthesis Lecture on Antennas*, Morgan & Claypool Publishers, Constantine Balanis, Ariz, USA, 2007.
- [6] J. Drouet, M. Thevenot, R. Chantalat et al., "Global synthesis method for the optimization of multi feed EBG antennas," *International Journal of Antennas and Propagation*, vol. 2008, Article ID 790358, 6 pages, 2008.
- [7] S. K. Sharma and L. Shafai, "Beam focusing properties of circular monopole array antenna on a finite ground plane," *IEEE Transactions on Antennas and Propagation*, vol. 53, no. 10, pp. 3406–3409, 2005.
- [8] C. Phongcharoenpanich, S. Suriya, T. Lertwiriyaprapa, P. Ngamjanyaporn, and M. Krairiksh, "Analysis of circular array of monopole on the ground plane radiating linearly polarized conical beam for wireless LAN applications," in *Proceedings of the 5th International Symposium on Antennas, Propagation and EM Theory*, pp. 646–649, Beijing, China, August 2000.
- [9] V. Volski and G. A. E. Vandebosch, "Modelling of microstrip antennas on a finite ground plane using the 2D physical optics model," *Microwave and Optical Technology Letters*, vol. 40, no. 1, pp. 26–29, 2004.
- [10] H. Jasik, *Antenna Engineering Handbook*, McGraw-Hill Book Company, New York, NY, USA, 1961.
- [11] J. Huang and A. C. Densmore, "Microstrip Yagi array antenna for mobile satellite vehicle application," *IEEE Transactions on Antennas and Propagation*, vol. 39, no. 7, pp. 1024–1030, 1991.
- [12] H. Yagi, "Beam transmission of the ultra short waves," *IRE Proceedings*, vol. 16, no. 6, pp. 715–740, 1928.
- [13] C. A. Balanis, *Antenna Theory. Analysis and Design*, John Wiley & Sons, New York, NY, USA, 1997.
- [14] S. K. Padhi and M. E. Bialkowski, "Parametric study of a microstrip Yagi antenna," in *Proceedings of the Asia-Pacific Microwave Conference*, pp. 715–718, Sydney, NSW, Australia, December 2000.

Research Article

Validation of Antenna Modeling Methodology in IMT-Advanced Channel Model

Jianhua Zhang and Chun Pan

Key Laboratory of Universal Wireless Communications, Ministry of Education, Wireless Technology Innovation Institute, Beijing University of Posts and Telecommunications, Beijing 100876, China

Correspondence should be addressed to Chun Pan, panchun1987@gmail.com

Received 6 July 2012; Revised 28 September 2012; Accepted 7 October 2012

Academic Editor: Guangyi Liu

Copyright © 2012 J. Zhang and C. Pan. This is an open access article distributed under the Creative Commons Attribution License, which permits unrestricted use, distribution, and reproduction in any medium, provided the original work is properly cited.

In this paper, the antenna modeling method in the International Mobile Telecommunications-Advanced (IMT-Advanced) channel model is validated by field channel measurements in the indoor scenario at 2.35 GHz. First, the 2×2 MIMO channel impulse responses (CIRs) are recorded with practical antennas as references. Second, the CIRs are reconstructed from the available IMT-Advanced channel model with field patterns of the practical antennas and updated spatial parameters extracted from the similar scenario measurements. Then comparisons between the field CIRs and the reconstructed CIRs are made from coherent bandwidth, eigenvalue dispersion, outage capacity, and ergodic channel capacity. It is found that the reconstructed results closely approximate real results in the coherent bandwidth and correctly describe the statistical characteristics in frequency domain. Compared to the field CIRs, the spatial correlation of the reconstructed CIRs with both types of antenna have a wider range that causes the underestimation of the 5% channel outage capacity. Due to the negligence of the coupling among the antennas and the near field effect of antenna, this modeling method will have a great impact on the characteristics of radio channels, especially on the spatial characteristics.

1. Introduction

Multiple-input multiple-output (MIMO) systems, which deploy spatially separated multiple antenna elements at both ends of the transmission link, have to be considered as one of the most promising approaches for high data rate and more reliable wireless systems without extra bandwidth. It was shown that the potential channel capacity of such MIMO systems grows linearly with antenna pairs in independent identically distributed (i.i.d.) channel model [1, 2], but the channel fading correlation affects the capacity by modifying the distributions of the gains of these parallel channels [3]. According to this, the capacity ultimately depends on the propagation channel model used.

Recently, to obtain an accurate channel capacity estimation, many verified channel models [4] were used. In [5], a model based on the Kronecker structure of the channel covariance matrix has been assumed to analyze the channel capacity and was extended to a wideband MIMO

channel model in [6]. But in [7], it was confirmed that the Kronecker model cannot describe the multipath structure correctly. For example, the 8×8 MIMO capacity predicted by the Kronecker model is always below the capacity extracted directly from the filed measurement. Another important wideband MIMO spatial channel model, the International Mobile Telecommunications-Advanced (IMT-Advanced) channel model, is regarded as an appropriate channel model to predict the MIMO channel capacity. This model is a geometry-based stochastic channel model, which adopts the multipath superposition method to generate channel coefficients. By separating multipath channel model into multipath propagation channel model and antenna pattern model, this model not only characterizes the multipath channel parameter but also can be configured with any type of antenna array. So this model is popular to investigate the impact of antenna array configuration on the capacity and the reliability of algorithm. The effects of the user's presence on the performance of a MIMO system in data

and in voice usage scenarios are investigated in [8], which concludes that the subscriber's usage has much impact on the link performance.

Although this modeling method is convenient to analyze the influences of different antenna configuration on the channel characteristics, based on the double-directional channel model, the multipath parameters are generated independently of a specific antenna, its configuration, and its pattern. Meanwhile, this channel model ignores the nonideal issues on the antennas which will influence the propagation characteristics, such as practical antenna pattern, coupling among the antennas, and human body. To the author's knowledge, there is no investigation to validate the impact of the practical antenna on the spatial channel model of MIMO. So it is not clear if it is accurate enough to model the antenna impact by combining the antenna pattern and multipath propagation channel.

In this paper, the field-measured MIMO channel impulse responses (CIRs) is firstly recorded with practical dipole antenna (DPA) and real terminal planar inverted-F antenna (PIFA) [9] as the reference, in which the channel measurements are conducted in indoor scenario. Second, the CIRs are reconstructed from IMT-Advanced channel model with updated spatial parameters which were measured with omnidirectional antenna array (ODA) and extracted by Space alternating generalized expectation maximization (SAGE) algorithm, and the practical antenna pattern's impact is also incorporated by combining the antenna pattern and multipath propagation channel by matrix manipulation. Then the comparisons between field data and reconstructed data are made from some metrics of MIMO channel [10], such as coherent bandwidth, eigenvalue dispersion, outage capacity, and ergodic channel capacity.

The remainder of the paper is organized as follows. The statistical channel model, channel measurements, and data postprocessing are introduced in Section 2. Section 3 presents the results and the analysis. The analysis of channel characteristics between the measured data and the reconstructed data is presented, for example, the frequency domain in Section 3.1 and the spatial domain in Section 3.2, respectively. The capacity analysis is presented in Section 3.3. Conclusions are drawn in Section 4.

2. Validation Framework

In order to validate the accuracy of antenna pattern modeling methodology of IMT-Advanced channel model, the linear time variant MIMO channel response is first defined by the MIMO channel complex matrix $\mathbf{H}(t, \tau)$ of dimension $U \times S$, where U is the number of receiving antennas and S is the number of transmitting antennas. The channel matrix relates the $S \times 1$ complex input vector \mathbf{x} to the $U \times 1$ complex output vector \mathbf{y} during a symbol period after adding the $U \times 1$ white Gaussian noise vector \mathbf{w} as follows:

$$\mathbf{y}(t) = \sum_{\tau} \mathbf{H}(t, \tau) \mathbf{x}(t) + \mathbf{w}(t). \quad (1)$$

2.1. Channel Model: IMT-Advanced. In IMT-Advanced channel model [11], the spatial and temporal distributions are parameterized to characterize the MIMO channel. One realization consists of six paths composed of twenty subpaths each. The parameters of all subpaths are calculated for each realization. A temporal channel matrix $\mathbf{H}(t_0, \tau_n)$ at t_0 is created by IMT-Advanced program for each path through the superposition of the subpaths. The entries $h_{u,s}(t_0, \tau_n)$ of $\mathbf{H}(t_0, \tau_n)$ are

$$\begin{aligned} h_{u,s}(t_0, \tau_n) = & \sum_{m=1}^M \mathbf{F}_{rx,u}^T(\Omega_{n,m}) \mathbf{A}_{n,m} \mathbf{F}_{tx,s}(\Phi_{n,m}) \\ & \times \exp(jd_u 2\pi\lambda_0^{-1} \sin(\Omega_{n,m})) \\ & \times \exp(jd_s 2\pi\lambda_0^{-1} \sin(\Phi_{n,m})) \\ & \times \exp(j2\pi f_{d,n,m} t_0). \end{aligned} \quad (2)$$

The indexes u and s correspond to the receiving and the transmitting antenna elements, respectively. The λ_0 is the wavelength of the carrier. The number of paths is indexed by $n = \{1, \dots, 6\}$ and the number of the subpaths is $m = \{1, \dots, 20\}$. The $\mathbf{F}_{rx,u}$ and $\mathbf{F}_{tx,s}$ are defined as the field pattern of the receiving and the transmitting antenna elements, respectively, in (3) and (4) as follows:

$$\mathbf{F}_{rx,u}(\Omega_{n,m}) = \begin{bmatrix} \mathbf{F}_{rx,u,V}(\Omega_{n,m}) \\ \mathbf{F}_{rx,u,H}(\Omega_{n,m}) \end{bmatrix}, \quad (3)$$

$$\mathbf{F}_{tx,s}(\Phi_{n,m}) = \begin{bmatrix} \mathbf{F}_{tx,s,V}(\Phi_{n,m}) \\ \mathbf{F}_{tx,s,H}(\Phi_{n,m}) \end{bmatrix}. \quad (4)$$

The d_u stands for the distance between the u th receiving antenna element and the first element, the $\mathbf{F}_{rx,u,p}$ is the field pattern of the u th receiving antenna element on the p th polarization, and $p = \{1, 2\}$. For transmitting antenna elements, the d_s and $\mathbf{F}_{tx,s,p}$ hold the same meanings with the d_u and $\mathbf{F}_{rx,u,p}$, respectively. The τ_n , $f_{d,n,m}$, $\Phi_{n,m}$, and $\Omega_{n,m}$ denote the propagation delay, the doppler shift, the azimuth of departure (AoD), and the azimuth of arrival (AoA) of the (n, m) propagation subpath. And the polarization matrix of the (n, m) subpath $\mathbf{A}_{n,m}$ is defined by

$$\mathbf{A}_{n,m} = \begin{bmatrix} \alpha_{n,m,VV} & \alpha_{n,m,VH} \\ \alpha_{n,m,HV} & \alpha_{n,m,HH} \end{bmatrix}, \quad (5)$$

where α_{n,m,p_1,p_2} denote the polarization gain of the (n, m) subpath from the p_1 th polarization component to the p_2 th polarization component.

2.2. Validation Methodology. The rational of the IMT-Advanced channel model is based on the concept of the double-directional mobile radio channel [12]. By separating radio channel model (including antenna) into multipath propagation channel model (including none of the antennas) and antenna pattern model, this modeling method is popular in the researches with multiple antennas at both sides of communication link. During the modeling of CIRs, the IMT-Advanced channel model combines antenna response

and multipath propagation channel by matrix manipulation to obtain the reconstructed CIRs. The feasibility of this methodology will be focused on in this paper.

In this paper, the CIRs $\mathbf{H}(t, \tau)$ in (1) are obtained, respectively, by field measurement and model reconstruction. The direct data (filed measured) \mathbf{H}^{meas} is recorded by channel sounder with DPA array and the real terminal PIFA. The indirect data $\mathbf{H}^{\text{model}}$ is reconstructed by IMT-Advanced channel model with antenna pattern of the same antenna array used in direct data recording and extracted propagation channel parameters from measurement with ODA in the same scenarios. In the following subsections, the insight into the channel measurement and channel reconstruction is presented.

So lots of channel measurement campaigns are conducted to obtain the raw data. According to the specific requirements, three types of measurement antenna arrays are needed, including DPAs, PIFA, and ODA. Furthermore, the antenna patterns of DPA and PIFA need to be calibrated as \mathbf{F}^{DPA} and \mathbf{F}^{PIFA} before measurement. At the end of data acquisition, four groups of CIRs are obtained. They are $\mathbf{H}_{\text{DPA}}^{\text{meas}}$ collected from field measurement with DPAs, $\mathbf{H}_{\text{PIFA}}^{\text{meas}}$ collected from field measurement with PIFA, $\mathbf{H}_{\text{DPA}}^{\text{model}}$ reconstructed by IMT-Advanced channel model with the antenna pattern of DPAs, and $\mathbf{H}_{\text{PIFA}}^{\text{model}}$ reconstructed by IMT-Advanced channel model with the antenna pattern of PIFA. After acquisition of CIRs, the analysis on the channel characteristics will be performed.

2.3. Measurement Antenna. In the field channel measurement, three types of antenna array are used during the measurement, including DPA, PIFA and ODA. The field CIRs \mathbf{H}^{meas} are collected by using DPA and PIFA as measurement antenna array. At transmitter (Tx), two DPAs with $4\lambda_0$ antenna spacing are used. Meanwhile two DPAs with $1/2\lambda_0$ antenna spacing and a basic PIFA are used at receiver (Rx), respectively. The measured far field radiation patterns \mathbf{F}^{DPA} and \mathbf{F}^{PIFA} are given in Figure 1 for each of the MIMO antennas. The patterns are measured in dBi on the azimuth plane (x - y) for all antennas are given in Figure 2. Both \mathbf{F}^{DPA} and \mathbf{F}^{PIFA} are the field radiation patterns of DPA and PIFA near the laptop.

In order to capture the multipath channel parameters in high accuracy, the ODA consisting of 56 cross-polarized elements is used at Tx and Rx. All the elements are mounted in a cylinder, and the spacing between the neighboring elements is half wavelength. Figures 3(a) and 3(b) depict, respectively, the structure and antenna pattern of ODA. The collected data with this antenna array is classified as \mathbf{H}_{ODA} , and this measured data is not used as the direct data \mathbf{H}^{meas} but used to extract the channel parameters. Then $\mathbf{H}^{\text{model}}$ is obtained by channel reconstruction with these channel parameters and the corresponding antenna pattern.

2.4. Measurement System and Environment. An extensive measurement campaign is performed at center frequency of 2.35 GHz with 50 MHz effective bandwidth, using the Elektrobit PropSound channel sounder. As described in

TABLE 1: Measurement parameters setting.

Parameters	Setting
Carrier frequency	2.35 GHz
Bandwidth	50 MHz
Code length	255 (DPA, PIFA), 63 (ODA)
Tx height	2.35 m
Rx height	1 m
Tx antenna number	2 (DPA), 32 (ODA)
Rx antenna number	2 (DPA or PIFA), 56 (ODA)
Max Tx to Rx distance	30 m

TABLE 2: Angular spread.

		Tx		Rx	
		μ (°)	σ (°)	μ (°)	σ (°)
Measurement	LOS	1.58	0.21	1.77	0.15
	NLOS	1.61	0.23	1.91	0.19
M. 2135	LOS	1.60	0.18	1.62	0.22
	NLOS	1.62	0.25	1.77	0.16

detail in [13], the sounder works in a time-division multiplexing (TDM) mode. Thus periodic pseudo random binary signals are transmitted between different Tx-Rx antenna pairs in sequence. The interval within which all antenna pairs are sounded once is defined as a measurement cycle. Some important characteristics of measurement setup can be found in Table 1. Because of the bandwidth limit of the data bus and the number of antenna element, the code length of measurement system is configured as 63 when using ODAs as test antennas.

The measurement is carried out in the indoor office area. The layout of the open area is illustrated in Figure 4(a). It should be noticed that in open area, the AP indicates the position where the Tx is fixed at 2.35 m, while the Rx antenna array is fixed on the desk denoted by red dot.

2.5. Data Postprocessing. In data postprocessing, the CIRs are converted from the raw data firstly. Due to the influence of the band-pass filter in measurement system, and 10% high frequency component of baseband signal is cut during the postprocessing. So the field CIRs $\mathbf{H}_{\text{DPA}}^{\text{meas}}$ and $\mathbf{H}_{\text{PIFA}}^{\text{meas}}$ are used as the direct CIRs \mathbf{H}^{meas} . And SAGE algorithm is applied to extract channel parameters from the CIRs \mathbf{H}_{ODA} . As an extension of maximum-likelihood (ML) method, the SAGE algorithm provides a joint estimation of the parameter set $\theta_l = \{\tau_l, f_{d,f}, \Phi_l, \Omega_l, \alpha_l\}$, $l = \{1, \dots, L\}$, with no constraints on the response of antenna array. The definition of all these parameters is the same as Section 2.1. In order to capture all dominant paths that characterize the propagation environment exactly, totally 120 paths of the strongest power are extracted for each measurement cycle, namely, $L = 120$.

The angular spread in all scenarios is listed in Table 2. As shown in the table, the angular spread estimated is consistent with that from IMT-Advanced channel model in indoor scenario.

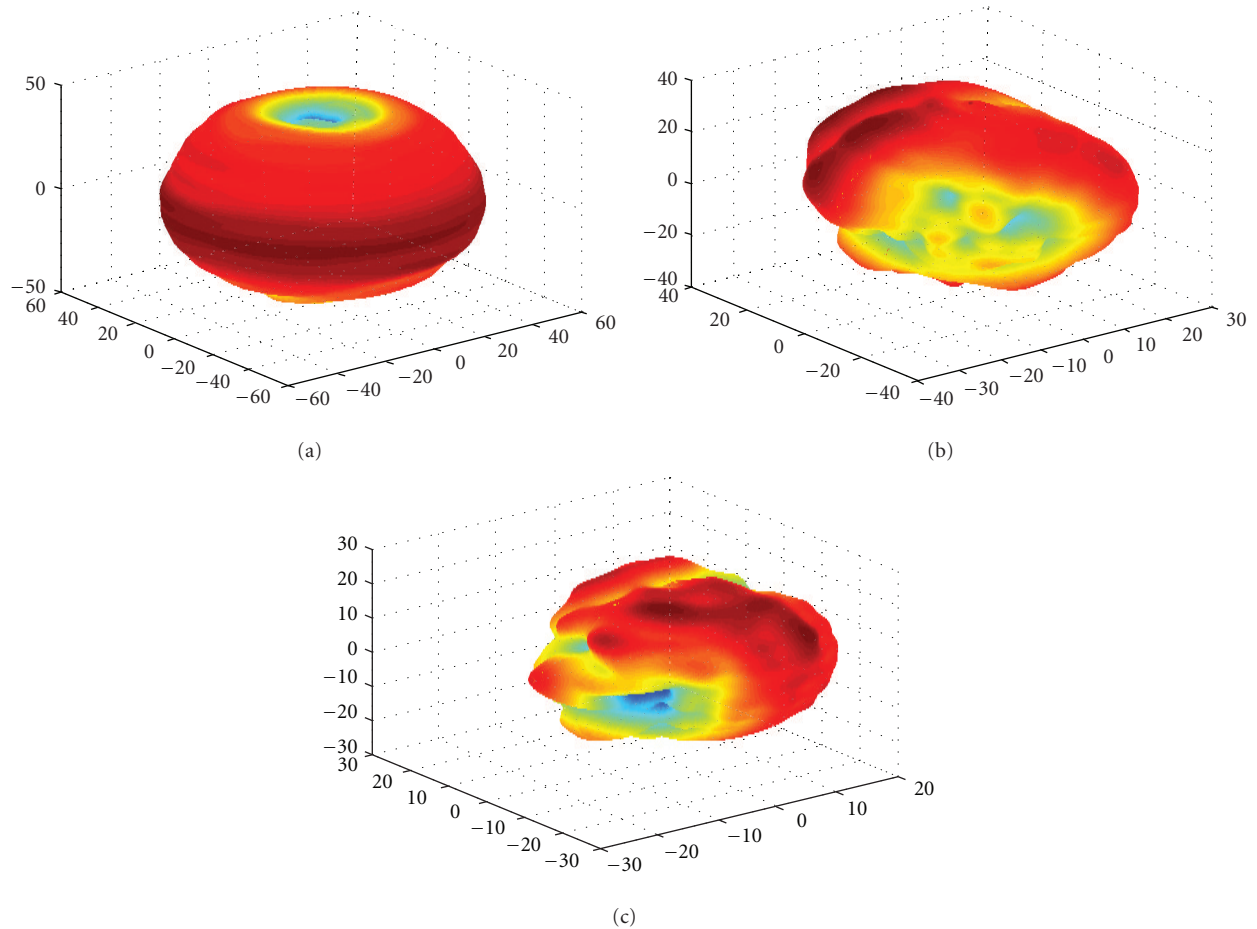


FIGURE 1: Measured far field radiation patterns for (a) dipole antenna; (b) PIFA antenna port 1; (c) PIFA antenna port 2.

2.6. Channel Reconstruction. Based on IMT-Advanced channel model with the estimated parameter set extracted from CIRs \mathbf{H}_{ODA} , the measured antenna array radiation patterns \mathbf{F}^{DPA} and \mathbf{F}^{PIFA} are incorporated into the channel model to obtain the reconstructed CIRs. The channel reconstruction follows the form as below:

$$h_{u,s}(t, \tau_n) = \begin{bmatrix} \mathbf{F}_{rx,u,V}(\Omega_l) \\ \mathbf{F}_{rx,u,H}(\Omega_l) \end{bmatrix} \begin{bmatrix} \alpha_{l,VV} & \alpha_{l,VH} \\ \alpha_{l,HV} & \alpha_{l,HH} \end{bmatrix} \begin{bmatrix} \mathbf{F}_{tx,s,V}(\Phi_l) \\ \mathbf{F}_{tx,s,H}(\Phi_l) \end{bmatrix} \times \exp(jd_u 2\pi \lambda_0^{-1} \sin(\Omega_l)) \times \exp(jd_s 2\pi \lambda_0^{-1} \sin(\Phi_l)) \times \exp(j2\pi f_{d,l} t). \quad (6)$$

The antenna pattern $\mathbf{F}_{tx,s}$ at Tx can be rewritten by \mathbf{F}^{DPA} , while the antenna patterns $\mathbf{F}_{rx,u}$ at Rx can be rewritten by \mathbf{F}^{PIFA} or \mathbf{F}^{DPA} . So the reconstructed CIRs $\mathbf{H}_{\text{model}}$ are denoted by $\mathbf{H}_{\text{PIFA}}^{\text{model}}$ and $\mathbf{H}_{\text{DPA}}^{\text{model}}$, respectively. Since there are two antenna elements at both sides of the link, $U = S = 2$ in (6).

3. Analysis and Results

To analyze the eigenvalue dispersion and capacity of the channel, the corresponding frequency transfer functions $\mathbf{H}(t, f)$ can be obtained by applying the Fourier transform to

the CIRs $\mathbf{H}(t, \tau)$. As the spectrum of the transmitted signal reveals a sinc function, signal strength is weak at band edges. Therefore, only 40 MHz in the middle of the band was used for the computation. Assuming that the $\mathbf{H}(j, k)$ is the sample of $\mathbf{H}(t, \tau)$, then

$$\mathbf{H}(j, k) = \mathbf{H}(t, f) |_{t=j \cdot \Delta t, f=k \cdot \Delta f} = \mathbf{H}(j \cdot \Delta t, k \cdot \Delta f), \quad (7)$$

where Δt and Δf are the sampling intervals in time domain and frequency domain, respectively. Before the Fourier transform, the noise level estimation should be done to reduce the affect from the additive noise on inherent characteristic of the channel [14]. And the noise level is set to -71 dB at spot 4. After denoising, about 6 delay taps are reserved for both the reconstructed data and the field measurement data. The reserved power of real CIRs accounts for 96% of the signal with noise.

Figure 5 shows the delay domain response of CIRs from field measurement data $\mathbf{H}_{\text{DPA}}^{\text{meas}}$ and the reconstructed data $\mathbf{H}_{\text{DPA}}^{\text{meas}}$ with DPAs. It is obvious that above the noise level the reconstructed data $\mathbf{H}_{\text{DPA}}^{\text{meas}}$ can well fit to the field measurement data $\mathbf{H}_{\text{DPA}}^{\text{meas}}$ in delay domain.

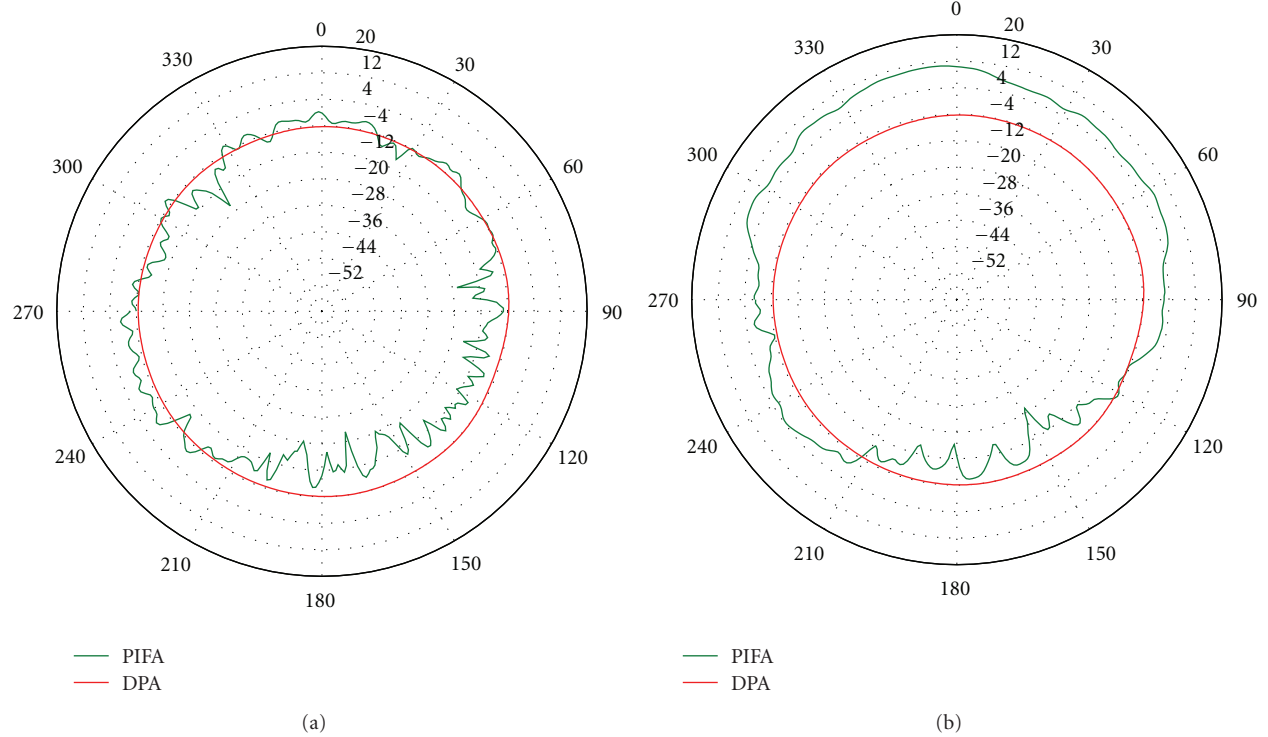
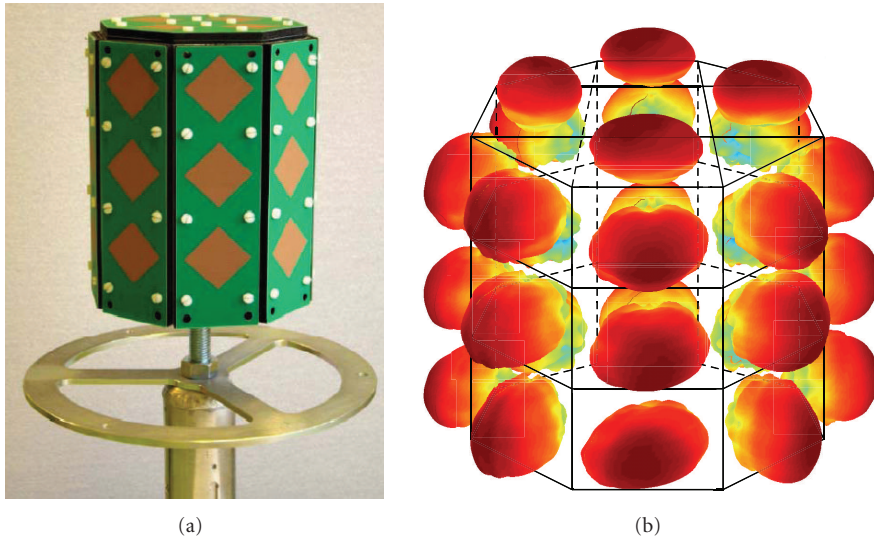
FIGURE 2: Measured radiation patterns (in dBi) on the azimuth plane (x - y) for (a) antenna port 1; (b) antenna port 2.

FIGURE 3: The configurations and antenna pattern of ODA: (a) configurations; (b) antenna pattern.

3.1. Coherent Bandwidth. Based on the CIRs from the measurement and reconstruction, the power delay profile $\beta(\tau)$ can be calculated as

$$\beta(\tau) = \frac{1}{US} \sum_{u=1}^U \sum_{s=1}^S |h_{u,s}(\tau)|^2. \quad (8)$$

Then a common normalization of the $\beta(\tau)$ is necessary for the probability density function (pdf) $\bar{\beta}(\tau)$. So the delay spread can be calculated as

$$\sigma_\tau = \sqrt{E(\tau^2) - (E(\tau))^2}, \quad (9)$$

where E is expectation operator over all channel realizations. The coherent bandwidth is defined as the bandwidth over

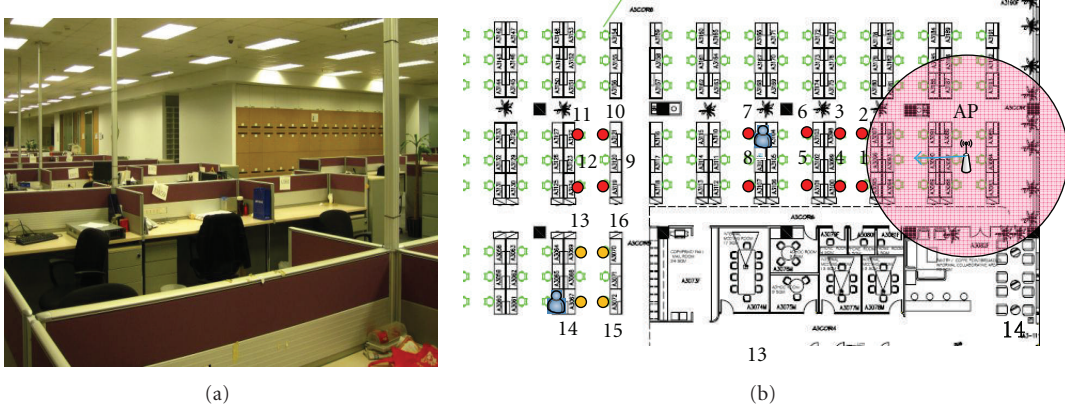


FIGURE 4: Measurement environment and route plan: (a) measurement environment; (b) route plan.

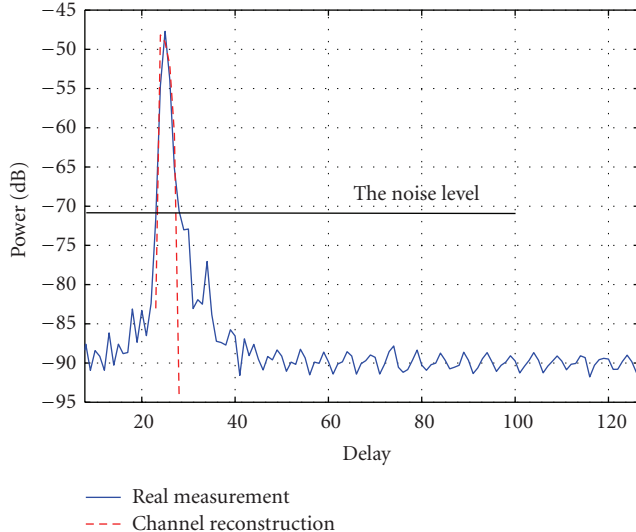


FIGURE 5: The delay domain response (in dB) of CIRs.

which the frequency correlation function is above 0.9, then the coherent bandwidth can be approximately obtained as

$$B_c \approx \frac{1}{50\sigma_\tau}. \quad (10)$$

Since 2×2 antenna configuration is applied in each test case, there are four subchannels between the transmit/receive antenna pairs in each group of CIRs. Table 3 shows the coherent bandwidth of each sub-channel (CH1~CH4) for the field CIRs \mathbf{H}^{meas} and the reconstructed CIRs $\mathbf{H}^{\text{model}}$ at spot 4. From the data of the field measurement CIRs \mathbf{H}^{meas} , the difference in coherent bandwidth between DPA and PIFA is not obvious. The small difference in coherent bandwidth of CH2 and CH4 can be attributed to the nonideal antenna patterns of PIFA on the azimuth plane as shown in Figure 2(b). For the same reason, the difference of the coherent bandwidth for reconstructed CIRs $\mathbf{H}^{\text{model}}$ is also small.

It is also shown that the coherent bandwidth of the field measurement CIRs $\mathbf{H}_{\text{DPA}}^{\text{meas}}$ and the reconstructed $\mathbf{H}_{\text{DPA}}^{\text{model}}$ are

TABLE 3: The coherent bandwidth (in MHz) of each subchannel in all cases.

		CH1	CH2	CH3	CH4
MEAS	DPA	1.67	1.07	1.24	1.13
	PIFA	1.24	0.83	1.23	0.82
MODEL	DPA	1.26	1.27	1.37	1.28
	PIFA	1.43	1.55	1.34	1.43

approximated in numerical value. So it is obvious that the reconstruction method based on the IMT-Advanced channel model with DPA will not extend or compress the width of CIRs in delay domain and will not change the statistical characteristics in frequency domain. But the reconstructed CIRs with PIFA will overestimate the coherent bandwidth, especially in CH2 and CH4. This is because different from the omnidirectional antenna gain of dipole antenna the nonideal issues on the PIFA pattern compress the width of CIRs and reduce the dispersion in delay domain. Due to the negligence of nonideal antenna pattern modeling in the IMT-Advanced channel model, the reconstructed data will impose a great impact on the system evaluation. In the real environment, the more serious intersymbol interference (ISI) will cause a degradation in the performance of MIMO-OFDM (orthogonal frequency division multiplexing) system.

3.2. Eigenvalue Dispersion. For any MIMO transfer matrix at the k th frequency bin of the j th time realization $\mathbf{H}(j, k)$, the singular value decomposition (SVD) can be obtained as

$$\begin{aligned} \mathbf{H}(j, k) &= \mathbf{U}_{\text{SVD}}(j, k) \sum(j, k) \mathbf{V}_{\text{SVD}}^H(j, k) \\ &= \sum_{r=1}^R \xi_r(j, k) u_r(j, k) v_r^H(j, k), \end{aligned} \quad (11)$$

where both the $U \times U$ matrix \mathbf{U}_{SVD} and the $S \times S$ matrix \mathbf{V}_{SVD} are unitary matrices, and is a $U \times S$ matrix of singular values σ_i of \mathbf{H} . These singular values have the property that for ξ_r is the r th largest eigenvalue of $\mathbf{H}\mathbf{H}^H$. $\xi_1(j, k) \geq \xi_2(j, k) \geq \dots \geq \xi_R(j, k)$, $1 \leq R \leq \min(U, S)$, are the ordered eigenvalues of the k th frequency bin of j th

TABLE 4: The mean value and standard deviation of eigenvalue dispersion.

		Mean	std
MEAS	DPA	0.65	0.12
	PIFA	0.77	0.12
MODEL	DPA	0.82	0.14
	PIFA	0.82	0.15

time channel realization. R is the rank of channel. The eigenvalue dispersion (ED), which is an important metric of MIMO channel, is commonly used to characterize the relative differences between the powers of eigenvalues. In this paper, we use S_{ED} as a metric of ED. The S_{ED} is defined as

$$S_{\text{ED}}(j, k) = \frac{\left(\prod_{r=1}^R \xi_r(j, k)\right)^{1/R}}{(1/R) \sum_{r=1}^R \xi_r(j, k)} \quad (12)$$

which is the ratio of geometric and arithmetic means of the eigenvalues of $\mathbf{H}\mathbf{H}^H$. S_{ED} is a useful figure of merit to characterize ED by a single number [15]. It is noted that in the case of small ED, S_{ED} tends to unity ($S_{\text{ED}} \rightarrow 1$), whereas, in the case of high ED, S_{ED} tends to zero ($S_{\text{ED}} \rightarrow 1$).

Table 4 shows the mean value and standard deviation of the eigenvalue dispersion of MIMO channel for the field CIRs \mathbf{H}^{meas} and the reconstructed CIRs $\mathbf{H}^{\text{model}}$. As shown in Table 4, for all the four cases, the mean values are, respectively, 0.65, 0.77, 0.82, and 0.82. This means that the reconstructed data has a larger S_{ED} than the real data, so the modeling method underestimates the spatial correlation of MIMO channel. And when we take the standard deviation into account, a higher value will cause a significant change in spatial correlation. Comparing the \mathbf{H}^{meas} with the CIRs $\mathbf{H}^{\text{model}}$, the reconstructed data has a larger standard deviation than the field measurement data.

Because of the coupling among the antennas in real environment, the correlation of practical antenna array will increase. However, the IMT-Advanced channel model does not take this nonideal issue into account. This antenna modeling method will make the spatial fading of the parallel channels more independently than real measurement. As the results shown above, using the data from channel reconstruction will underrate the spatial correlation in MIMO system and impose an impact on the spatial domain. In order to obtain the expected multiplexing degree from real MIMO system, the spatial resource (such as antenna spacing and polarized antenna) must be more utilized than that used in channel modeling.

3.3. Channel Capacity. The channel capacity is one of the important indicators for MIMO channel. In the absence of the channel state information at the transmitter, it is optimal to equally allocate power over all antennas. The channel capacity of frequency-selective fading MIMO channel is given by [16]

$$C(t) = \frac{1}{B} \int_B \log_2 \det \left(\mathbf{I}_U + \frac{\rho}{\beta S} \mathbf{H}(t, f) \mathbf{H}^H(t, f) \right) df, \quad (13)$$

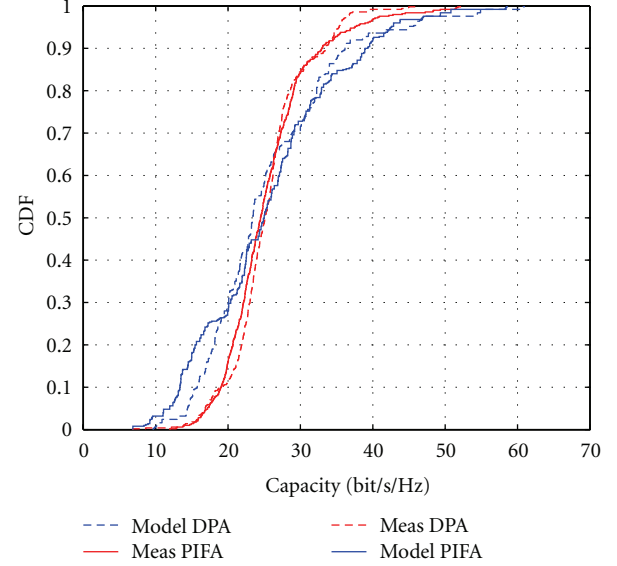


FIGURE 6: Capacity CDF at SNR 25 dB.

where ρ denotes the SNR and B is the bandwidth. For the discrete channel $H(j, k)$, an approximation can be given by

$$C(j) \approx \frac{1}{K} \sum_{k=1}^K \log_2 \det \left(\mathbf{H}_U + \frac{\rho}{\beta S} \mathbf{H}(j, k) \mathbf{H}^H(j, k) \right), \quad (14)$$

where K is the number of frequency bins of j th time realization and β is a common normalization factor for all channel realizations in such that the average channel power gain is unitary as

$$E \left\{ \frac{1}{\beta} \|\mathbf{H}(j, k)\|_F^2 \right\} = U \cdot S, \quad (15)$$

where $\|\cdot\|_F$ denotes the Frobenius norm. The CIRs between different Tx-Rx antenna array pairs are used to form the channel transfer matrix. After transforming the transfer matrix to the frequency domain, we can calculate the capacity using (14). Figure 6 shows the capacity cumulative density function (CDF) curves for all types of channel realizations.

As is shown in Figure 6, for both the field CIRs, the \mathbf{H}^{meas} has the same outage capacity as the $\mathbf{H}_{\text{DPA}}^{\text{meas}}$ and for the reconstructed CIRs, the similar result is presented. But comparing the field CIRs with the reconstructed CIRs, it is should be noted that the outage capacity CDF of $\mathbf{H}_{\text{DPA}}^{\text{meas}}$ has a smaller slope than that of $\mathbf{H}_{\text{DPA}}^{\text{model}}$. This is the reason why the field measurement data has a larger 5% channel outage capacity than the reconstructed channel data. As shown in Figure 7, the 5% channel outage capacity value of $\mathbf{H}_{\text{DPA}}^{\text{meas}}$, $\mathbf{H}_{\text{DPA}}^{\text{model}}$, $\mathbf{H}_{\text{PIFA}}^{\text{meas}}$, and $\mathbf{H}_{\text{PIFA}}^{\text{model}}$ are, respectively, 16.86, 14.62, 17.1, and 12.38. The reason is the incorrect estimation in the standard deviation of the eigenvalue dispersion. Because the standard deviation of the eigenvalue dispersion from the reconstructed CIRs $\mathbf{H}^{\text{model}}$ is larger than that from the field CIRs \mathbf{H}^{meas} , the reconstructed data has a larger slope and a higher 5% outage capacity.

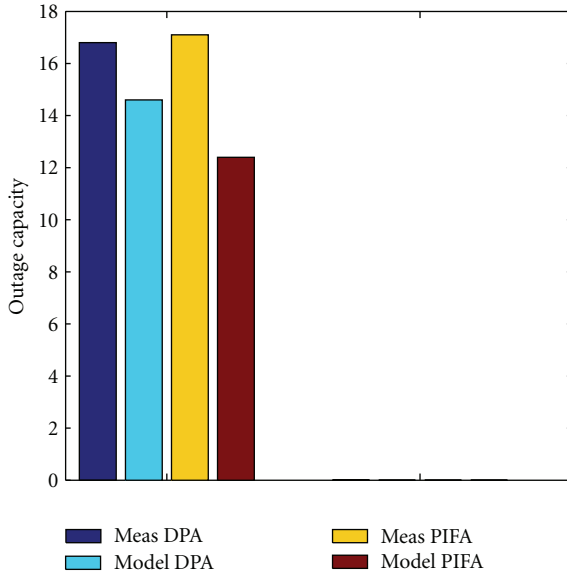


FIGURE 7: 5% outage channel capacity at SNR 25 dB at the different spots.

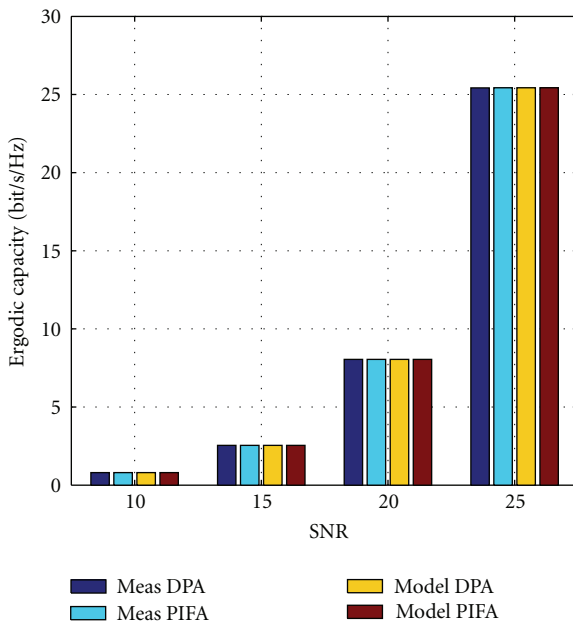


FIGURE 8: Ergodic capacity.

On the other hand, under the condition of block fading channel, the ergodic capacity is used to characterize the spatial channel capacity. Figure 8 show the ergodic capacity of MIMO channel for all four cases at spot 4. It is obvious that at each SNR all the cases have a similar ergodic capacity. Because both the \mathbf{H}^{meas} and $\mathbf{H}^{\text{model}}$ have a large S_{ED} , the spatial correlation of them is small enough to make them have a high ergodic capacity.

4. Conclusion

In this paper, the antenna pattern modeling of IMT-Advanced channel model is validated by some extensive measurement campaign at center frequency of 2.35 GHz with 50 MHz effective bandwidth in indoor environment. DPA, PIFA, and ODA are used to collect the spatial CIRs, and the channel reconstruction is performed by updating the characteristics parameters of IMT-Advanced channel model and matrix manipulation with the antenna array patterns at the both sides of the communication link. The coherent bandwidth, eigenvalue dispersion, and channel capacity are compared between the measured raw data and the reconstructed CIRs. It is found that the reconstructed data can well fit to the field measurement data in delay domain. Meanwhile, different from CIRs with DPA, the field CIRs with PIFA have a smaller coherent bandwidth than the reconstructed CIRs. A larger standard deviation of the eigenvalue dispersion makes the reconstructed CIRs have a wider range on spatial correlation than the measured raw data. So the IMT-Advanced channel model will have an influence on the channel spatial correlation estimation. On the channel capacity prediction, the wider range on spatial correlation causes the underestimation of the 5% channel outage capacity, but the four cases all have a consistent ergodic capacity at each SNR. So it is concluded that the modeling method based on IMT-Advanced channel model has a larger impact on the spatial characteristics than the frequency characteristics. Because of the nonideal issues on the antennas, the incorporation of the antenna array on the channel model should be further considered for future channel measurement and modeling.

Acknowledgments

The research is supported in part by National Natural Science Foundation of China with NO. 61171105, National Key Technology Research and Development Program of the Ministry of Science and Technology of China with NO. 2012BAF14B01, and Program for New Century Excellent Talents in University of Ministry of Education of China with NCET-11-0598, as well as funded by China Academy of Telecommunications Technology.

References

- [1] G. J. Foschini and M. J. Gans, "On limits of wireless communications in a fading environment when using multiple antennas," *Wireless Personal Communications*, vol. 6, no. 3, pp. 311–335, 1998.
- [2] E. Telatar, "Capacity of multi-antenna gaussian channels," *European Transactions on Telecommunications*, vol. 10, no. 6, pp. 585–595, 1999.
- [3] D.-S. Shiu, G. J. Foschini, M. J. Gans, and J. M. Kahn, "Fading correlation and its effect on the capacity of multielement antenna systems," *IEEE Transactions on Communications*, vol. 48, no. 3, pp. 502–513, 2000.
- [4] J. Zhang, "Review of wideband MIMO channel measurement and modeling for IMT-advanced systems," *Chinese Science Bulletin*, vol. 57, no. 19, pp. 2387–2400, 2012.

- [5] D. Chizhik, F. Rashid-Farrokhi, J. Ling, and A. Lozano, "Effect of antenna separation on the capacity of BLAST in correlated channels," *IEEE Communications Letters*, vol. 4, no. 11, pp. 337–339, 2000.
- [6] K. Yu, M. Bengtsson, B. Ottersten, D. McNamara, P. Karlsson, and M. Beach, "A wideband statistical model for NLOS indoor MIMO channels," in *Proceedings of the IEEE 55th Vehicular Technology Conference (VTC '02)*, vol. 1, pp. 370–374, May 2002.
- [7] H. Özcelik, M. Herdin, W. Weichselberger, J. Wallace, and E. Bonek, "Deficiencies of "Kronecker" MIMO radio channel model," *Electronics Letters*, vol. 39, no. 16, pp. 1209–1210, 2003.
- [8] A. M. Shirook, M. Ali, and P. Lusina, "User effects on MIMO performance: from an antenna to a link perspective," *International Journal of Antennas and Propagation*, vol. 2011, Article ID 918315, 13 pages, 2011.
- [9] *FEKO User Manual, Suite 5.4*, EM Software & Systems-S.A. (Pty), 2008.
- [10] Y. Zhang, J. Zhang, G. Liu, X. Gao, and P. Zhang, "A generic validation framework for wideband MIMO channel models," in *Proceedings of the IEEE Vehicular Technology Conference (VTC '08)*, pp. 330–334, May 2008.
- [11] *Guidelines for Evaluation of Radio Interface Technologies for IMTAdvanced*, ITU-R Std, 2008.
- [12] M. Steinbauer, A. F. Molisch, and E. Bonek, "The double-directional radio channel," *IEEE Antennas and Propagation Magazine*, vol. 43, no. 4, pp. 51–63, 2001.
- [13] *Propsound cs: The Ultimate Technology in Radio Propagation Measurement*, Elektrobit.
- [14] X. Nie, J. H. Zhang, C. Huang, Z. M. Liu, and P. Zhang, "Spatial characteristics and capacity investigation of indoor hotspot channel based on wideband MIMO measurement at 4.9 GHz," *Journal of China Universities of Posts and Telecommunications*, vol. 17, no. 3, pp. 38–44, 2010.
- [15] P. Suvikunnas, J. Salo, L. Vuokko, J. Kivinen, K. Sulonen, and P. Vainikainen, "Comparison of MIMO antenna configurations: methods and experimental results," *IEEE Transactions on Vehicular Technology*, vol. 57, no. 2, pp. 1021–1031, 2008.
- [16] A. Paulraj, R. Nabar, and D. Gor, *Introduction to Space-Time Wireless Communications*, Cambridge University Press, 2003.

Research Article

Statistical Modeling of Antenna: Urban Equipment Interactions for LTE Access Points

Xin Zeng and Alain Sibille

COMELEC Department, TELECOM ParisTech, 75013 Paris, France

Correspondence should be addressed to Xin Zeng, xin.zeng@telecom-paristech.fr

Received 6 July 2012; Accepted 7 October 2012

Academic Editor: Guangyi Liu

Copyright © 2012 X. Zeng and A. Sibille. This is an open access article distributed under the Creative Commons Attribution License, which permits unrestricted use, distribution, and reproduction in any medium, provided the original work is properly cited.

The latest standards for wireless networks such as LTE are essentially based on small cells in order to achieve a large network capacity. This applies for antennas to be deployed at street level or even within buildings. However, antennas are commonly designed, simulated, and measured in ideal conditions, which is not the real situation for most applications where antennas are often deployed in proximity to objects acting as disturbers. In this paper, three conventional wireless access point scenarios (antenna-wall, antenna-shelter, and antenna lamppost) are investigated for directional or omnidirectional antennas. The paper first addresses the definition of three performance indicators for such scenarios and secondly uses such parameters towards the statistical analysis of the interactions between the wall and the antennas.

1. Introduction

With the development of new wireless communication systems and standards, antennas of base stations or access points are more likely deployed at street level in proximity to walls and urban furniture other than the traditional antennas for GSM networks which are mounted on rooftops with few neighboring disturbers [1–3]. The effect of surrounding disturbers may be strong or weak and is very sensitive to the antenna location and antenna characteristics. Unfortunately, antennas are commonly designed, simulated, and measured in isolation from anything else as much as possible, which is not a realistic use case. For instance, the radiation pattern of a dipole mounted beside a wall is highly perturbed, indicating the severe performance degradation to omnidirectionality (see below). Unfortunately, such disturbances are highly variable and impact the behavior of antennas in an uneasily predictable manner, with significant consequences in terms of cell coverage. The latter can be quantitatively evaluated through, for example, ray tracing of even empirical propagation simulation tools, but it will be very costly to compute the propagation for many realizations of disturbed antenna characteristics. For this reason, a reasonable approach is first to develop a statistical model for the antenna radiation

behavior, before combining it with a model of simulation of the propagation. It is the goal of this paper, keeping in mind that statistical models lend themselves to the tuning of the trade-off between complexity and accuracy, depending on the number of parameters involved in the statistical distributions. For instance, [4] gives an example of this approach through radiation patterns series expansions. Actually, the evaluation of the impact of close objects on radiation is not entirely new. In [5–7], for example, the authors simulated and analyzed the antenna radiation patterns on roofs, beside walls, and on top of cars in a deterministic way. In [8–10] and many other papers, a work has been done in order to statistically evaluate the effect of, for example, a human body on antennas performance. Unfortunately and in spite of its relevance for small cells in wireless networks, little has been done regarding the interaction of antennas with walls or with urban furniture.

In the present paper, we investigate the effect of such influences on antenna radiation patterns, by using a statistical approach for their analysis. For this purpose, we first define the concept of ideal antenna sector, which can, for example, be related with the coverage area targeted by an antenna in a street. Three kinds of parameters relevant for quantifying the influence are proposed. Secondly,

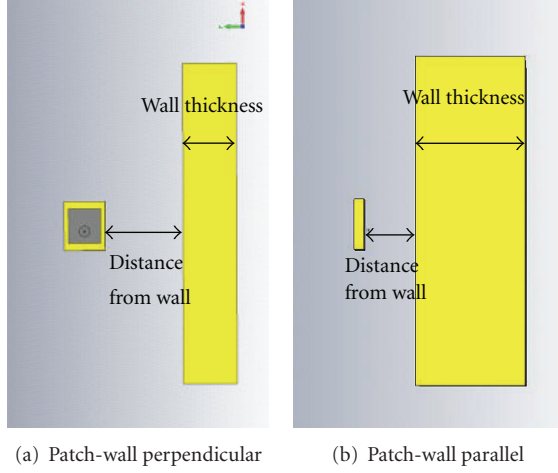


FIGURE 1: Patch antenna locations and parameters.

three antenna-disturber interaction scenarios (antenna-wall, antenna-shelter of bus stop, and antenna lamppost) are investigated. The analysis in particular seeks to check whether a normal or lognormal distribution can provide an acceptable fit to the observed distributions, for example, for power gains. All results are obtained from detailed electromagnetic simulations of the environed antennas, using both CST [11] and WIPL [12] commercial tools.

2. Sector Definition and Performance Parameters

In relation with the placement and performance of an access point antenna, the designer mostly aims at ensuring that the main beam will cover the targeted directions, conditioned by the power gain to exceed a certain level [13, 14]. This also assumes that the orientation and tilt angle will be steered adequately from just knowing the geometry of the antenna. In the present paper, we address both omnidirectional and directional antennas and we attempt to evaluate the impact brought by environmental perturbations to the radiated power, taking into account the considered “sector” (defined by azimuth and elevation widths). Ideally, a radiation sector is thus defined versus an intended use, that is, as a specification of the antenna. However, in practice, real antennas already cannot perfectly obey the specification. The deviation with respect to ideality occurs both on the beam widths and on the radiated power profile, with respect to the ideal profile (which is flat within the sector and null outside). A first aspect of antenna nonideality consequently would be to define performance criteria of an *isolated* antenna. However, this is not the purpose of the present work, whose goal is to address degradations by comparing isolated antennas. Also, from the perspective of an antenna designer, the main beam of an antenna shall include all the interested directions that perfectly match the sector requirements for an operator. For those reasons, the sector is going to be defined from the characteristics of the isolated antenna as the rectangle in angular coordinates given by the quarter power beam width of the isolated antenna (-6 dB from the maximum), in both

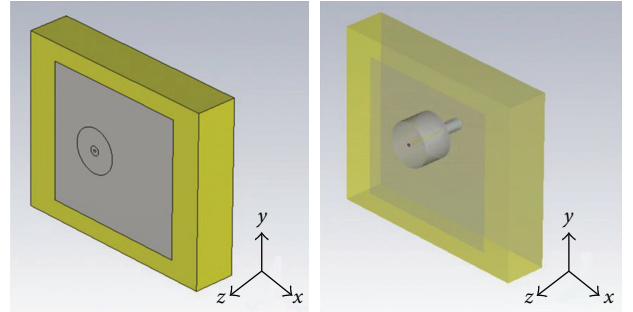


FIGURE 2: Patch antenna geometry.

E plane and H planes, completely defined by the elevation and azimuth angles θ_{\min} , θ_{\max} , ϕ_{\min} , and ϕ_{\max} . In the case of an omnidirectional antenna, only the elevation beam width needs to be defined and the parameters below are adapted accordingly.

In practice, this definition is still not fully sufficient, since the radiation pattern is frequency-dependent. Therefore, in the analysis conducted in Sections 3 and 4, a unique frequency independent antenna sector is chosen as the sector with the narrowest beam widths over the set of considered frequencies.

Given this definition of a sector, three important statistical parameters are proposed below, in order to quantify the capability of an antenna to radiate optimally into the considered sector. Beforehand, some quantities need to be defined.

SE_{ref} stands for sector efficiency as expressed in (1), where $G_{\text{ref}}(\phi, \theta)$ is the power gain of the isolated (reference) antenna along ϕ , θ azimuth and elevation angles, respectively as follows:

$$SE_{\text{ref}} = \frac{\int_{\phi_{\min}}^{\phi_{\max}} \int_{\theta_{\min}}^{\theta_{\max}} G_{\text{ref}}(\theta, \phi) d\Omega}{\int_0^{2\pi} \int_0^{\pi} G_{\text{ref}}(\theta, \phi) d\Omega}. \quad (1)$$

This quantity basically expresses that not all radiated power falls within the sector, even for the isolated antenna, owing to the fact from elementary principles that a part of the radiation necessarily leaks out of the sector.

In the expressions below, $G(\phi, \theta)$ is the power gain of the disturbed antenna. S_{sector} is the solid angle area of the sector.

The three performance parameters are as follows.

(i) The normalized “In Sector Power Gain” (ISPG) is

$$G_{\text{norm}}(\theta, \phi) = \frac{G(\theta, \phi)}{SE_{\text{ref}} \cdot TE_{\text{ref}}}, \quad (2)$$

where TE_{ref} stands for total efficiency (matching efficiency + radiation efficiency) of the isolated antenna.

(ii) The normalized “In Sector Mean Power Gain” (ISMPG) within the sector is

$$\mu_{\text{gain}} = \frac{\int_{\phi_{\min}}^{\phi_{\max}} \int_{\theta_{\min}}^{\theta_{\max}} G_{\text{norm}}(\theta, \phi) d\Omega}{S_{\text{sector}}}. \quad (3)$$

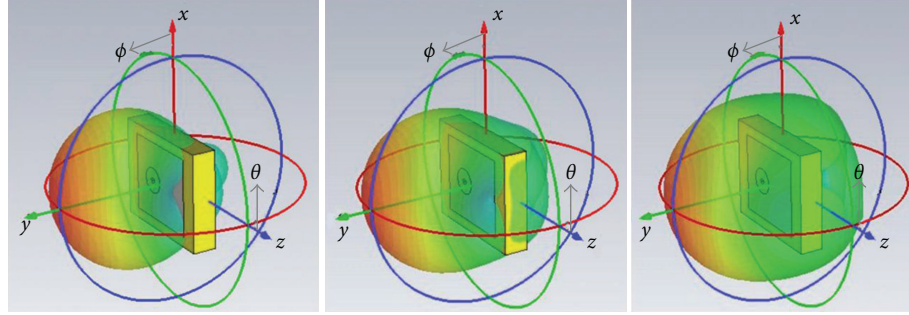


FIGURE 3: Patch antenna power radiation pattern at 1.71, 1.905 and 2.05 GHz.

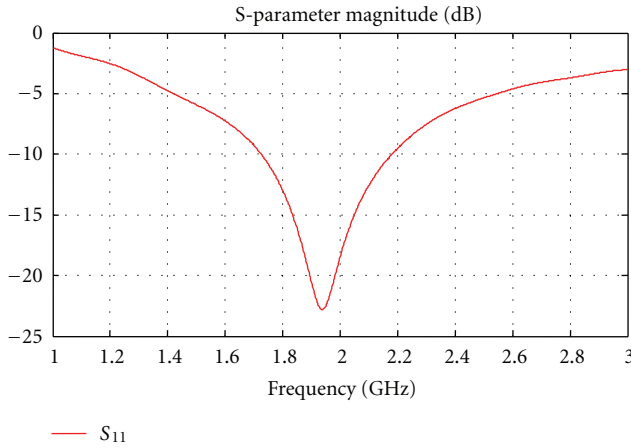


FIGURE 4: Patch antenna reflection coefficient.

$SE_{\text{ref}} \cdot TE_{\text{ref}}$ here is a normalization factor. Owing to this factor, μ_{gain} can thus be understood as the angular mean power gain over the sector, normalized by the isolated antenna sector efficiency and total efficiency. The reason for incorporating this normalization factor is that the sector efficiency and total efficiency turn out to depend on the frequency, even for the isolated antenna. By normalizing, we retain in μ_{gain} only the effects due to the disturbances rather than the non idealities of the isolated antenna.

- (iii) The “In Sector Standard Deviation of the Power Gain” (ISSDPG) within the sector is

$$\sigma_{\text{gain}} = \sqrt{\frac{\int_{\phi_{\min}}^{\phi_{\max}} \int_{\theta_{\min}}^{\theta_{\max}} (G_{\text{norm}}(\theta, \phi) - \mu_{\text{gain}})^2 d\Omega}{S_{\text{sector}}}}. \quad (4)$$

Basically, these 3 parameters tell us if the radiated power is constant and sufficiently high within the sector, with respect to the isolated antenna. ISPG contains all values of the radiated power in all directions within the sector, thus it provides us with very detailed information about the antenna radiation characteristic. ISMPG tells us what is in average, the gain of the antenna within the sector, and whether it is higher than that of an isolated antenna. ISSDPG tells up to what extent the gain deviates from this mean value, in other words whether the radiation pattern is flat or varying within

TABLE 1: Parameters of patch-wall scenarios.

	1.71	1.905	2.05
Frequency (GHz)			
Permittivity of wall	3	4	5
Distance between patch (edge) and wall (mm)	50	100	150
Wall thickness (mm)	100	150	200

the sector. The cumulative distribution function (CDF) of these three parameters provides us with an indication on the gross characteristics of the variability of radiation patterns and they will be shown in the following sections.

3. Antenna in Proximity to a Wall

In this section, we consider the practically important case of an antenna placed on a wall.

3.1. Analysis of Directional Antenna-Wall Interaction. In the first part of this section, two patch-wall configurations are considered (Figure 1).

In order to simulate a real scenario, we designed an air patch antenna operating from 1.7 GHz to 2.1 GHz in proximity to a wall, whose characteristics are shown in Figures 2–4. Given that the power radiation pattern is getting narrower at low frequency, the sector at 1.7 GHz is selected to cover the angles $\phi = [30^\circ - 150^\circ]$, $\theta = [55^\circ - 150^\circ]$ in degrees according to the definition in Section 2. This patch antenna is a directional antenna, which may be deployed in two configurations: one is parallel to a wall in order to cover the area along a street; the other is perpendicular to a wall in order to cover a wide area, a street crossing, a square, and so forth.

The patch location and the wall parameters are shown in Figure 1 and in Table 1, respectively. The frequency points of the simulation are selected from 1.7 GHz to 2.1 GHz as one of the potential LTE bands. The permittivity of the wall has been chosen to vary from 3 to 5, according to common building material parameters [15]. The other parameters are determined based on typical building structure and the experience of antenna deployment provided by an antenna commercial company. There are 81 realizations for each configuration and all electromagnetic simulations have all

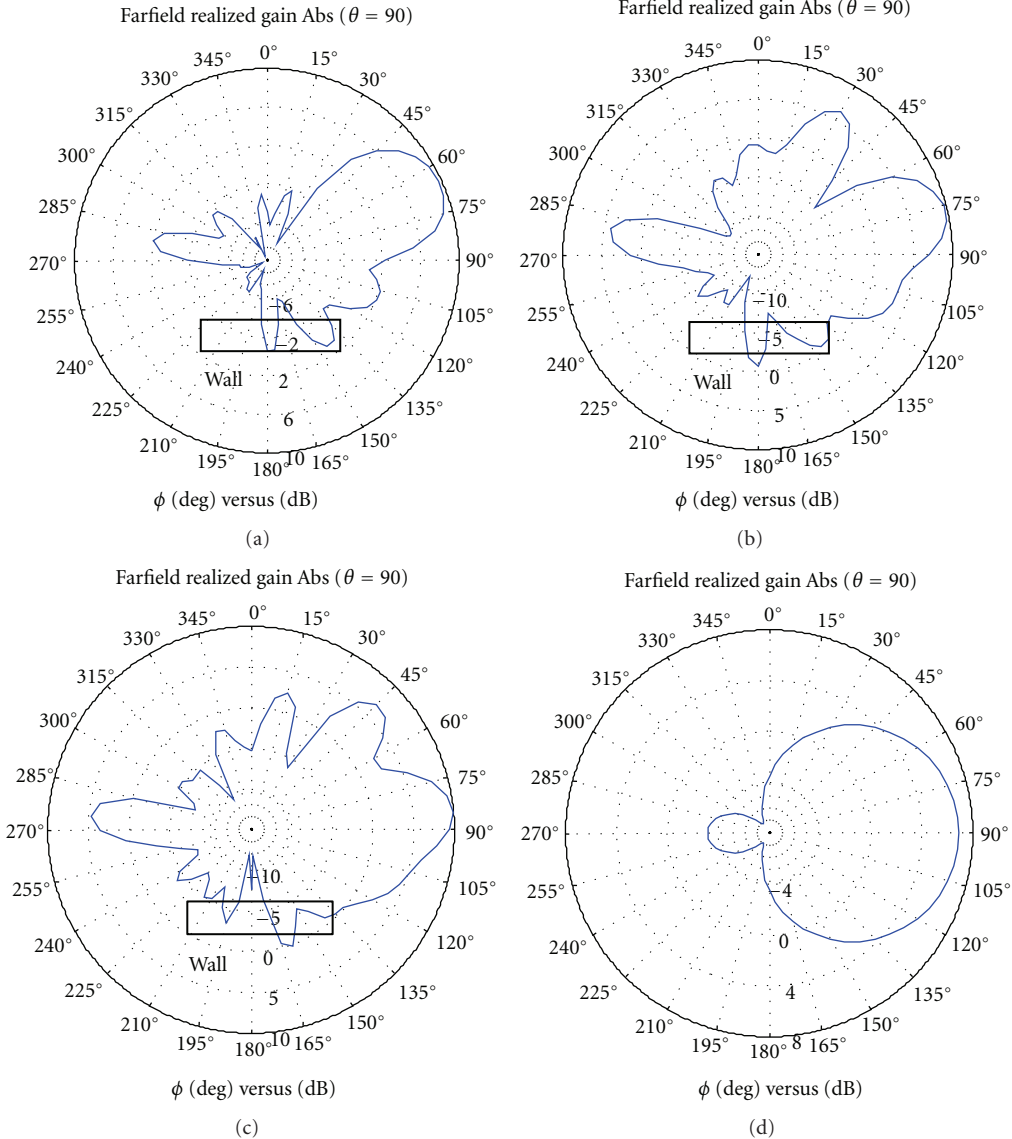


FIGURE 5: Power gain in azimuth in the perpendicular case (a)–(c) Wall distance 50 mm, 100 mm, and 150 mm; (d) isolated antenna (1.7 GHz).

been carried out using CST. In the simulations, neither the antenna nor the materials are lossy. Thus, the considered effects are solely related to the impedance mismatch or (mainly) to the degradation of the radiation pattern shape.

Figures 5 and 6 reveal the serious impact of the wall on the patch antenna radiation patterns in both cases, even in the parallel case, which is not so intuitive since commonly it is assumed that the back radiation has little influence on the main beam. It can be found in Figure 5 that the main beam direction is driven away from the wall when the antenna-wall distance decreases. This phenomenon is obvious because the lower half of the original main lobe experiences a wall reflection and sums up with the other half. The smaller the distance, the more power is reflected by the wall and the larger the reflection angles. In order to represent the main beam direction and to know how it is affected by this effect, we use the mean radiation direction (MRD) proposed

by Fleury [16], which is more stable than maximum gain direction. The MRD is based on the following vector:

$$\mu_\Omega = \oint e(\phi, \theta) G(\phi, \theta) d\Omega, \quad (5)$$

where $e(\phi, \theta) = [\cos(\phi) \sin(\theta), \sin(\phi) \sin(\theta), \cos(\theta)]^T$. From this mean vector, we can extract the MRD as the direction of μ_Ω .

Figure 7 highlights the distribution of the mean azimuth angle ϕ_{mean} over the set of realizations. Notice that the difference of MRD between the disturbed antenna and the isolated antenna is up to 32 degrees and varies inversely with the distance from wall. As opposed to the perpendicular case, the parallel case is almost symmetrical, thus the mean direction does not change significantly as compared to the isolated antenna, see Figure 6.

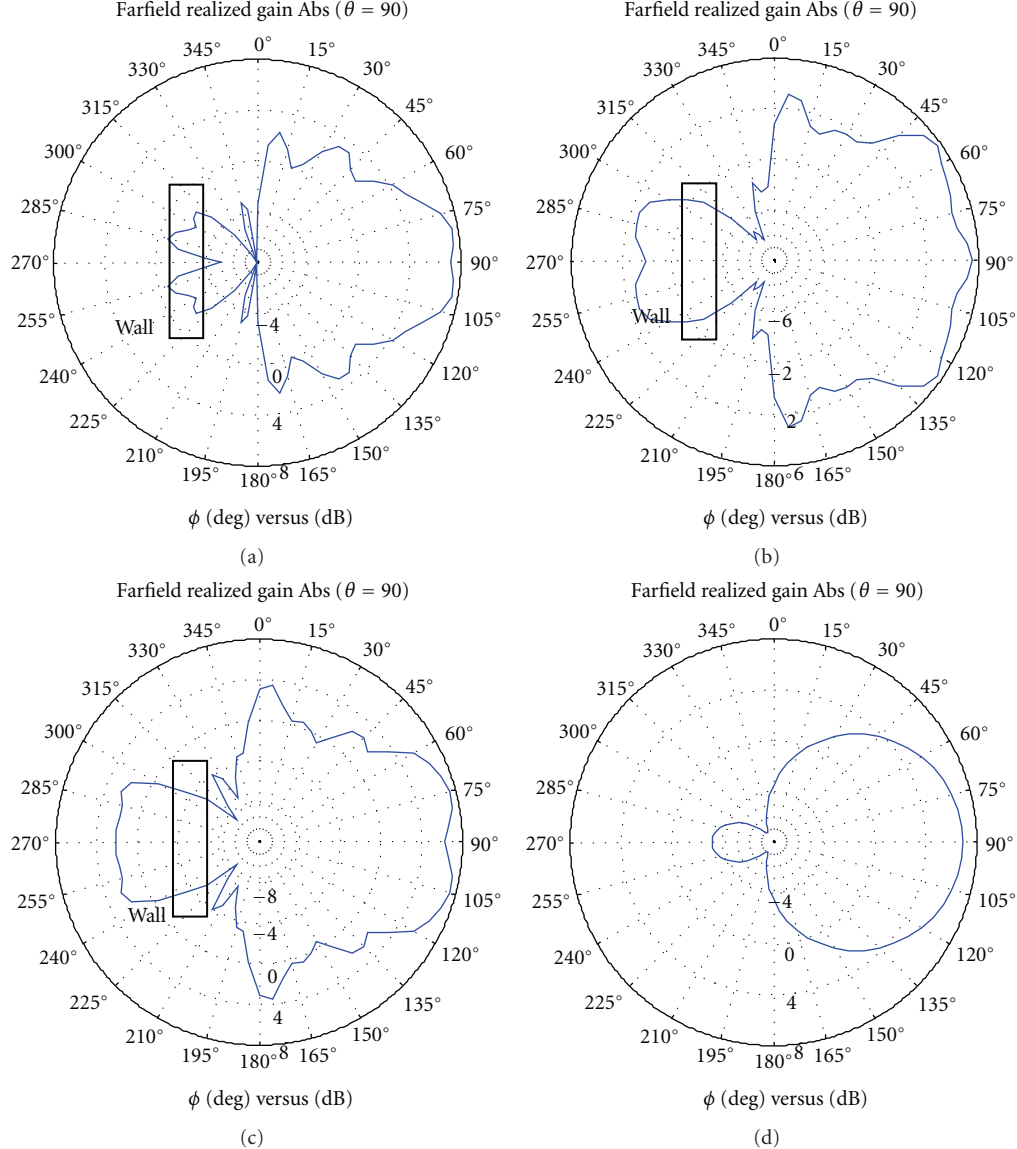


FIGURE 6: Power gain in azimuth in the parallel case. (a)–(c): wall distance 50 mm, 100 mm, and 150 mm; (d) isolated antenna (1.9 GHz).

Figures 8 and 9 show the aggregated ISPG distribution for the two cases, at each frequency and with all frequencies altogether. Owing to the total and sector efficiencies normalization, the main frequency dependence is removed and the statistics are better combined. The Gaussian best-fit distribution is plotted for comparison. Notice that in Figure 6, several nulls can be seen, which is due partly to the blocking of the radiation into the directions penetrating the wall, and partly to severe destructive interference as the result of reflections at the first and second interface of the wall, leading to the long tail in Figure 8 of low gain values. This effect will be more clearly seen in the omnidirectional antenna case. In other examples of antenna-disturber interactions, such tails have been analyzed in terms of general extreme value distribution or of a Gaussian mixture distribution [9, 10].

Figure 10 shows the ISMPG for the former scenario. As expected, because the main lobe of patch is parallel

to the wall and due to strong wave reflections out of the sector, the average gain within the sector is less than the isolated antenna. Notice that the shorter the distance from wall, the larger the portion of power reflected from wall to outside of the sector, which leads to less average gain as shown below. However, in the latter case, it is difficult to find a regular distribution of the average gain (Figure 11). While wall reflection should increase power within the sector, destructive interference (e.g., at 1.71 GHz) sometimes actually attenuates the gain in the sector.

Figure 13 shows the cumulative distribution of ISSDPG for the perpendicular scenario and Figure 14 shows the same parameter for the parallel scenario. Results from the three frequencies were combined in these two figures in order to construct a global statistical distribution. The deviation of the gain around the mean ranges from 2.7 dB to 5.9 dB in Figure 12 and from 1.6 dB to 3 dB in Figure 13. We observe that the Gaussian distribution fits the curves well, with the

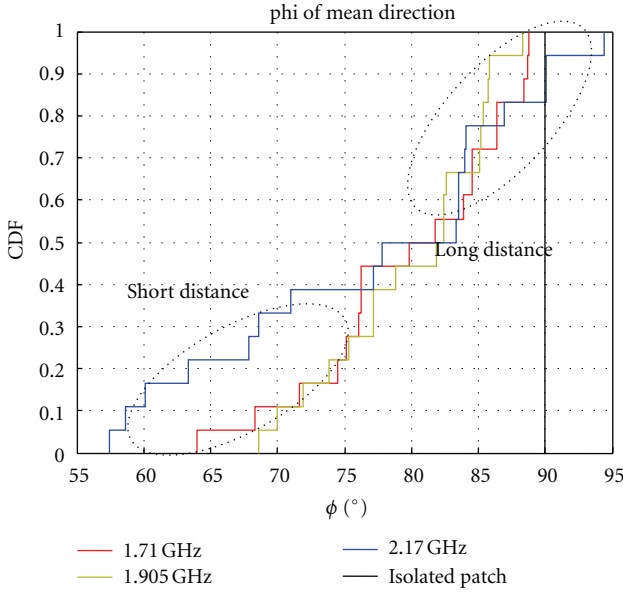


FIGURE 7: Distribution of the azimuth angle of the MRD for the patch-wall perpendicular case.

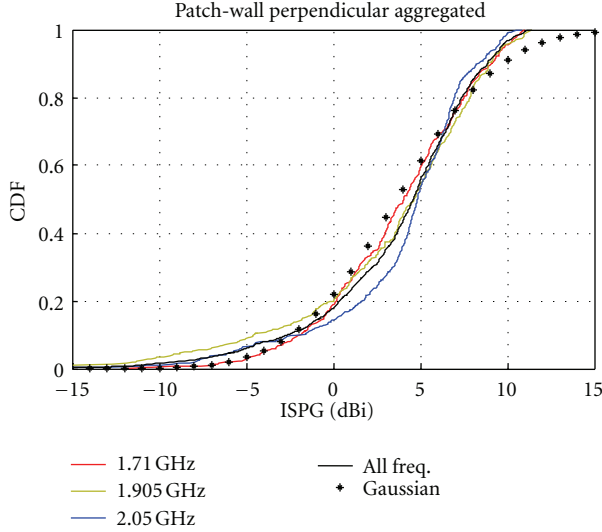


FIGURE 8: Distribution of ISPG for the perpendicular patch-wall case.

average and standard deviation (μ, σ) of (4.12, 0.84) dB for the first scenario and (2.26, 0.29) dB for the second scenario. The average of the Gaussian distribution in the first scenario is larger than that in the second one because when the patch is perpendicular to a wall, the wall reflects the radiated power from the lower half of the sector into the upper half, weakening the former and enhancing the latter. This leads to a large difference between the lower and upper halves of the pattern.

3.2. Analysis of Omnidirectional Antenna-Wall Interaction. For the second set of simulations, we considered a dipole vertical array, with a metallic supporting post attached to a wall as shown in Figure 14, again operating within the same

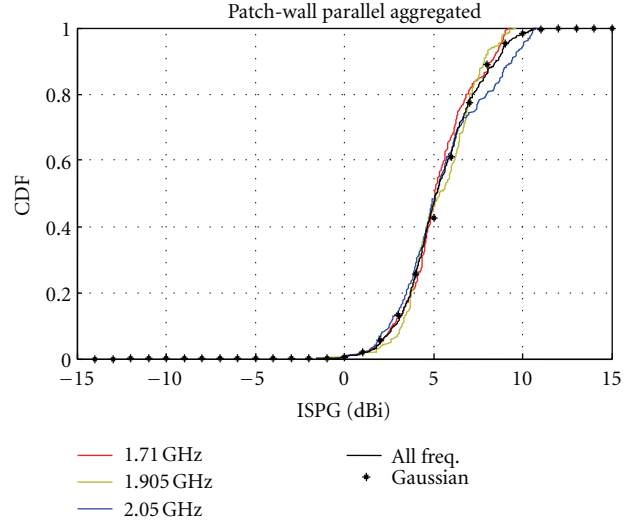


FIGURE 9: Distribution of ISPG for the parallel patch-wall case.

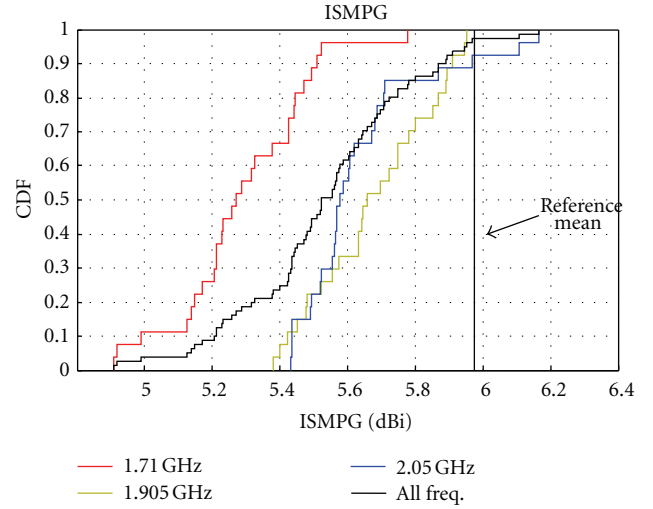


FIGURE 10: ISMPG distribution over all realizations for the patch-wall perpendicular scenario.

TABLE 2: Parameters of dipole-wall scenarios.

Frequency (GHz)	1.71	1.905	2.05
Permittivity of wall	3	4	5
Distance between patch (edge) and wall (mm)	100	200	300
Wall thickness (mm)	100	150	200

bandwidth in order to compare with the directional antennas case. The simulation parameters are listed in Table 2, again providing 27 realizations at 3 frequencies. Since the radiation pattern of the dipole array is omnidirectional on the azimuth plane, the sector for the dipole array only restricts the elevation angle ($\theta = [65, 115]$) according to its -6 dB beam width.

Firstly, the azimuth pattern and distribution of ISPG are presented in Figures 15 and 16. The long tails of the

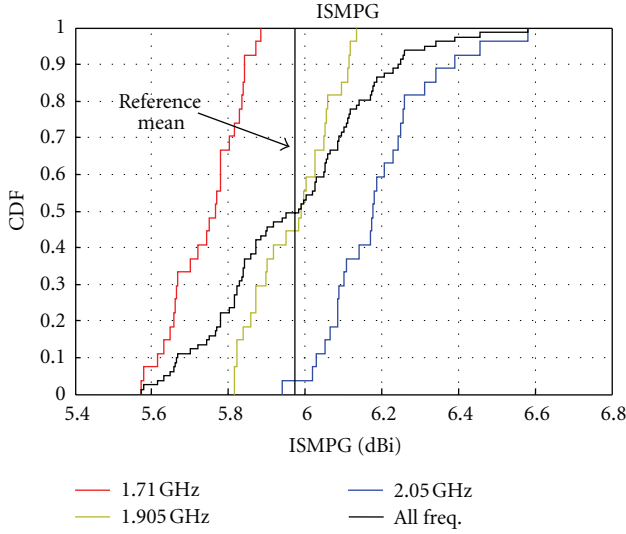


FIGURE 11: ISMPG distribution over all realizations for the patch-wall parallel scenario.

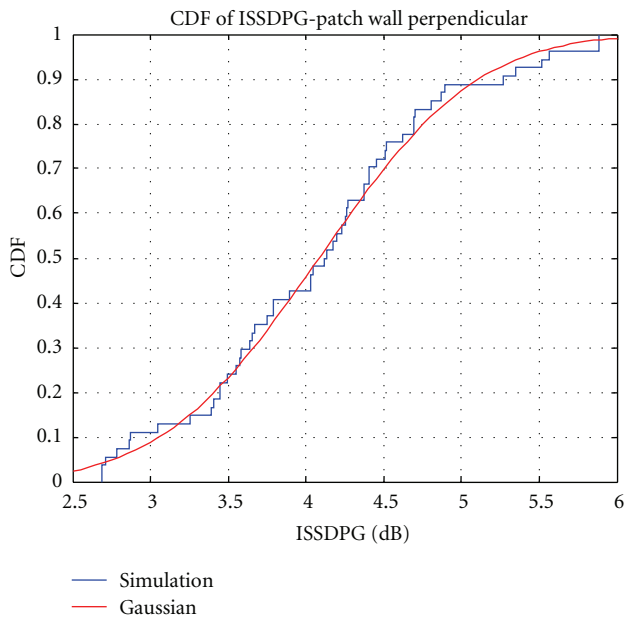


FIGURE 12: ISSDPG distribution for the patch-wall perpendicular case.

CDF, which are similar to the patch-wall scenario, are due to several radiation pattern nulls, as revealed in Figure 15. Some of the waves radiated towards the wall reflect on its near surface while some penetrate the wall and reflect on the second interface. These two reflections, together with the direct waves, cause constructive and destructive interference and form irregular patterns. Secondly, even though the wall disturbs the radiation patterns dramatically, most of the power radiates around the azimuth plane, not only resulting in unchanged average gain in the sector (not shown here) but also resulting in a large deviation around the mean. Figure 17 shows the CDF of ISSDPG at all frequencies, revealing that a normal distribution again fits the data quite well. The

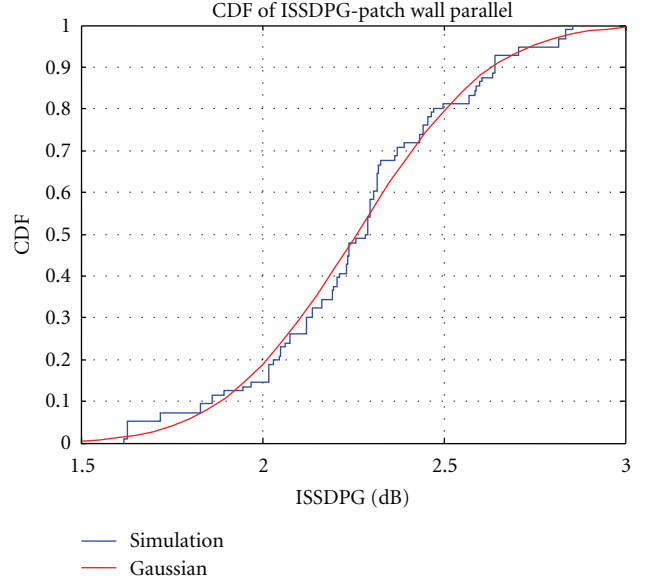


FIGURE 13: ISSDPG distribution for the patch-wall parallel case.

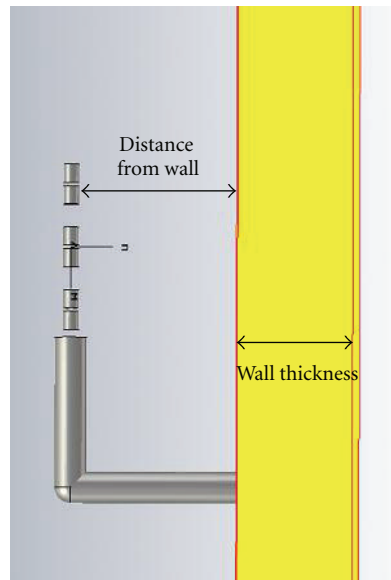


FIGURE 14: Dipole array locations and parameters.

parameters of the fitted Gaussian distribution are $(\mu, \sigma) = (4.08, 0.29)$ dB, which tells us that the standard deviation of gain in each pattern is not heavily dependent on the particular realization. A large ISSDPG means that the gain values within the considered sector are deeply disturbed and do not behave so nicely omnidirectionally as for the isolated antenna, therefore the antenna performance is degraded.

4. Antenna Deployment on Urban Furniture

Among the deployment schemes considered for 4 G wireless networks, small cells and femtocells as well as relays are the most widely advocated. This implies bringing antennas very close to the users and as much invisible as possible. Then the

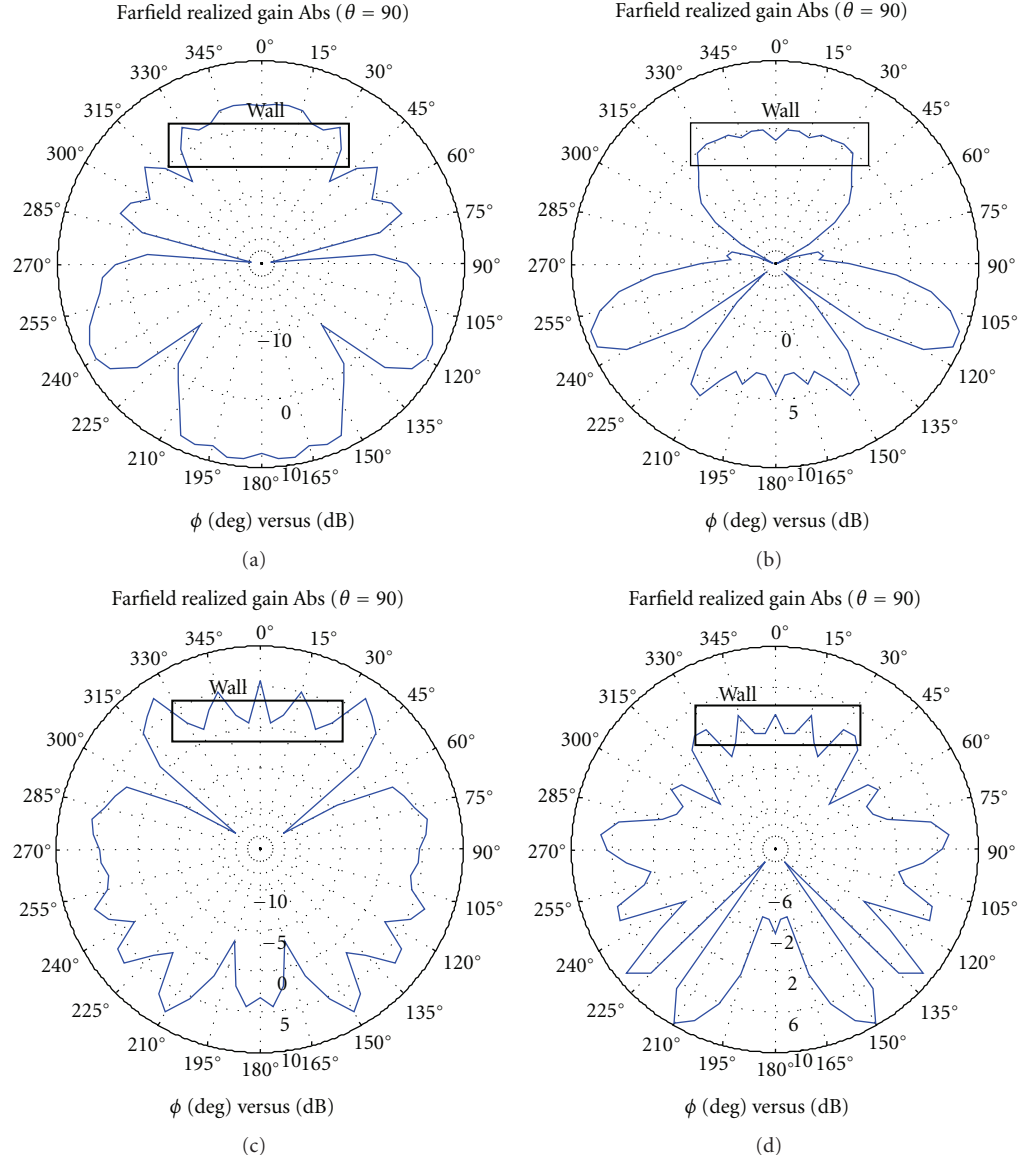


FIGURE 15: Examples of power gains in the azimuth plane for four realizations.

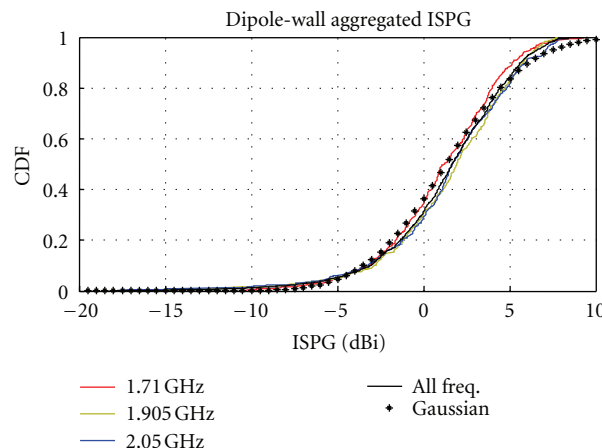


FIGURE 16: ISPG distribution for these two examples.

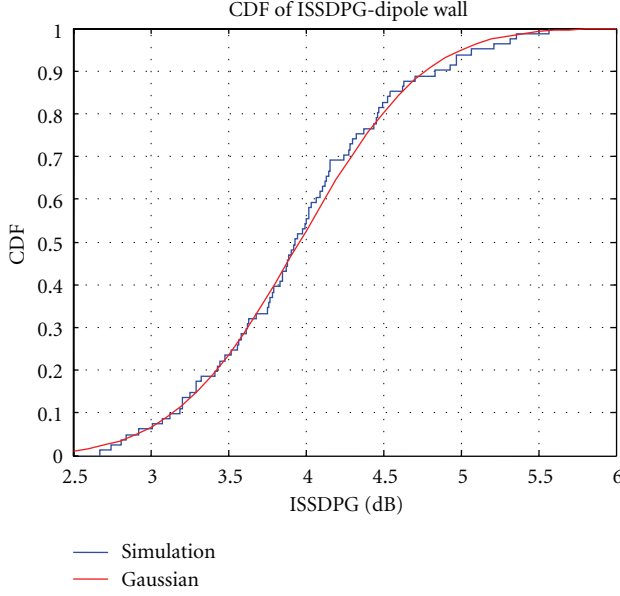


FIGURE 17: ISSDPG distribution for the dipole-wall scenario.

integration of the antennas into urban furniture is a serious option. Indeed, such equipments are very common in all modern cities, being part of transportation or other public services and it will likely be possible to contract with servicing companies for installing and maintaining 4 G networks antennas. In addition, these pieces of equipment are often connected; however, as indicated above, urban furniture may cause a strong degradation of antenna performance, resulting in uncontrolled changes of the radiation patterns. In order to investigate this quantitatively, two scenarios are considered here, one being an omnidirectional antenna settled on a bus-stop shelter with a dielectric roof, see Figure 18, and a directional antenna attached to a lamppost (Figure 23).

These designs have been inspired by a real bus shelter and real lamp posts.

4.1. Analysis of Omnidirectional Antenna-Shelter Interaction. In this part, the simulated antenna is an ultra-wideband (UWB) bicone, designed to operate from 200 MHz to 3 GHz in Figure 19.

As opposed to the above cases, where the considered frequencies only ranged from ~ 1.7 to 2.1 GHz, this scenario considers a much broader band from 200 to 3000 MHz. The reason stems from the large variation of frequency bands contemplated for LTE, in some cases going down to 400 MHz (e.g., for private mobile radio applications used by civil security services, police forces, etc.).

The other parameters are

- (1) frequency points: 200 to 3000 MHz every 200 MHz;
- (2) permittivity of plastic roof: 3;
- (3) size of roof (mm): $1800 * 810 * 3.6$.

The UWB antenna was assumed to be located on top of a bus-stop roof, according to a uniform spatial distribution. In practice, the antenna locations are distributed over

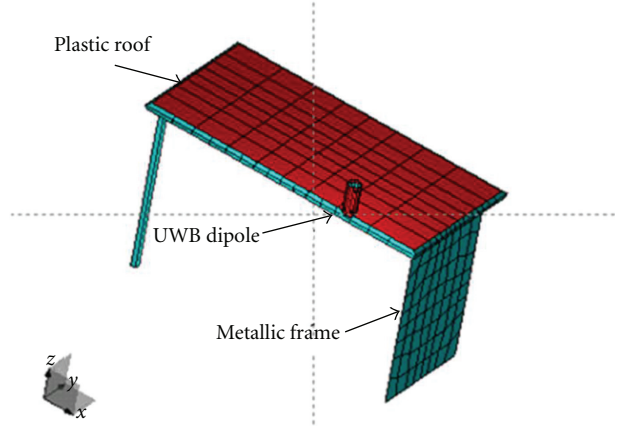


FIGURE 18: Antenna-urban equipment scenarios.

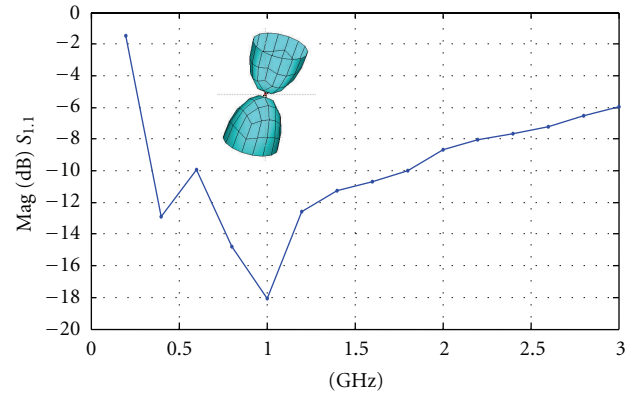


FIGURE 19: Design and reflection coefficient of an ultra-wideband omnidirectional radiator.

a rectangular grid, of increment 450 mm in length and 202.5 mm in width. This resulted in 25 antenna locations for each frequency point. All simulations were carried out using WIPL-D.

Owing to the UWB antenna's nearly perfect rotational symmetry, the isolated antenna pattern is extremely omnidirectional. It is also quite broad in elevation, although starting from ~ 1.2 GHz onward, it starts being multimode, which translates into a structured shape in elevation. This phenomenon is responsible for a slightly lower gain in the horizontal plane at these frequencies.

In the previous section, the statistical parameters at different frequencies have been aggregated together. However, in this section, the statistical parameters will be shown in individual frequency points in order to fully reveal a possible regular variation with frequency. Besides, since the "sector" means the solid angle area in which we are interested or where the antenna intends to radiate, the range of the sector has been adjusted in order to observe the variation of the ISPG. The sector is found to cover the angles $\phi = (0-360)$, and $\theta = (35-145)$ in degrees, so we will show results with sector $\phi = (0-360)$, and $\theta = (35 (\pm 10) \sim 145 (\pm 10))$.

The left column of Figure 20 exhibits the ISPG distributions for the antenna-shelter scenario at each frequency,

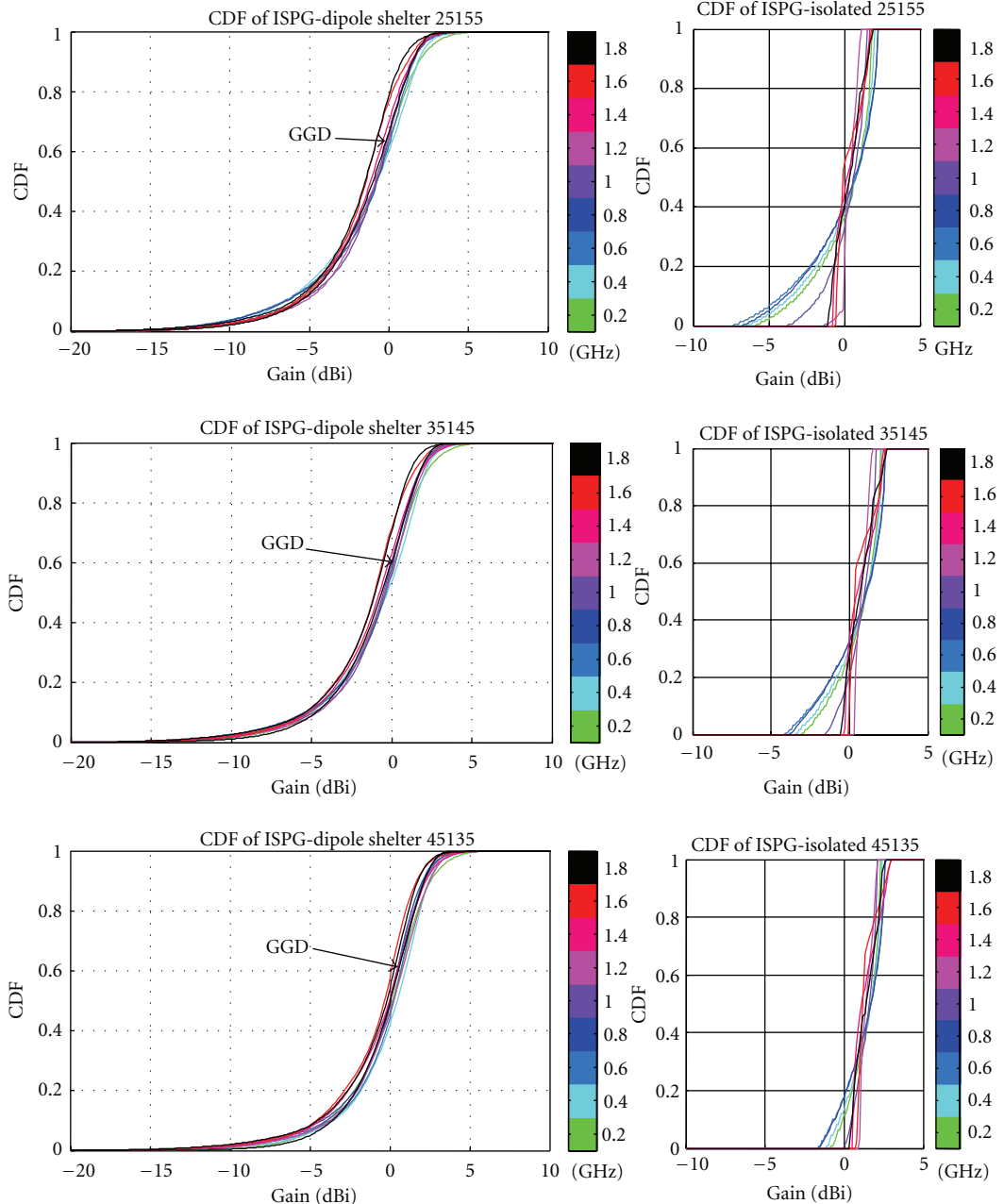


FIGURE 20: ISPG distribution for antenna-shelter and various sector widths in elevation: (25–155°), (35–145°), and (45–135°) (from top to bottom).

while the right column shows the corresponding ISPG distributions for the isolated antenna. Naturally in that case, the distribution is very narrow and only stems from the shape of the radiation pattern, which is not isotropic. In Figure 20, three values for the sector elevation beamwidth have been chosen (130°, 110°, and 90° from top to bottom) in order to test the robustness of the distributions to this parameter.

With the normalization of TE and SE, the curves at different frequencies are much closer and easier to compare. By looking at the isolated antenna ISPG plots, we see that the low gain tail is shorter when the sector gets narrower, especially for the low frequencies (green curves). This is

because in a broader sector, more low power gain values originating from high angles in the radiation patterns are involved at low frequencies. A high frequency often means a broad beamwidth. Even though the first sector is the broadest, it still cannot catch many low power values of the gain. Thus, for high frequencies, the radiation patterns change less with the restriction of the sector.

The ISPG distributions for the disturbed antenna case, in contrast, vary less when the size of the sector decreases, which also proves the robustness of the selection of the sector. Since the distribution of ISPG is naturally asymmetrical due to the fact that the power gain can be extremely low

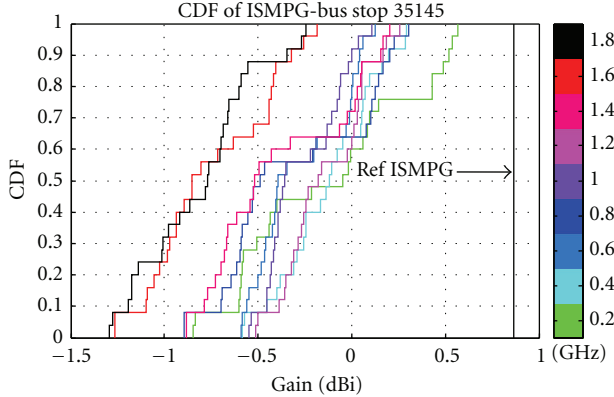


FIGURE 21: ISMPG distribution for antenna-shelter (standard sector).

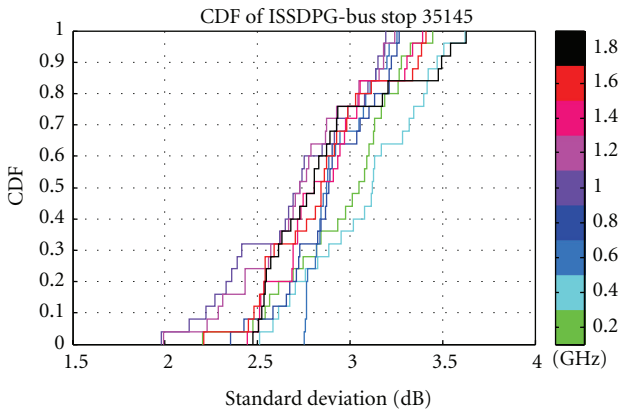


FIGURE 22: ISSDPG distribution for antenna-shelter (standard sector).

(nulls) but cannot be extremely high, Gaussian distribution is not suitable for this case, even though it performs well in previous scenarios. Generalized Gaussian distribution (GGD), whose shape parameter can be used to introduce skew, has been proposed to fit the ISPG distribution. After the normalization, the curves are found to follow the generalized Gaussian distribution far better than the Gaussian distribution. The goodness of fit will be studied in a future work.

Figure 21 reveals a negative impact by the dielectric roof, where the UWB dipole at all frequencies performs a little worse than the isolated antenna. With the increase of frequency, the ISMPG deviates from the reference with a difference up to 2.3 dB. A high frequency generally translates into a more severe degradation than a low frequency. From the perspective of radiation main lobes orientation, the roof does not block radiations downward, thus signal detection for users below the roof is still achievable. The ISSDPG distributions are shown in Figure 22, revealing that the metallic frame largely increases the variance of the ISSDPG. The average value and difference of ISSDPG at one frequency is more than 2.5 dB and 1 dB, respectively. The metallic frame creates constructive and destructive interference by its strong reflections, increasing ISSDPG and weakening the stability of radiation within the sector.

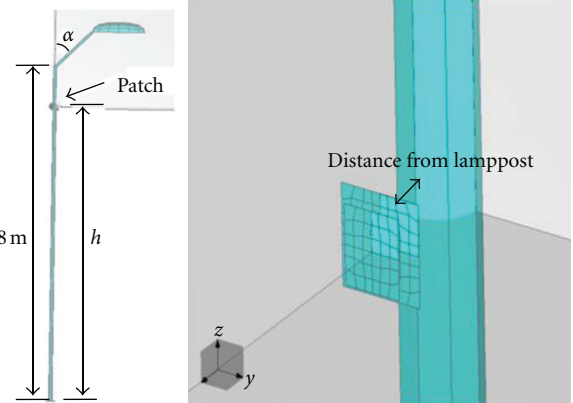


FIGURE 23: Antenna and lamppost location.

TABLE 3: Parameters of dipole-wall scenarios.

Frequency (GHz)	1.7	1.9	2.1
Antenna height (mm)	7000	7400	7800
Angle of corner ($^{\circ}$)	45	60	90
Distance from lamppost (mm)	20	50	

4.2. Analysis of Directional Antenna Lamppost Interaction. In order to simulate the scenario where a directional antenna is deployed on a lamp post, a simulation environment has been established as shown in Figure 23. Similar to the directional antenna-wall scenario, there are 3 kinds of input parameters (listed in Table 3), where the material of the lamp post is taken to be a PEC (perfect electric conductor). The variation of parameters represents the possible position and possible type of lamp post on which the LTE access point will be deployed.

As shown in Figure 24, because of the reflection of radiated waves by the metallic lamp post, the beam width becomes narrower whatever the frequency is. In contrast to the isolated antenna, the main beam of the disturbed antenna at 2.1 GHz is almost allocated in the sector, leading to a high ISPG after normalization, which implies high sector efficiency improvement at 2.1 GHz under disturbance. This effect can be seen easily in the CDF of the ISPG (Figure 25).

For isolated antenna, the sector efficiency at 2.1 GHz is 0.36, meaning a low normalization factor. But for disturbed antenna, the main beams at three frequency points are all focused in the sector. In other words, the sector efficiency has been highly improved especially at 2.1 GHz, than divided by a low normalization factor. Thus it interprets why ISPG at 2.1 GHz is larger than the reference (isolated) antenna. Meanwhile, one can observe that the ISPG at 1.7 GHz is smaller than the reference because the interaction with lamp post raises antenna's input return loss ($S_{11} = -3.69$ dB). Such an unfavorable return loss impairs and weakens the radiated power in the sector, leading to low ISPG.

A fitted generalized Gaussian distribution curve has been plotted, for comparison with the aggregated ISPG CDF curve. However, the curves for individual frequencies are too far away from each other, only modeling the aggregated curve

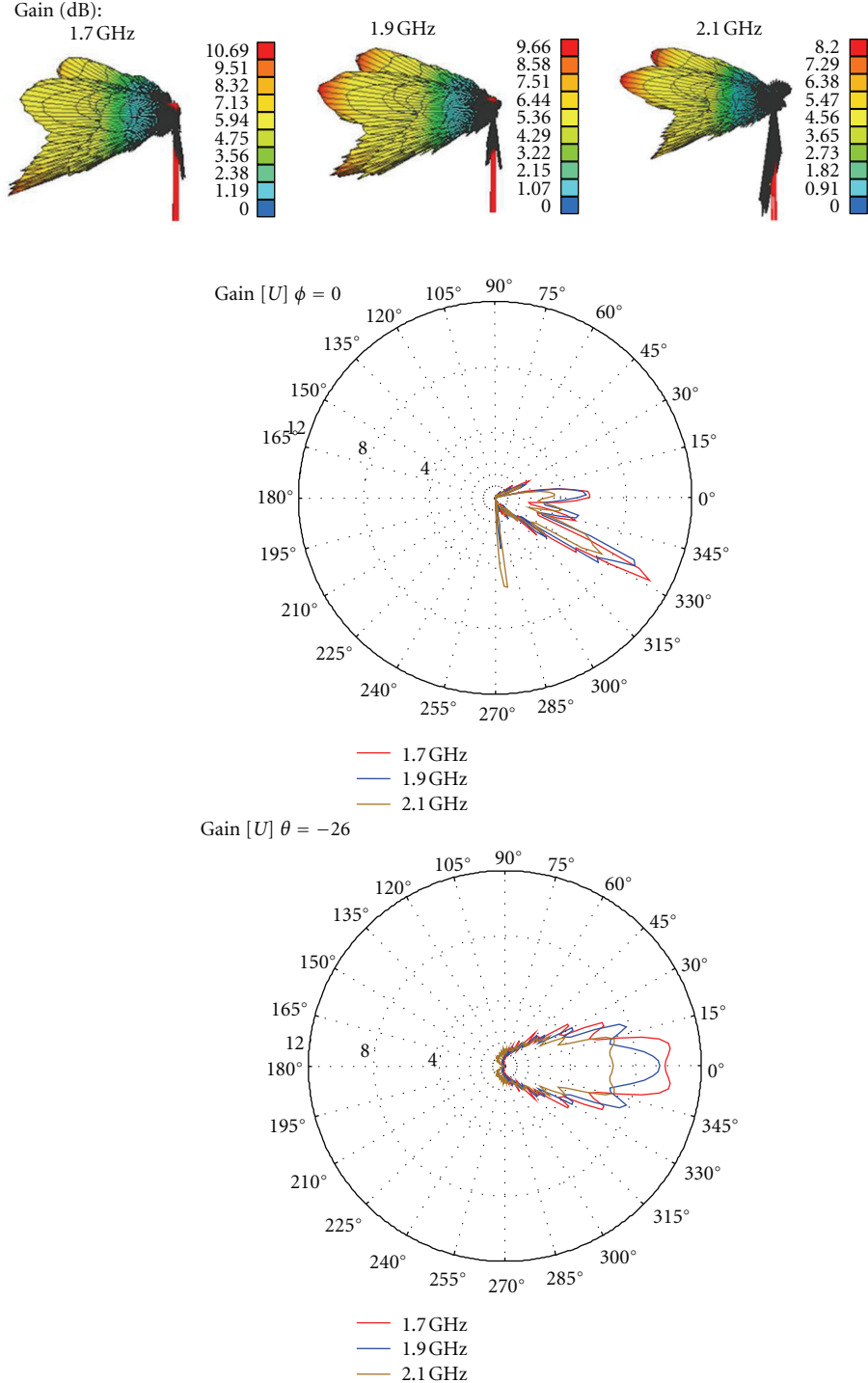


FIGURE 24: Radiation patterns for one realization in the lamppost scenario.

is not sufficient to find frequency-specific distribution while the ISMPG and ISSDPG at individual frequency are also very important to be modeled. The ISMPG (Figure 26) for three frequencies with very small variations is distributed around the reference ISMPG as expected. This means that the sector efficiency or the portion of power radiated within the desired direction at 1.9 and 2.1 GHz is much better than the isolated antenna, and this quality does not change too much with

the shape of lamp post or height of antenna due to a small variation.

With the lampshade on top of the antenna, the radiation upward will be reflected to ground, causing a strong beam downward and a null upward, which can be observed in Figure 24. Due to such a large variation of radiated power gains, the ISSDPG must be large, as shown in Figure 27. Again, because of the normalization factor and the low

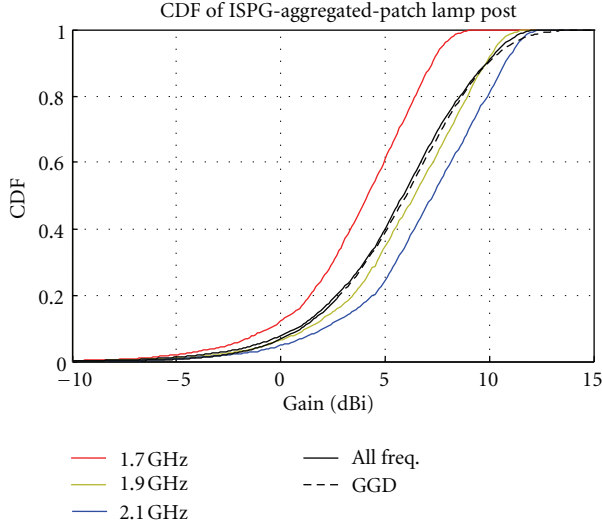


FIGURE 25: ISPG distribution for patch-lamppost scenario and fitted Gaussian distribution.

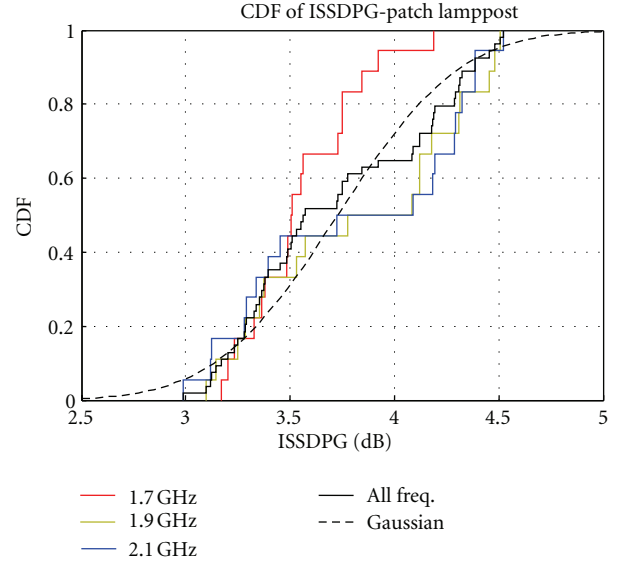


FIGURE 27: ISSDPG distribution for lamppost scenario.

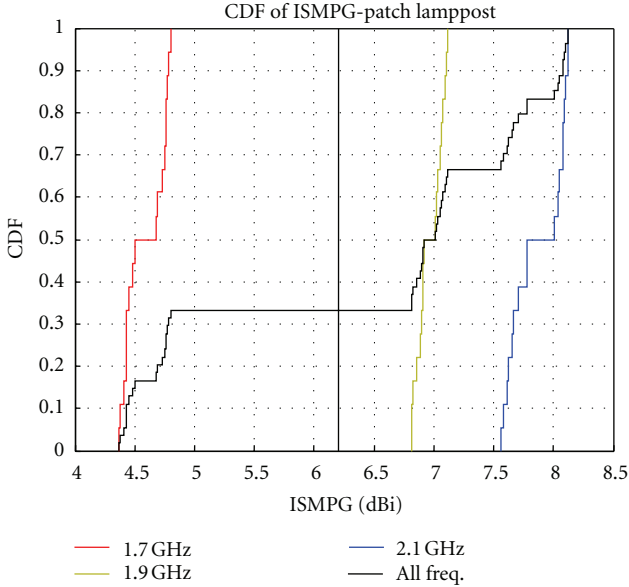


FIGURE 26: ISMPG distribution for patch-lamppost scenario.

S_{11} at 1.7 GHz, the curves are separated. A fitted Gaussian distribution has been plotted to illustrate that the aggregated ISSDPG is hard to be modeled by Gaussian distribution. The first or second central moment of ISPG (ISMPG or ISSDPG) cannot be extremely low or high in this scenario, so their values have upper and lower boundaries which may be correctly described by a linear model (uniform distribution).

5. Conclusion

In this paper we have presented simulations' results on the performance of omnidirectional and directional antennas, in proximity to a wall, a bus shelter, and a lamp post, as examples of access point placement for 4G access points,

relays, or base stations. The concept of the sector has been applied in order to focus the statistical analysis of the antenna pattern degradation by these disturbers in terms of wanted and unwanted radiation directions. Three parameters assessing the antenna performance and its degradation, which could be used in order to set up a statistical model, have been defined.

The results indicate that the lognormal distribution (Gaussian in dB) is often approximately obeyed, as regards the power gains in the considered sector. This is true for the antenna-wall scenario, while in the antenna-shelter and antenna lamppost scenarios, the ISPG appears to follows the generalized Gaussian distribution. In most scenarios, except for the patch-lamp post scenario, the mean value of ISPG is less than that of a reference antenna, due to the reflection by surrounding disturbers. The ISSDPG follows well a lognormal distribution in the antenna-wall scenarios, within the frequency band from 1.7 GHz to 2.0 GHz for both directional and nondirectional antennas. For the other scenarios, its distribution shall be carefully investigated in future works. This statistical analysis of averages and deviations of the gain in the considered sector may be helpful in appreciating the problems posed by antennas deployment in small cells at street level, when the placement of antennas must be made in locations where strong disturbances are present. In the future, the frequency and angular correlation of radiation patterns will be investigated, and the goodness of fit for statistical parameter evaluation will be studied.

Acknowledgments

This work has been partly carried out with funding from the RECOSS project under the French competitiveness cluster "Systematic." The authors are grateful to Y. Lostanlen (SIRADEL) for his support and encouragement to the work.

References

- [1] Y. Jeong, T. Q. S. Quek, and H. Shin, "Beamforming optimization for multiuser two-tier networks," *Journal of Communications and Networks*, vol. 13, no. 4, pp. 327–338, 2011.
- [2] V. Chandrasekhar, M. Kountouris, and J. G. Andrews, "Coverage in multi-antenna two-tier networks," *IEEE Transactions on Wireless Communications*, vol. 8, no. 10, pp. 5314–5327, 2009.
- [3] V. Chandrasekhar and J. G. Andrews, "Uplink capacity and interference avoidance for two-tier femtocell networks," *IEEE Transactions on Wireless Communications*, vol. 8, no. 7, pp. 3498–3509, 2009.
- [4] C. Roblin and M. A. Yousuf, "Statistical models of wideband and UWB omni-directional antennas based on a parametric modelling," in *Proceedings of the 4th European Conference on Antennas and Propagation (EuCAP '10)*, Barcelona, Spain, April 2010.
- [5] F. Molisch Andreas, F. Josef, and B. Ernst, "Pattern distortion of mobile radio base station antennas by antenna masts and roofs," in *Proceedings of the 25th European Microwave Conference*, vol. 1, pp. 71–76, September 1995.
- [6] G. Stratis, C. A. Corral, S. Emami, S. Sibecas, G. Rasor, and R. Kipp, "Composite antenna pattern for realistic ray tracing simulations," in *Proceedings of the IEEE International Antennas and Propagation Symposium and USNC/CNC/URSI North American Radio Science Meeting*, pp. 106–109, USA, June 2003.
- [7] R. L. Jesch, "Measured vehicular antenna performance," *IEEE Transactions on Vehicular Technology*, vol. 34, no. 2, pp. 97–107, 1985.
- [8] A. Sibille, J. Guterman, A. Moreira, and C. Peixeiro, "Performance evaluation of 2.4 GHz laptop antennas using a joint antenna-channel statistical model," Technical Report TD-09-930 28–30, Vienna, Austria, 2009.
- [9] A. Sibille and C. Roblin, "Analysis and modelling of the randomness in terminals antennas," *WAVES*, pp. 39–48, 2010.
- [10] M. A. Mellah, A. Sibille, C. Roblin, M. Nedil, and T. A. Denidni, "Statistical modeling of the "antenna-head" interaction," *IEEE Antennas and Wireless Propagation Letters*, vol. 10, pp. 454–457, 2011.
- [11] CST: *Microwave Studio*, 2011th edition.
- [12] <http://www.wipl-d.com>.
- [13] I. Siomina, P. Värbrand, and D. Yaun, "Automated optimization of service coverage and base station antenna configuration in UMTS networks," *IEEE Wireless Communications*, vol. 13, no. 6, pp. 16–25, 2006.
- [14] L. Song and J. Shen, *Evolved Cellular Network Planning and Optimization for UMTS and LTE*, CRC Press, London, UK, 1st edition, 2010.
- [15] *Dielectric Constants of Materials*, Clipper Controls, 2007.
- [16] B. H. Fleury, "First- and second-order characterization of direction dispersion and space selectivity in the radio channel," *IEEE Transactions on Information Theory*, vol. 46, no. 6, pp. 2027–2044, 2000.

Research Article

Differences in User Influence on MIMO Handset Antenna Performance in Reverberation Chamber

Juan D. Sánchez-Heredia,¹ Paul Hallbjörner,² Juan F. Valenzuela-Valdés,³
Thomas Bolin,⁴ and Antonio M. Martínez-González¹

¹Departamento de Tecnologías de la Información y Comunicaciones, Universidad Politécnica de Cartagena, 30202 Cartagena, Spain

²Electronics Department, SP Technical Research Institute of Sweden, Box 857, 501 15 Borås, Sweden

³Departamento de Ingeniería de Sistemas Informáticos y Telemáticos, Universidad de Extremadura, 06800 Mérida, Spain

⁴Network Communication Research Lab, Sony Mobile Communications, Nya Vattentornet, 221 88 Lund, Sweden

Correspondence should be addressed to Juan D. Sánchez-Heredia, jd.sanchez@upct.es

Received 31 July 2012; Accepted 7 October 2012

Academic Editor: Guangyi Liu

Copyright © 2012 Juan D. Sánchez-Heredia et al. This is an open access article distributed under the Creative Commons Attribution License, which permits unrestricted use, distribution, and reproduction in any medium, provided the original work is properly cited.

User influence on multiple-input multiple-output (MIMO) performance is studied for different dual antenna handsets specially designed to have good and bad MIMO performance. The study reveals that user influence can cause either improvement or degradation for different test objects, including a spread effect over the parameters. Differences in performance between good and bad handsets can be clear when they are measured without user influence, but become small under real person influence. This result illustrates the particular importance of user influence to characterize MIMO handsets.

1. Introduction

User influence on multiple antenna device performance has been a topic for research in the last few years, since it is well known that a user in the vicinity of a wireless device affects the propagation conditions that the device is experiencing. This effect is well known for single-input single-output (SISO) communications, consisting of a degradation of radiation performance due to the losses introduced by the user. This effect is usually quantified by the changes in radiation efficiency and absorbed power [1].

In spite of this knowledge, it is still not clear what the consequences are when it comes to multiple antenna devices, since they base their enhanced capabilities on a rich field distribution in terms of signal paths. Numerous studies have been performed over the last years, agreeing to the fact that the effect of the human body is more complex in MIMO terminals than in traditional ones [1–5]. The presence of the user has been demonstrated to have immediate influence on radiation patterns, input impedances and therefore on the correlation matrix, yet the effects are not fully understood and contradictory findings are commonplace. In [3], the

envelope correlation coefficients were significant when the user was present. These changes showed a more important dependence to antenna orientation in [1]. In contrast, an increment of the correlation coefficients is also available in the literature [6]. Contradictory findings can also be found for the effects on diversity gain [7].

In this paper, the performance of different handsets has been analyzed. All the handsets used within this study consist of two antennas, in order to implement diversity at the receiving terminal end of the link (SIMO: Single Input Multiple Output). This SIMO configuration is relevant for this study since it is one of the normal over-the-air (OTA) test cases for the new communication standards (HSDPA and LTE).

2. Measurements

2.1. Test Objects. Four different handsets are used for this study. Two of them work at low frequency (700–780 MHz) and the other two work at a higher frequency (2620–2690 MHz). For each band, there is one handset with a good

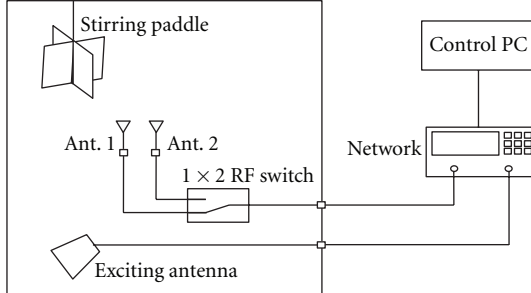


FIGURE 1: Scheme of the reverberation chamber measurement setup.

antenna solution and the other one has been designed on purpose to have bad MIMO performance.

2.1.1. 700 MHz Test Objects. Two samples of the same handset model are used with dimensions 115 mm × 65 mm. The two test objects are referred to as Prototype A and Prototype B. Prototype A has two monopole antennas located at each short side of the handset. The two monopoles excite the chassis in the same way, so high correlation is expected. Prototype B includes one monopole located at one of the short sides of the handset and a notch antenna located along the long side of it. These two antennas have different radiation patterns which cause a low correlation with each other.

2.1.2. 2600 MHz Test Objects. Two terminal antenna models are used with dimensions 100 mm × 40 mm. The two test objects are referred to as Prototype C and Prototype D. Both Prototype C and Prototype D consist of a ground plane and two Planar Inverted F Antennas (PIFA) fed by coaxial cables. Prototype C is designed to have high correlation on purpose, by slightly connecting the patches of the two single PIFA antennas; however, Prototype D has low correlation.

2.2. Measurement Setup. Measurements were carried out using a reverberation chamber (RC) (length 3 m, width 2.45 m, and height 2.45 m) located at SP Technical Research Institute of Sweden, Borås, Sweden. The RC comprises an electronically controlled turn table, as well as a rotational zig-zag stirrer placed in a corner of the metallic cavity. The shielding effectiveness of this RC is 100 dB. Figure 1 showed a basic scheme of the setup used for the measurements performed during this study.

Three different scenarios (No User, Head Phantom, and Real Person) are used to simulate different effects of the user on the radiation performance of the antennas. No User scenario is the classical scenario generated in a reverberation chamber, with an isotropic and Rayleigh distributed field strength at the device. In this scenario, the antennas under test were placed over a low loss dielectric foam piece, in order to avoid as much as possible the effect of the holder. Head Phantom is the commonly used scenario to estimate the behavior of a device including user influence, that is,

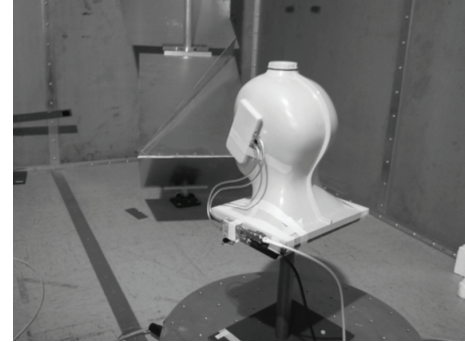


FIGURE 2: Measurement setup with the presence of the head phantom and the device placed in talk position.

device attached to the cheek of the phantom and aligned between the ear point and the mouth point (Figure 2). Real Person scenario is performed with the introduction of a real person inside the chamber, holding the device with the hand simulating talk position, in the same way as in the Head Phantom scenario. The person is sitting on a chair placed in the center of the chamber, in order to have the antenna in a similar place as in the other scenarios.

No User is used as a reference case. This scenario, although useful, is not intended to be realistic. With the introduction of a head phantom, the effect of the user head on the antenna is included. The head phantom affects the close environment of the antenna, but it is still an intermediate approach to a real user influence simulation, since a head phantom does not block all the incident waves that a real person would. This is the motivation of the Real Person scenario.

3. User Influence on Antenna Parameters

3.1. Correlation. Antenna correlation is the figure-of-merit which has been commonly accepted to be a good indicator of the MIMO performance of an antenna pair. As showed in [8], correlation affects MIMO capacity, which is clearly decreased when antennas at the receiver are highly correlated. The complex correlation coefficient of two antennas can be calculated from the complex transmission coefficients (S_{21}) between the exciting antenna of the RC and the antenna pair under test, by [9]

$$\rho = \left| \rho_{\text{complex}} \right| = \left| \frac{\sum_{k=1}^N (S_{21,1}(k) - \langle S_{21,1} \rangle)(S_{21,2}(k) - \langle S_{21,2} \rangle)^*}{\sqrt{\sum_{k=1}^N |S_{21,1}(k) - \langle S_{21,1} \rangle|^2 \sum_{k=1}^N |S_{21,2}(k) - \langle S_{21,2} \rangle|^2}} \right|, \quad (1)$$

where k stands for the current stirrer position, and

$$\langle S_{21} \rangle = \frac{1}{N} \sum_{k=1}^N S_{21}(k) \quad (2)$$

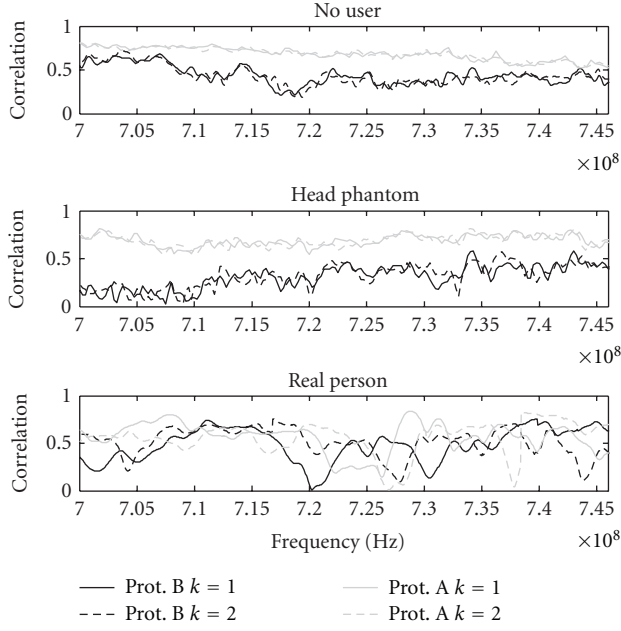


FIGURE 3: Correlation of the 700 MHz band devices for the three different scenarios.

- (i) N is the total number of stirrer positions over a whole sequence of stirring movement.
- (ii) $S_{21,1}$ is the S_{21} parameter between the transmission antenna and receiving antenna 1.
- (iii) $S_{21,2}$ is the S_{21} parameter between the transmission antenna and receiving antenna 2.

For the purpose of these measurements, 400 different positions are selected (100 stirrer position \times 4 turn table positions), and the number of points of the vector network analyzer used to perform the S_{21} measurements is set to 401.

Two repetitions ($k = 1, k = 2$) of each measurement were performed. The measurement of each of the scenarios took about 40 minutes, for each dual antenna. Some problems were detected due to the decorrelation introduced by the cables connected to the antennas. In order to avoid those problems, an RF switch is introduced between one of the connectors of the vector network analyzer and the antennas under test, so the S_{21} can be measured for the two receiving antennas without changing the position of the cables.

Figures 3 and 4 show the different correlation values obtained under the three different user influence scenarios, for antennas at both bands. Tables 1 and 2 show the values of mean and standard deviation of the measured correlation values.

Correlation is clearly affected by the presence of the user. Normally when an object is close to the antenna, the object produces two different effects. The first effect is to create new reflection points for the signal thus producing new clusters and increasing the richness of multipath propagation, which means that it decreases the correlation between antennas. On the other hand, when an object is positioned near an antenna, this object blocks the signal incoming from other

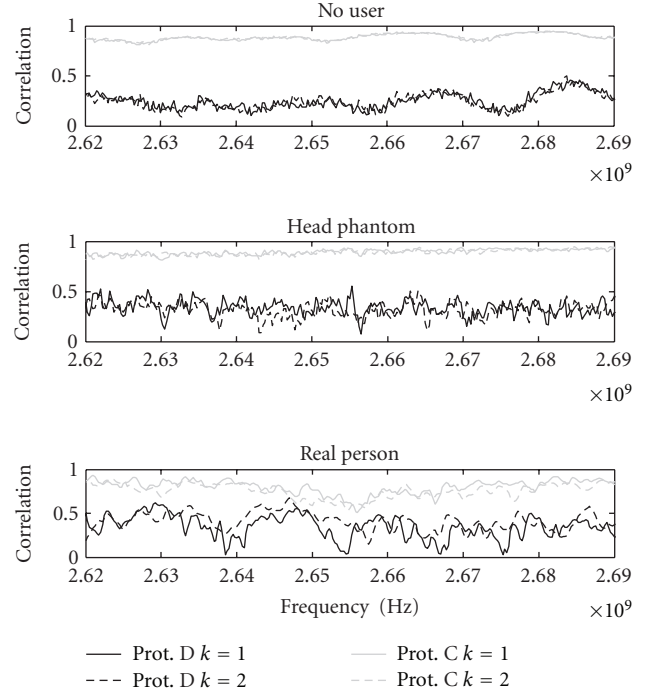


FIGURE 4: Correlation of the 2600 MHz band devices for the three different scenarios.

cluster which impoverishes multipath propagation of the signal causing an increase of the correlation.

These two opposed effects, as they are combined, cause the a randomization of the measured correlation. That is, when an object is inserted in the vicinity of a wireless device, the device can either increase or decrease its correlation. In other words, we can say that the effect of introducing objects near the antenna makes these antenna lose their inherent properties and their correlation depend more on the propagation environment. While the handsets present a well-recognized low and high correlation behavior in the No User scenario, this difference becomes smaller as the presence of the user is more significant. In fact, in the Real Person case, where there exist the influences of both the head and the hand of the person, the random effect on the results is much greater than when it is the head phantom only.

It is also worth noticing the different impact depending on the frequency. Even though the effect is important at the higher frequency, it has a dramatic impact at the 700 MHz band, where correlation becomes very similar in both test objects, and with large variations over the band. This is because in terms of (d/λ) , the distance over which the objects are placed (phantom or real person) is much smaller at 700 MHz compared to 2600 MHz, which means that an object placed closer has a greater influence.

Another factor is that the real person has a physiognomy much rougher than a phantom which is the average of many users (being the average of many users tends to round the shape). This rougher shape of individual persons, when compared to phantoms, creates more scattering effects and therefore some differences can be appreciated.

TABLE 1: Correlation results (mean).

Band	Prototype	k	No User	Head Phantom	Real Person
700 MHz	A	1	0.689	0.676	0.570
		2	0.687	0.676	0.526
	B	1	0.313	0.389	0.506
		2	0.310	0.390	0.492
2600 MHz	C	1	0.885	0.889	0.813
		2	0.886	0.886	0.760
	D	1	0.257	0.354	0.336
		2	0.255	0.340	0.375

TABLE 2: Correlation results (standard deviation).

Band	Prototype	k	No User	Head Phantom	Real Person
700 MHz	A	1	0.099	0.055	0.151
		2	0.098	0.057	0.168
	B	1	0.155	0.129	0.164
		2	0.156	0.130	0.169
2600 MHz	C	1	0.026	0.032	0.079
		2	0.027	0.035	0.074
	D	1	0.071	0.077	0.126
		2	0.073	0.083	0.115

Finally, it should be noted that the standard deviation of the correlation (Table 2) is always higher for the scenario of real person in all the prototypes. This is also observable in Figures 3 and 4, where we can see that variations in correlation are much larger with the frequency. Also the difference between the two measurement repetitions is much higher for the real person case. This is due to abrupt changes in the appearance of the real person, together with the uncertainty on the position of the prototypes introduced when a real person is holding them. Both phantoms and holders are designed so they represent the average of human shape. However, in order to detect minimums and maximums in performance, average shapes are not as useful as particular cases are. Therefore, it is advisable to perform these tests with real people because the results of these tests may differ from the results obtained using a phantom.

3.2. Diversity Gain. Diversity gain (DG) is one of the most recognized figures-of-merit when evaluating multiple antenna terminals. DG quantifies the improvement created by the existence of more than one antenna over a reference case. In this study, the reference case chosen is the average power of both antennas operating separately.

Several schemes can be used to combine the signals coming from the two antennas. Since the prototypes and antennas used in this study are intended to be part of complex wireless devices, the maximum ratio combining (MRC) [10–12] scheme is used, which is common for these kind of devices. Table 3 shows the measured DG (in dB) of the devices for a signal reliability of 1 %. Efficiency of antennas is not taken in account for the DG calculations, which means that apparent diversity gain (ADG) is calculated [13, 14].

TABLE 3: Apparent diversity gain results (decibels).

Band	Prototype	No User	Head Phantom	Real Person
700 MHz	A	6.38	6.98	6.71
	B	8.21	8.40	7.35
2600 MHz	C	5.52	5.75	7.28
	D	8.76	8.10	8.38

Low correlation handsets present a reduction in diversity gain when the user influence becomes more important. The effect is the opposite for the high correlated handsets.

This effect is in line with the correlation that both devices present under the three different scenarios. As we have seen before, the correlation between antennas is decreased in high correlated devices when they are under user influence. This effect can actually lead to a better MIMO performance of the device under user influence, compared to the performance the device has under No User scenario. Even more so, we can see how the DG results become very similar for both bad and good devices, in the case of a real person influence. It then seems that the real effect of a user on DG is the equalization of device performance, and not necessarily deterioration.

4. Conclusion

In this paper, user influence over correlation and diversity gain is evaluated for some different scenarios including a real person. This is the first time that measurements using a real person in a reverberation chamber are reported. Results show that user influence equalizes MIMO performance of devices which have very different behavior when analyzed without user influence. Furthermore, the user influence on correlation does not seem to be a linear constant offset but a spread effect.

The different behavior of different user calls for detailed studies with different body phantoms in order to define the effect of the user influence over the antenna. It is important to study standard deviations from different body phantoms. Finally, it is necessary to deepen the shadowing effect that actually changes the propagation environment where the antenna is being measured.

Further research includes the development of a theoretical model for the user influence on MIMO devices, as well as the repetition of this study including realistic propagation channel models (including delay and angular properties).

Acknowledgments

The authors wish to thank Kristian Karlsson at SP for the implementation of the measurement software for the RC. This work was supported in part by MICINN (Project TEC2008-05811) through an FPI Doctoral Grant (BES-2009-013764).

References

- [1] G. F. Pedersen and S. Skjaeris, "Influence on antenna diversity for a handheld phone by the presence of a person," in *Proceedings of the 47th IEEE Vehicular Technology Conference*, pp. 1768–1772, May 1997.
- [2] T. Zervos, A. Alexandridis, K. Peppas et al., "The influence of MIMO terminal user's hand on channel capacity," in *Proceedings of the 1st European Conference on Antennas and Propagation (EuCAP '06)*, Nice, France, November 2006.
- [3] K. Meksamoot, M. Krairiksh, and J. I. Takada, "A polarization diversity PIFA on portable telephone and the human body effects on its performance," *Proceedings of the IEICE Transactions on Communications*, vol. E84-B, no. 9, pp. 2460–2467, 2001.
- [4] D. C. Kemp and Y. Huang, "Antenna diversity and user interaction at 1800 MHz," in *Proceedings of the IEEE Antennas and Propagation Society International Symposium*, vol. 3, pp. 479–482, July 2005.
- [5] B. M. Green and M. A. Jensen, "Diversity performance of dual-antenna handsets near operator tissue," *IEEE Transactions on Antennas and Propagation*, vol. 48, no. 7, pp. 1017–1024, 2000.
- [6] J. F. Valenzuela-Valdés, A. M. Martínez-González, and D. Sánchez-Hernández, "Effect of user presence on receive diversity and MIMO capacity for Rayleigh-Fading channels," *IEEE Antennas and Wireless Propagation Letters*, vol. 6, pp. 596–599, 2007.
- [7] V. Plicanic, B. K. Lau, A. Derneryd, and Z. Ying, "Actual diversity performance of a multiband diversity antenna with hand and head effects," *IEEE Transactions on Antennas and Propagation*, vol. 57, no. 5, pp. 1547–1556, 2009.
- [8] M. Kang and M. S. Alouini, "Impact of correlation on the capacity of MIMO channels," in *Proceedings of the International Conference on Communications (ICC '03)*, pp. 2623–2627, May 2003.
- [9] D. A. Hill and J. M. Ladbury, "Spatial-correlation functions of fields and energy density in a reverberation chamber," *IEEE Transactions on Electromagnetic Compatibility*, vol. 44, no. 1, pp. 95–101, 2002.
- [10] R. G. Vaughan and J. B. Andersen, "Antenna diversity in mobile communications," in *Proceedings of the IEEE Transactions on Vehicular Technology*, vol. VT-36, pp. 147–172, November 1987.
- [11] D. G. Brennan, "Linear diversity combining techniques," in *Proceedings of the IRE*, vol. 47, pp. 1075–1102, June 1959.
- [12] D. G. Brennan, "Linear diversity combining techniques," in *Proceedings of the IEEE*, vol. 91, no. 2, pp. 331–356, February 2003.
- [13] P. S. Kildal and K. Rosengren, "Electromagnetic analysis of effective and apparent diversity gain of two parallel dipoles," *IEEE Antennas and Wireless Propagation Letters*, vol. 2, pp. 9–13, 2003.
- [14] J. F. Valenzuela-Valdés, M. A. García-Fernández, A. M. Martínez-González, and D. Sánchez-Hernández, "The role of polarization diversity for MIMO systems under Rayleigh-fading environments," *IEEE Antennas and Wireless Propagation Letters*, vol. 5, no. 1, pp. 534–536, 2006.

Research Article

Impact of Antenna Placement on Frequency Domain Adaptive Antenna Array in Hybrid FRF Cellular System

Sri Maldia Hari Asti, Wei Peng, and Fumiuki Adachi

Department of Communication Engineering, Graduate School of Engineering, Tohoku University, 6-6-05 Aza-Aoba, Aramaki, Aoba-ku, Sendai 980-8579, Japan

Correspondence should be addressed to Wei Peng, peng@mobile.ecei.tohoku.ac.jp

Received 6 July 2012; Accepted 7 September 2012

Academic Editor: Guangyi Liu

Copyright © 2012 Sri Maldia Hari Asti et al. This is an open access article distributed under the Creative Commons Attribution License, which permits unrestricted use, distribution, and reproduction in any medium, provided the original work is properly cited.

Frequency domain adaptive antenna array (FDAAA) is an effective method to suppress interference caused by frequency selective fading and multiple-access interference (MAI) in single-carrier (SC) transmission. However, the performance of FDAAA receiver will be affected by the antenna placement parameters such as antenna separation and spread of angle of arrival (AOA). On the other hand, hybrid frequency reuse can be adopted in cellular system to improve the cellular capacity. However, optimal frequency reuse factor (FRF) depends on the channel propagation and transceiver scheme as well. In this paper, we analyze the impact of antenna separation and AOA spread on FDAAA receiver and optimize the cellular capacity by using hybrid FRF.

1. Introduction

Single-carrier (SC) transmission has been adopted for uplink transmission in LTE [1] and LTE-A [2] systems due to its wide coverage and lower peak-to-average power ratio (PAPR) than multicarrier (MC) transmission. However, the wireless channel becomes severely frequency selective as the data rate increases due to the multiple paths with different time delays [3]. In such a frequency-selective channel, interblock interference (IBI) and intersymbol interference (ISI) are produced and degrade the transmission significantly. To deal with this problem, cyclic prefix (CP) will be inserted at the transmitter side, and then be removed at the receiver side to avoid IBI and frequency domain equalization (FDE) technique has been proposed to suppress ISI in SC transmission [3]. FDE equalizes the frequency domain receive signal by applying equalization weight to combat the channel fluctuation in each frequency. Several methods to calculate FDE weight have been introduced, such as zero-forcing (ZF), minimum-mean-square error (MMSE), and so forth.

In cellular system, neighboring cells will use the same carrier frequency/frequencies to save the bandwidth and cochannel interference (CCI) exists and CCI power will be determined by the distance between cochannel cells. In addition, the existence of multiple users within the same cell will cause multiuser interference (MUI). As a result, cellular capacity will be limited by multiple access interference (MAI, which includes both CCI and MUI) instead of additive noise. Adaptive antenna array (AAA) is a powerful method to combat MAI. It has been proved in [4] that AAA receiver can effectively deal with up to $N_r - 1$ interferences when flat fading channel is assumed where N_r represents the number of antenna elements in the array.

Therefore, in order to combat the MAI in frequency selective fading channel, it is natural for us to resort to both FDE and AAA. In our previous study [5], frequency domain adaptive antenna array (FDAAA) has been proposed and proved to be more effective to suppress MUI in severe frequency selective fading channel than the other frequency domain algorithms such as diversity combining algorithm. However, the performance of antenna array will depend

on antenna placement, which determines the coupling and radiation pattern between antennas. In addition, the angle of arrival (AOA) of the receive signals' waveform will also affect the performance [6, 7]. These considerations have not been addressed in our previous study and, to the best of our knowledge, have not been addressed in the literature.

On the other hand, cellular capacity is determined by the bandwidth efficiency and the available bandwidth. By increasing the frequency reuse factor (FRF), the distance between cochannel cells will increase, and the CCI power will be reduced. However, the available bandwidth is reduced at the same time. As a result, cellular capacity becomes a tradeoff between bandwidth efficiency and available bandwidth, which is determined by FRF. In our previous study [8], hybrid FRF has been proposed to optimize the cellular capacity. However, the optimal FRF depends on the channel propagation model and transceiver structure. And the cellular capacity optimization problem has to be reformulated when FDAAA receiver is considered.

In this paper, we optimize the cellular capacity in SC uplink transmission using FDAAA receiver by taking into consideration the impact of antenna placement. The remaining of the paper is organized as follows: uplink FDAAA receiver for cellular system is introduced in Section 2; Hybrid FRF algorithm and analysis on cellular capacity is given in Section 3; In Section 4, the impact of antenna placement, that is, antenna separation and AOA spread, will be analyzed; Numerical results on cellular capacity will then be given in Section 5 and finally the paper will be concluded in Section 6.

2. Uplink FDAAA Receiver in Cellular System

2.1. System Model. It is assumed that the base station (BS) locating at the center of each cell is equipped with N_r antennas, and there are U mobile stations (MSs, that is, users) in each cell and each user is equipped with a single transmit antenna, as shown in Figure 1. We assume that the 0th user is the desired user, and the other users are interfering users, it is also assumed that the channel remains unchanged during one block transmission. Two cellular structures are shown in Figure 2. On the left is the conventional cellular structure using single FRF (FRF 1), on the right is the cellular structure using hybrid FRF which will be further explained in Section 3.

The channel impulse response between the u th user and the BS can be expressed as

$$\mathbf{h}_u(\tau) = \sum_{l=0}^{L-1} \mathbf{h}_{u,l} \delta(\tau - \tau_l), \quad (1)$$

where $\mathbf{h}_{u,l}$ and τ_l are the channel gain vector and time delay of the l th path, respectively, $\sum_{l=0}^{L-1} E\{|h_{u,m,l}|^2\} = 1$ where $h_{u,m,l}$ is the m th element of $\mathbf{h}_{u,l}$ and $E\{\cdot\}$ denotes statistical expectation. The path delay is assumed to be integer multiples of symbol duration and $\tau_l = l$. CP is used and its length is assumed to be longer than the maximum path delay so that IBI can be avoided.

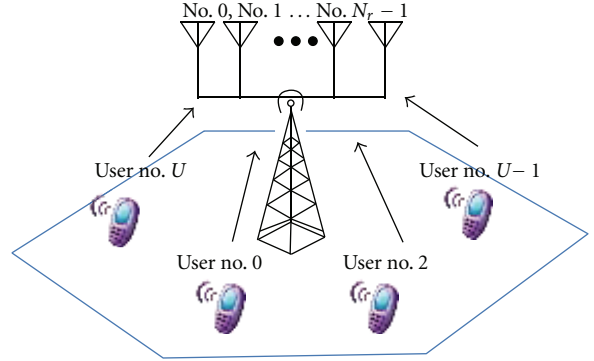


FIGURE 1: Uplink transmission in a single cell.

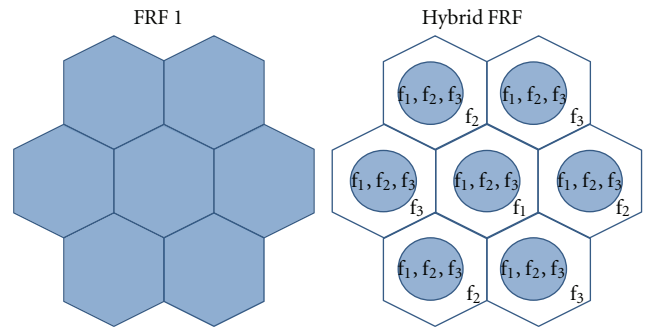


FIGURE 2: Structure of single FRF and hybrid FRF.

The baseband receive signal vector $\mathbf{r}(n) = [r_0(n), r_1(n), \dots, r_{N_r-1}(n)]^T$, ($n = 1, \dots, N_c$) is given by

$$\begin{aligned} \mathbf{r}(n) = & \sqrt{P_0 d_0^{-\alpha} 10^{-\xi_0/10}} \sum_{l=0}^{L-1} \mathbf{h}_0 s_0(n - \tau_l) \\ & + \sum_{u=1}^{U-1} \sqrt{P_u d_u^{-\alpha} 10^{-\xi_u/10}} \sum_{l=0}^{L-1} \mathbf{h}_u s_u(n - \tau_l) \\ & + \sum_{i=0}^{I-1} \sum_{u=0}^{U-1} \sqrt{P_{u,i} d_{u,i}^{-\alpha} 10^{-\xi_{u,i}/10}} \\ & \times \sum_{l=0}^{L-1} \mathbf{h}_{u,i} s_{u,i}(n - \tau_l) + \mathbf{z}(n), \end{aligned} \quad (2)$$

where U and I are the number of users per cell and the number of cochannel cells, respectively; Subscripts u and (u, i) represent the index of the u th user at the desired cell and at the i th cochannel cell, respectively; P represents the transmit power; s is the transmit signal; d represents the normalized distance between the user and the BS of the desired cell; α and ξ represent the path loss exponent and shadowing loss, respectively. $\mathbf{z}(n) = [z_0(n) \dots z_{N_r-1}(n)]^T$ is the vector of complex additive white Gaussian noise (AWGN). In this study, slow transmit power control (TPC) in each cell is assumed so that each user will have the same

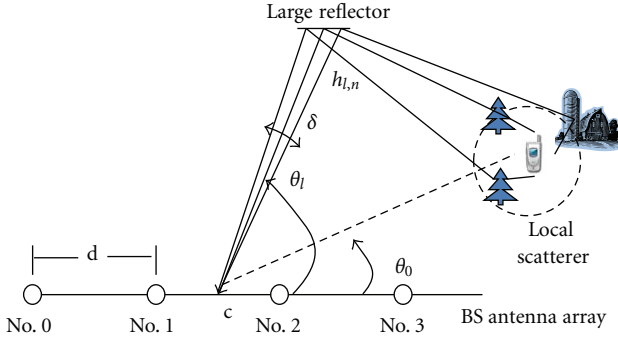


FIGURE 3: Propagation model of linear antenna array.

target receive signal power in average at the corresponding BS. Therefore, the transmit power is given by

$$P_u = \left(\frac{P_{\text{target}}}{d_u^{-\alpha} 10^{-\xi_u/10}} \right) d_{u,0}^{-\alpha} 10^{-\xi_{u,0}/10}, \quad (3)$$

where P_{target} is the target receive signal power; The frequency domain received signal on the k th frequency is then expressed as

$$\begin{aligned} \mathbf{R}(k) &= \mathbf{H}_0(k)S_0(k) + \sum_{u=1}^{U-1} \mathbf{H}_u(k)S_u(k) \\ &\quad + \sum_{i=0}^{I-1} \sum_{u=0}^{U-1} \mathbf{H}_{u,i}(k)S_{u,i}(k) + \mathbf{Z}(k), \end{aligned} \quad (4)$$

where $\mathbf{H}_u = [H_{u,0}(k) \ H_{u,1}(k) \ \dots \ H_{u,N_r-1}(k)]^T$, $S_u(k)$, and $\mathbf{Z}(k) = [Z_0(k) \ Z_1(k) \ \dots \ Z_{N_r-1}(k)]^T$ are, respectively, the frequency domain channel response, transmit signal, and noise component, given by (5). In the right hand side of (4), the first term comes from the desired user, the second term comes from MUI, the third term comes from CCI, and the last term is the noise component.

$$\begin{aligned} S_u(k) &= \sqrt{P_u d_u^{-\alpha} 10^{-\xi_u/10}} \sum_{n=0}^{N_c-1} s_u(n) \exp\left(-j2\pi n \frac{k}{N_c}\right), \\ H_{u,m}(k) &= \sum_{l=0}^{L-1} \sum_{n=0}^{N_c-1} h_{u,l,m} \exp\left(-j2\pi n \frac{k}{N_c}\right), \\ Z_m(k) &= \sum_{n=0}^{N_c-1} z_m(n) \exp\left(-j2\pi n \frac{k}{N_c}\right). \end{aligned} \quad (5)$$

2.2. Propagation Model of Adaptive Antenna Array. Linear antenna array is assumed, and the propagation model is shown in Figure 3. The geometric center of array is denoted by c and the antenna separation is denoted by d . θ_0 represents the angle between line of sight (LOS) direction of MS and the BS array plane; The plane waveform of the l th path from the u th user is consisted of a number of unresolvable paths and the angle spread of the unresolvable paths is denoted by δ ; In this study, δ is assumed to be zero for simplicity and $h_{u,l}$

represents the plane waveform of l th path from the u th user. The nominal AOA of $h_{u,l}$ observed at array center c is denoted by $\theta_{u,l}$ and the AOA spread of $\theta_{u,l}$ is uniformly distributed within a range of Δ . Therefore, the l th path gain of the u th user which is observed at the m th antenna element can be given by

$$h_{u,l,m} = h_{u,l} \exp\left(-j2\pi \frac{(0.5M - m + 0.5)}{\lambda} d \cos \theta_{u,l}\right), \quad (6)$$

where $m = 1, 2, 3, \dots, N_r$ and λ is the carrier wavelength.

2.3. FDAAA Receiver. In our previous study, FDAAA receiver has been investigated in [5–7]. The transceiver structure of SC transmission using FDAAA receiver is shown in Figure 4. At the receiver side, the CP is removed and the receive signal at each antenna is transformed to frequency domain by using fast Fourier transform (FFT), then adaptive antenna array (AAA) weight control is then performed on each frequency and the output after AAA weight control is given by [9]:

$$\hat{\mathbf{R}}(k) = \mathbf{W}_{\text{FDAAA}}^H(k) \mathbf{R}(k), \quad (7)$$

where $\mathbf{W}_{\text{FDAAA}}(k) = [W_{\text{FDAAA},0}(k), W_{\text{FDAAA},1}(k), \dots, W_{\text{FDAAA},N_r-1}(k)]^T$ minimizes the mean square error (MMSE) between $\hat{\mathbf{R}}(k)$ and the frequency domain desired signal $S_0(k)$, given by [5–7]:

$$\mathbf{W}_{\text{FDAAA}}(k) = \mathbf{X}(k)^{-1} \mathbf{p}(k), \quad (8)$$

where $\mathbf{X}(k) = E\{\mathbf{R}(k)\mathbf{R}(k)^H\}$ is the autocorrelation matrix of the received signal vector, $\mathbf{p}(k) = E\{\mathbf{R}(k)S_0^*(k)\}$ is the cross-correlation between the receive signal and the reference signal, superscript H denotes Hermitian transposition, and $*$ denotes the complex conjugate operation. It is assumed that the transmit signals from different users are independent and the noise component is also independent to them. The autocorrelation matrix $\mathbf{X}(k)$ is an $N_r \times N_r$ square matrix, and the (m, n) th element of $\mathbf{X}(k)$ is given by

$$\begin{aligned} X_{m,n}(k) &= E\{R_m(k)R_n^*(k)\} \\ &= E\{H_{0,m}(k)S_0(k)S_0^*(k)H_{0,n}^*(k)\} \\ &\quad + \sum_{u=1}^{U-1} E\{H_{u,m}(k)S_u(k)S_u^*(k)H_{u,n}^*(k)\} \\ &\quad + \sum_{i=0}^{I-1} \sum_{u=0}^{U-1} E\{H_{u,i,m}(k)S_{u,i}(k)S_{u,i}^*(k)H_{u,i,n}^*(k)\} \\ &\quad + E\{Z_m(k)Z_n^*(k)\}. \end{aligned} \quad (9)$$

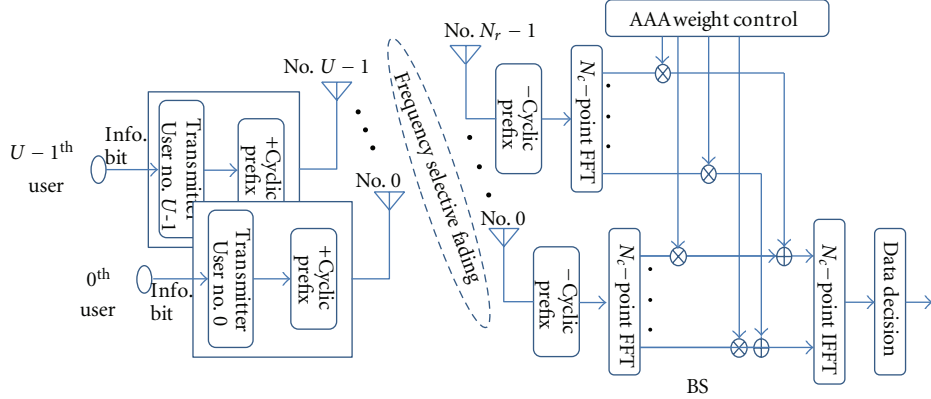


FIGURE 4: FDAAA uplink transmission.

Since channel state information (CSI) is known for the users within the cell of interest, (9) can be rewritten as

$$\begin{aligned} X_{m,n}(k) &= B_0 H_{0,m}(k) H_{0,n}^*(k) \\ &+ \sum_{u=1}^{U-1} P_{\text{MUI},u} H_{u,m}(k) H_{u,n}^*(k) \\ &+ \sum_{i=0}^{I-1} \sum_{u=0}^{U-1} \text{diag}[P_{\text{CCI},u,i}]_{N_r \times N_r} \\ &+ \sigma^2 \mathbf{I}, \end{aligned} \quad (10)$$

where B_0 is received signal power of the desired user; $P_{\text{MUI},u}$ and $P_{\text{CCI},u}$ represent MUI and CCI power from the u th user, respectively. Similarly, the m th element of the cross correlation matrix can be given by

$$p_m(k) = E\{R_m(k) S_0^*(k)\} = B_0 H_{0,m}(k). \quad (11)$$

Data decision is then made based on the time domain signal estimate which is obtained by applying inverse FFT (IFFT) to the frequency domain signal component in (7), given by

$$\hat{r}(n) = \frac{1}{N_c} \sum_{k=0}^{N_c-1} \hat{R}(k) \exp\left(j2\pi k \frac{n}{N_c}\right). \quad (12)$$

3. Hybrid FRF Algorithm and Capacity Analysis

3.1. Hybrid FRF. Different from traditional cellular system which uses the same FRF for the whole cell, hybrid FRF algorithm adopts FRF = 1 and FRF = 3 adaptively to optimize the cellular structure [10]. According to the location and instantaneous channel status of a user, hybrid FRF algorithm uses FRF 1 for area near the cell center and FRF 3 for area near the edge cell. As a result, two data rates coexist within a cell. Since the same target receive power P_{target} is required for

users with different data rates, the relation between energy and power is given as

$$\frac{E_s}{N_0} = \frac{P_{\text{target}} \times T_s}{N_0}, \quad (13a)$$

$$\frac{P_{\text{target}}}{N_0} = \begin{cases} \text{BW} \times \left(\frac{E_s}{N_0}\right)_{\text{target}}, & \text{cell center,} \\ \frac{\text{BW}}{3} \times \left(\frac{E_s}{N_0}\right)_{\text{target}}, & \text{cell edge,} \end{cases} \quad (13b)$$

where T_s is symbol period, and BW is the bandwidth. Receive power from the u th user at the desired BS and at the i th cochannel BS are given by (14) and (15), respectively.

$$\frac{B_u}{N_0} = \left(\frac{P_{\text{target}}/N_0}{d_u^{-\alpha} 10^{-\xi_u/10}} \right) d_u^{-\alpha} 10^{-\xi_u/10}, \quad (14a)$$

$$B_u = \begin{cases} (E_s)_{\text{target}} \times \text{BW}, & \text{cell center,} \\ (E_s)_{\text{target}} \times \frac{\text{BW}}{3}, & \text{cell edge,} \end{cases} \quad (14b)$$

$$\frac{B_{u,i}}{N_0} = \left(\frac{P_{\text{target}}/N_0}{r_{u,i}^{-\alpha} 10^{-\eta_{u,i}/10}} \right) d_{u,i}^{-\alpha} 10^{-\xi_{u,i}/10}, \quad (15a)$$

$$\begin{aligned} B_{u,i} &= \left(\frac{P_{\text{target}}}{r_{u,i}^{-\alpha} 10^{-\eta_{u,i}/10}} \right) d_{u,i}^{-\alpha} 10^{-\xi_{u,i}/10} \\ &= \begin{cases} \left(\frac{(E_s)_{\text{target}} \times \text{BW}}{r_{u,i}^{-\alpha} 10^{-\eta_{u,i}/10}} \right) d_{u,i}^{-\alpha} 10^{-\xi_{u,i}/10}, & \text{cell center,} \\ \left(\frac{(E_s)_{\text{target}} \times (\text{BW}/3)}{r_{u,i}^{-\alpha} 10^{-\eta_{u,i}/10}} \right) d_{u,i}^{-\alpha} 10^{-\xi_{u,i}/10}, & \text{cell edge,} \end{cases} \end{aligned} \quad (15b)$$

where $r_{u,i}$ represents normalized distance between the u th user and its corresponding BS in the i th cochannel cell.

3.2. System Capacity Analysis. Capacity is the highest rate at which information can be sent over the channel with

arbitrarily small probability of error [11] and the relation between capacity (bps/Hz) and signal-to-noise-plus-interference ratio (SINR) is given by

$$C = (1 + \log_2 \text{SINR}). \quad (16)$$

In cellular system, carrier frequency/frequencies will be reused by neighboring cells. Taking FRF into consideration, cellular capacity in bps/Hz/BS is given by

$$\bar{C} = \frac{1}{\text{FRF}} (1 + \log_2 \text{SINR}). \quad (17)$$

In hybrid FRF cellular system, since FRF 1 and FRF 3 are both used within a cell, cellular capacity depends on user's location and (17) is rewritten as

$$\bar{C} = \begin{cases} \log_2(1 + \text{SINR}), & \text{FRF1 area}, \\ \frac{1}{3} \log_2(1 + \text{SINR}), & \text{FRF3 area}. \end{cases} \quad (18)$$

In order to evaluate the cellular capacity, we are going to derive SINR in the next. For FDAAA, the signal power of array output can be calculated by

$$\begin{aligned} P_{\text{FDAAA}} &= E \left\{ \frac{1}{N_c} \sum_{k=0}^{N_c-1} \hat{R}(k) \hat{R}^*(k) \right\} \\ &= \frac{1}{N_c} \sum_{k=0}^{N_c-1} \mathbf{W}_{\text{FDAAA}}^H(k) [\mathbf{R}_s(k) + \mathbf{R}_{NI}(k)] \\ &\quad \times \mathbf{W}_{\text{FDAAA}}(k), \end{aligned} \quad (19)$$

where $\mathbf{R}_s(k)$ is the autocorrelation matrix of the receive signal from the desired user, and $\mathbf{R}_{NI}(k)$ is the autocorrelation matrix of the receive signal from interfering users plus noise. Therefore, SINR can be obtained by

$$\begin{aligned} \text{SINR} &= \frac{\text{power of received signal}}{\text{power of interference + noise power}} \\ &= \frac{\sum_{k=0}^{N_c-1} \mathbf{W}_{\text{FDAAA}}(k) \mathbf{R}_s(k) \mathbf{W}_{\text{FDAAA}}(k)}{\sum_{k=0}^{N_c-1} \mathbf{W}_{\text{FDAAA}}^H(k) \mathbf{R}_{NI}(k) \mathbf{W}_{\text{FDAAA}}(k)}. \end{aligned} \quad (20)$$

Note that interference power also depends on the users' location and two cases should be considered:

Case 1 (Desired user is inside FRF 1 area). MUI power is given by

$$P_{\text{MUI},u} = \begin{cases} (E_s)_{\text{target}} \times \text{BW}, & \text{cell center}, \\ (E_s)_{\text{target}} \times \frac{\text{BW}}{3}, & \text{cell edge}, \end{cases} \quad (21)$$

and CCI power is given by

$$P_{\text{CCI},u}$$

$$\begin{aligned} &= \begin{cases} \left(\frac{(E_s)_{\text{target}} \times \text{BW}}{r_{u,i}^{-\alpha} 10^{-\eta_{u,i}/10}} \right) d_{u,i}^{-\alpha} 10^{-\xi_{u,i}/10}, & \text{cell center}, \\ \left(\frac{(E_s)_{\text{target}} \times (\text{BW}/3)}{r_{u,i}^{-\alpha} 10^{-\eta_{u,i}/10}} \right) d_{u,i}^{-\alpha} 10^{-\xi_{u,i}/10}, & \text{cell edge}. \end{cases} \end{aligned} \quad (22)$$

Case 2 (Desired user is inside FRF 3 area). MUI power is given by

$$P_{\text{MUI},u} = \begin{cases} (E_s)_{\text{target}} \times \frac{\text{BW}}{3}, & \text{cell center}, \\ (E_s)_{\text{target}} \times \frac{\text{BW}}{3}, & \text{cell edge}, \end{cases} \quad (23)$$

and CCI power is given by

$$\begin{aligned} P_{\text{CCI},u} &= \begin{cases} \left(\frac{(E_s)_{\text{target}} \times (\text{BW}/3)}{r_{u,i}^{-\alpha} 10^{-\eta_{u,i}/10}} \right) d_{u,i}^{-\alpha} 10^{-\xi_{u,i}/10}, & \text{cell center} \\ \left(\frac{(E_s)_{\text{target}} \times (\text{BW}/3)}{r_{u,i}^{-\alpha} 10^{-\eta_{u,i}/10}} \right) d_{u,i}^{-\alpha} 10^{-\xi_{u,i}/10}, & \text{cell edge}. \end{cases} \end{aligned} \quad (24)$$

4. Impact of Antenna Placement

FDAAA receiver was proposed as a solution to combat MAI in frequency selective fading environment. In our previous study, it has been proved that when the antennas are considered to be uncorrelated with each other, FDAAA receiver has the ability to accommodate up to N_r users in a single cell and even in cellular environment when the FRF is big enough. However, the noncorrelation assumption is impractical and correlation often occurs and depends on the antenna placement in an array. To understand the impact of antenna placement, two parameters, antenna separation d and AOA spread Δ , are considered in this study. Equation (6) can be rewritten by

$$\mathbf{h}_{u,l} = h_{u,l} \mathbf{w}(\theta_{u,l}), \quad (25)$$

where $\mathbf{w}(\theta_{u,l})$ is the steering vector of the linear array, given by

$$\begin{aligned} \mathbf{w}(\theta_{u,l}) &= [w_0(\theta_{u,l}), w_1(\theta_{u,l}), \dots, w_{N_r-1}(\theta_{u,l})]^T \\ &= \left[\exp \left(-j 2 \pi \frac{(0.5 N_r - 0.5)}{\lambda} d \cos \theta_{u,l} \right), \right. \\ &\quad \left. \exp \left(-j 2 \pi \frac{(0.5 N_r - 1.5)}{\lambda} d \cos \theta_{u,l} \right), \dots, \right. \\ &\quad \left. \exp \left(j 2 \pi \frac{(0.5 N_r - 0.5)}{\lambda} d \cos \theta_{u,l} \right) \right]^T. \end{aligned} \quad (26)$$

$\theta_{u,l}$ is uniformly distributed within a range of Δ and the probability density function of $\theta_{u,l}$ is given by

$$f(\theta_{u,l}) = \begin{cases} \frac{1}{\Delta}; & -\frac{\Delta}{2} + \theta_0 \leq \theta_{u,l} \leq \frac{\Delta}{2} + \theta_0, \\ 0; & \text{otherwise}. \end{cases} \quad (27)$$

The spatial correlation between the m th and n th antenna elements can be calculated by [12–15]:

$$\begin{aligned} D_s(m, n) &= \int_{\theta_{u,l}} w_m(\theta_{u,l}) w_n^*(\theta_{u,l}) f(\theta_{u,l}) d\theta_{u,l} \\ &= \frac{1}{\Delta} \int_{-(\Delta/2)+\theta_0}^{(\Delta/2)+\theta_0} \exp \left(j 2 \pi \frac{m-n}{\lambda} d \cos \theta_{u,l} \right) d\theta_{u,l}. \end{aligned} \quad (28)$$

TABLE 1: Simulation parameters.

Transmitter	Data modulation	QPSK
	FFT size	$N_c = 256$
	TPC	Slow TPC
	Number of user per cell	$U = 1 \sim 8$
	No. of CCI cells	$I = 18$
Channel	Target receive E_s/N_0 per antenna	10 dB
	Channel model	Frequency-selective block Rayleigh fading
	Power delay profile	$L = 16$ uniform power delay
	Angle spread of resolvable paths (AOA)	$\Delta = 30^\circ, 60^\circ, 180^\circ, 360^\circ$
	Path loss exponent	$\alpha = 3.5$
	Standard deviation of shadowing losses	$\xi = 6$ dB
	Channel State Information	Available only for user within the desired cell
Receiver	Nominal angle	Random
	No. of antennas	$N_r = 8$
	Antenna separation	$\lambda/2, \lambda, 5\lambda, 10\lambda$
Channel estimation	Channel estimation	Ideal

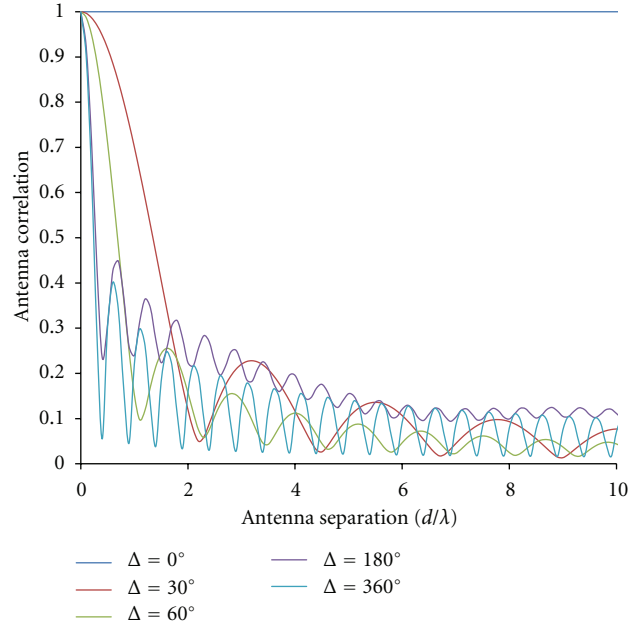
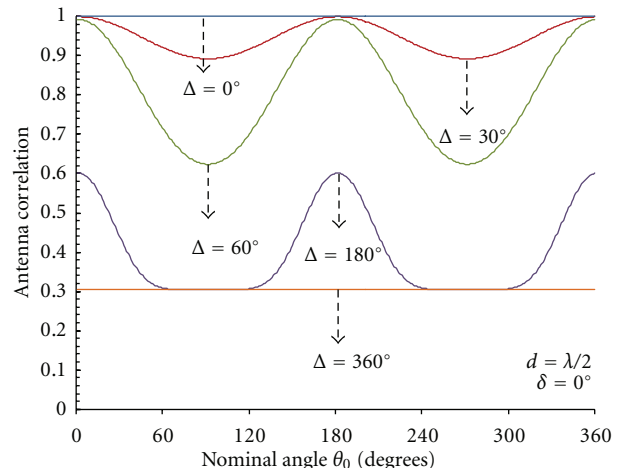
According to (28), the correlation between antenna elements as a function of AOA spread Δ as well as antenna separation d is calculated. The antenna correlation for $\theta_0 = 60^\circ$ is shown in Figure 5. It is shown that when d increases, the antenna correlation decreases with vibration and finally converges to zero when d becomes infinite. In the extreme case when $d = 0$, all the antenna elements in the array become completely correlated. On the other hand, to increase the AOA spread Δ will speed up the convergence to zero. Therefore, in order to have less correlation between antennas, two possible ways are to increase d by occupying more space or to increase Δ by introducing more reflectors around the antenna array.

In addition, the antenna correlation will also be affected by angle θ_0 and the relation between antenna correlation and θ_0 is shown in Figure 6 where $d = \lambda/2$ is used. It is shown that the antenna correlation has the smallest value when $\theta_0 = 90^\circ$ or $\theta_0 = 270^\circ$. In other words, in order to reduce the antenna correlation, the third way is to adjust the array plane to be vertical to the incoming waveform.

5. Numerical Result

In the next, we are going to study the impact of antenna placement on the uplink cellular capacity using FDAAA receiver following (18) by Monte Carlo simulations. The parameters to be used are listed in Table 1.

In order to calculate the capacity for hybrid FRF cellular system, the hybrid FRF scheme, that is, FRF 1 area and FRF 3 area allocation within each cell should be determined at the

FIGURE 5: Antenna correlation for $\theta_0 = 60^\circ$.FIGURE 6: Relation between antenna correlation and θ_0 .

first place. The cellular capacity will then be calculated based on the hybrid FRF scheme. In order to optimize the capacity performance, hybrid FRF is determined as

$$\text{FRF}_{\text{hybrid}} = \arg \min_{\text{FRF}=\{1,3\}} \frac{1}{\text{FRF}} (1 + \log_2 \text{SINR}). \quad (29)$$

For example, when antenna separation is $d = \lambda/2$ and AOA spread $\Delta = 360^\circ$, hybrid FRF scheme with varying number of users is shown in Figure 7 where the FRF 1 area and FRF 3 area are separated by the colored circular curves. It is natural to observe that the FRF 1 area decreases when the number of users in each cell increases in order to optimize the cellular capacity when CCI power increased.

In the next, impact of antenna placement on the cellular capacity will be studied and our focus is on cellular outage

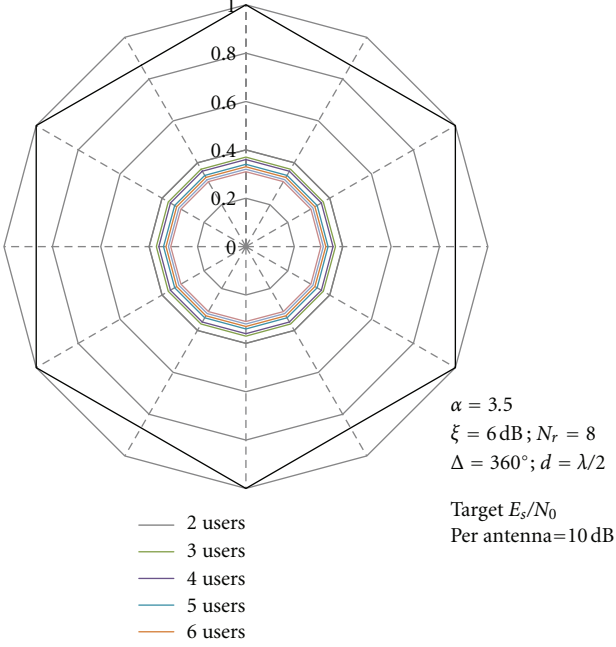


FIGURE 7: Hybrid FRF scheme with varying number of users.

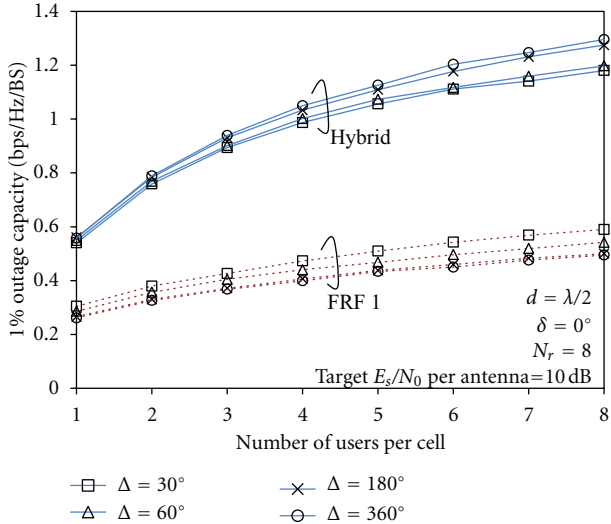


FIGURE 8: Cellular outage capacity with 1% outage probability.

capacity (the value that cellular capacity falls below with the outage probability) [16]. At first, the impact of AOA spread on cellular outage capacity is considered. In order to observe the effect of hybrid FRF algorithm, cellular capacity of single frequency reuse (FRF = 1) system is also calculated to make a comparison. The simulation results of 1% and 10% outage capacity are shown in Figures 8 and 9, respectively. It can be observed that the when AOA spread Δ increases from 30° to 360° , the cellular capacity increases for both hybrid FRF and FRF 1 cases. Recall that in Figure 5, we observed decreased antenna correlation when Δ increases. Actually, when $d = \lambda/2$ is used, FDAAA uses the correlation between

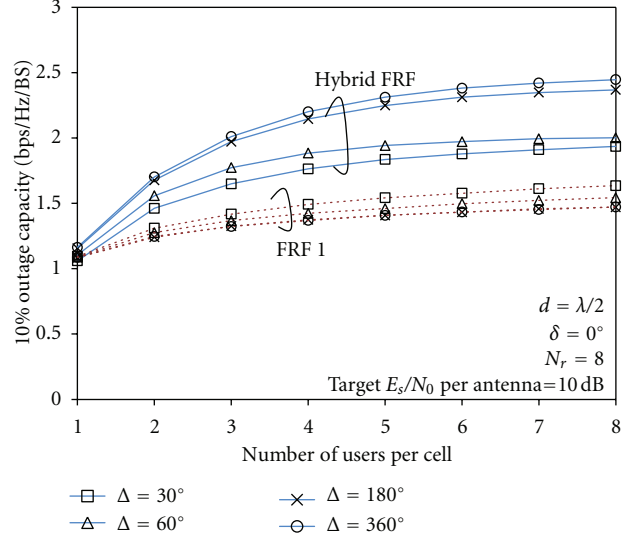


FIGURE 9: Cellular outage capacity with 10% outage probability.

antennas to generate beams in the directions of desired user and nulls in the directions of interfering users. When antenna correlation increases, the radiation pattern of the array will not be good enough and nonzero array gain will occur in the should-be-null directions, as shown in Figure 10. However, it is also observed that the capacity increase by increasing the AOA spread is quite limited, and the residue MAI should be the limiting factor.

The impact of antenna separation d is considered in the following. Assuming AOA spread $\Delta = 30^\circ$, the cellular outage capacity is calculated for $d = \lambda/2$, $d = \lambda$, $d = 5\lambda$ and 10λ . The results corresponding to 1% and 10% outage probability are shown in Figures 11 and 12, respectively. It is observed that the cellular capacity can be obviously increased when the antenna separation increases. Recall that in Figure 5 we observed decreased antenna correlation when d increases and when d becomes larger than 5λ , antenna correlation drops to below 0.1, and the antenna elements can be treated as independent. In this situation, no beams or nulls will be generated (as shown in Figure 13) and diversity gain of multiple antennas can be utilized to combat MAI, and therefore maximize the achievable SINR.

In addition, it can be observed from Figures 8-9 and Figures 11-12 that the cellular outage capacity can be increased by using hybrid FRF and the increase in percentage is summarized in Tables 2 and 3 for $d = \lambda/2$ and $\Delta = 30^\circ$, respectively. It is now obvious that by using hybrid FRF, cellular outage capacity, especially when the outage probability is low, can be greatly increased by using hybrid FRF. As we know that outage capacity is usually contributed by the users near the cell edge and the quality of service (QoS) of these users always suffers from strong CCI. Therefore, hybrid FRF together with FDAAA receiver is an effective solution to improve the QoS of the cell edge users and therefore can help to improve the fairness among users as well.

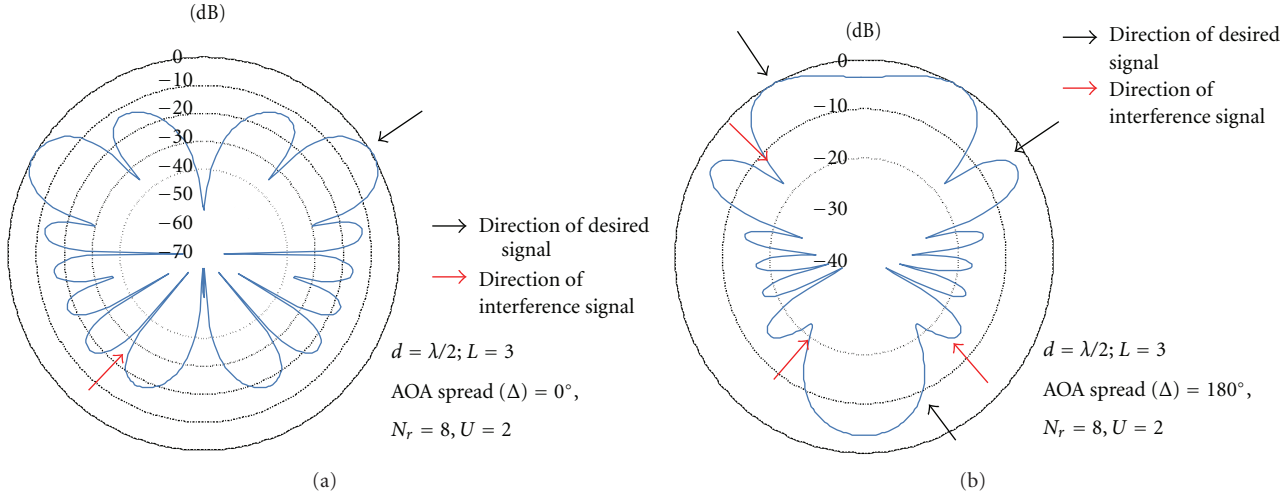


FIGURE 10: FDAAA Radiation pattern change from $\Delta = 0^\circ$ to $\Delta = 180^\circ$ where nonzero array gain appears in should-be-null direction.

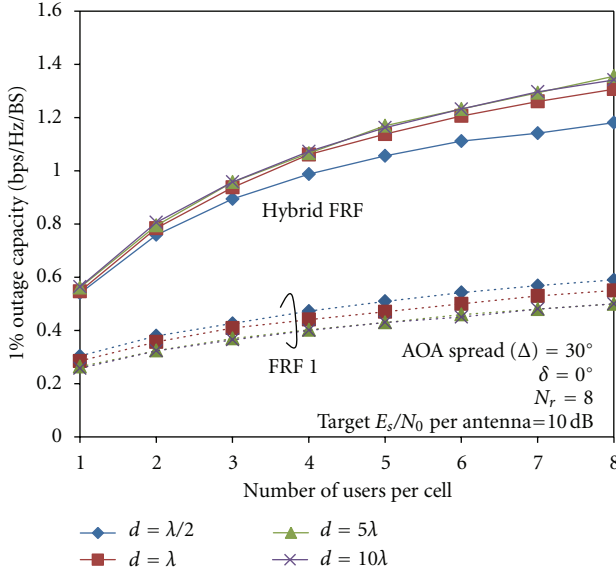


FIGURE 11: Cellular outage capacity with 1% outage probability.

TABLE 2: Cellular capacity increase by using hybrid FRF ($d = \lambda/2$).

Outage probability	Capacity increase			
	$\Delta = 30^\circ$	$\Delta = 60^\circ$	$\Delta = 180^\circ$	$\Delta = 360^\circ$
1%	110%	129%	156%	168%
10%	19%	33%	61%	67%

TABLE 3: Cellular capacity increase by using hybrid FRF ($\Delta = 30^\circ$).

Outage probability	Capacity increase			
	$d = \lambda/2$	$d = \lambda$	$d = 5\lambda$	$d = 10\lambda$
1%	110%	142%	172%	174%
10%	19%	41%	68%	71%

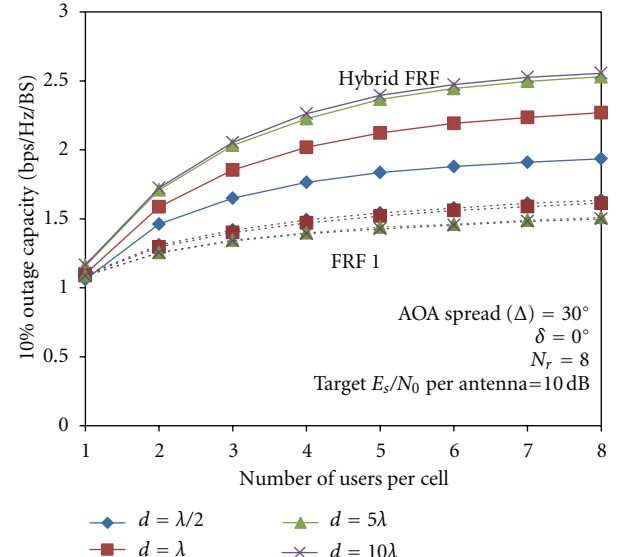
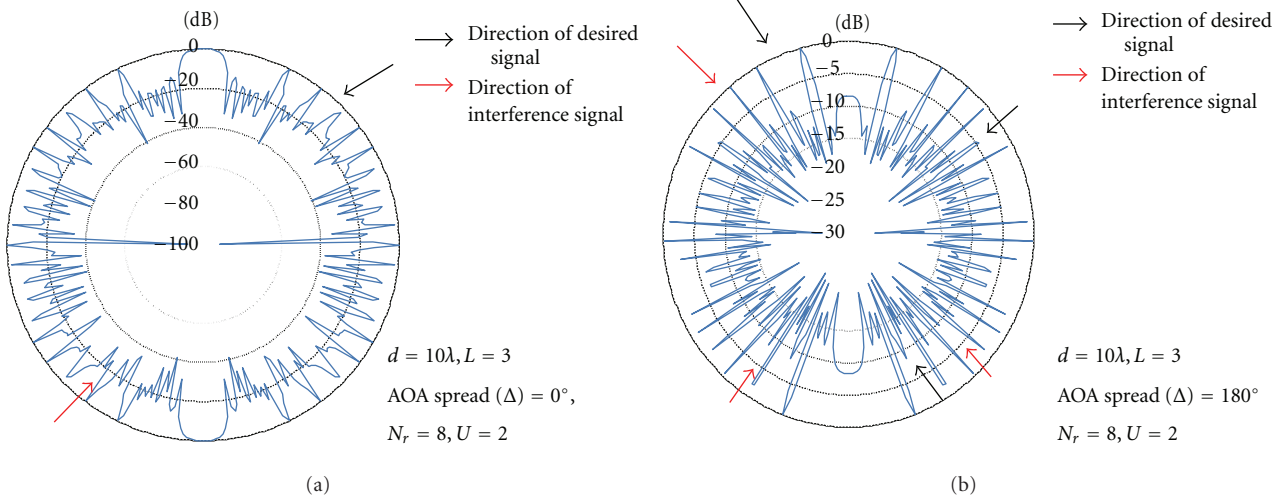


FIGURE 12: Cellular outage capacity with outage probability of 10%.

6. Conclusions

In this paper, the impact of antenna placement on the FDAAA receiver in hybrid FRF cellular system has been studied. Two parameters, antenna separation and AOA spread, have been considered. Taking the hybrid FRF into consideration, cellular capacity is derived and the impact of antenna placement on cellular capacity is then evaluated. It has been shown that increasing the AOA spread can reduce the antenna correlation, and therefore can increase the cellular capacity by using FDAAA receiver. On the other hand, increasing the antenna separation to above 5λ will reduce the antenna correlation to almost zero and can greatly increase the cellular capacity. In addition, the comparison between hybrid FRF and FRF 1 has shown that hybrid FRF algorithm can effectively improve the cellular outage

FIGURE 13: FDAAA radiation pattern when antenna separation $d = 10\lambda$.

capacity, and therefore hybrid FRF together with FDAAA receiver is a good solution for uplink transmission in cellular system.

Acknowledgment

This work was supported in part by 2011 KDDI Research Grant Program (J110000208).

References

- [1] H. G. Myung, J. Lim, and D. J. Goodman, "Single carrier FDMA for uplink wireless transmission," *IEEE Vehicular Technology Magazine*, vol. 1, no. 3, pp. 30–38, 2006.
- [2] S. Jimaa, K. K. Chai, Y. Chen, and Y. Alfaadhl, "LTE-A an overview and future research areas," in *Proceedings of the IEEE 7th International Conference on Wireless and Mobile Computing, Networking and Communications (WiMob)*, pp. 395–399, Wuhan, China, October 2011.
- [3] F. Adachi, H. Tomeba, and K. Takeda, "Frequency-domain equalization for broadband single-carrier multiple access," *IEICE Transactions on Communications*, vol. 92, no. 5, pp. 1441–1456, 2009.
- [4] J. H. Winters, "Signal acquisition and tracking with adaptive arrays in the digital mobile radio system IS-54 with flat fading," *IEEE Transactions on Vehicular Technology*, vol. 42, no. 4, pp. 377–384, 1993.
- [5] W. Peng and F. Adachi, "Frequency domain adaptive antenna array algorithm for single-carrier uplink transmission," in *Proceedings of the IEEE 20th Personal, Indoor and Mobile Radio Communications Symposium (PIMRC' 09)*, pp. 2514–2518, Tokyo, Japan, September 2009.
- [6] B. Kang, O. Nakamura, H. Tomeba, and F. Adachi, "Performance comparison of Pre-FFT and Post-FFT OFDM adaptive antenna array," in *Proceedings of the 3rd IEEE VTS Asia Pacific Wireless Communications Symposium*, Daejeon, South Korea, August 2006.
- [7] K. Takeda, R. Kawauchi, and F. Adachi, "Single-carrier uplink transmission using frequency-domain equalization," in *Proceedings of the 9th Symposium on Wireless Personal* *Multimedia Communications*, pp. 776–780, Hyatt Regency La Jolla, San Diego, Calif, USA, September 2006.
- [8] W. Peng and F. Adachi, "Multi-user hybrid FRF algorithm for downlink cellular MIMO systems," in *Proceedings of the IEEE 20th Personal, Indoor and Mobile Radio Communications Symposium (PIMRC' 09)*, pp. 968–972, Tokyo, Japan, September 2009.
- [9] W. Peng and F. Adachi, "Frequency domain adaptive antenna array for broadband single-carrier uplink transmission," *IEICE Transactions on Communications*, vol. 94, no. 7, pp. 2003–2012, 2011.
- [10] J. C. Liberti and J. S. Rappaport, *Smart Antenna for Wireless Communication: IS-95 and Third Generation CDMA Applications*, Prentice Hall, Upper Saddle River, NJ, USA, 1995.
- [11] J. G. Proakis, *Digital Communications*, McGraw Hill, New York, NY, USA, 2001.
- [12] J. Salz and J. H. Winters, "Effect of fading correlation on adaptive arrays in digital mobile radio," *IEEE Transactions on Vehicular Technology*, vol. 43, no. 4, pp. 1049–1057, 1994.
- [13] K. Watanabe, S. Sampei, and N. Morinaga, "Effect of angle spread on system capacity in DS/CDMA cellular system using adaptive array antenna," in *Proceedings of the 11th IEEE International Symposium on Personal, Indoor and Mobile Radio Communications (PIMRC' 00)*, vol. 1, pp. 98–102, September 2000.
- [14] J. A. Tsai, R. M. Buehrer, and B. D. Woerner, "The impact of AOA energy distribution on the spatial fading correlation of linear antenna array," in *Proceedings of the IEEE Vehicular Technology Conference (VTC' 02)*, pp. 933–937, May 2002.
- [15] F. Adachi, M. T. Feeney, A. G. Williamson, and J. D. Parsons, "Cross-correlation between the envelopes of 900 MHz signals received at a mobile radio base station site," *IEE Proceedings*, vol. 133, no. 6, pp. 506–512, 1986.
- [16] K. Adachi, F. Adachi, and M. Nakagawa, "On cellular MIMO spectrum efficiency," in *Proceedings of the 66th IEEE Vehicular Technology Conference (VTC-Fall'07)*, pp. 417–421, Baltimore, Md, USA, October 2007.